Wave Uplift Pressure on Horizontal Platforms

by

Kamran Iradjpanah

USCSG-TR-01-84

SEA GRANT

Technical Reports

UNIVERSITY OF SOUTHERN CALIFORNIA
Institute for Marine and Coastal Studies
University Park, Los Angeles, CA 90007

USC imcs

The Institute for Marine and Coastal Studies was founded by the University of Southern California in 1975 to be the institutional framework for its marine programs, many of which had been in operation since the early 1900s. The Institute promotes basic and applied research, as well as training in marine studies; sponsors workshops, conferences and extension courses; and produces reports and publications based on Institute-sponsored research. The work of the Institute takes place throughout the Southern California region--at USC's University Park campus, on several research vessels, at the research facilities located at the Port of Los Angeles and the Catalina Marine Science Center on Santa Catalina Island.

A part of the Institute is the Sea Grant program, funded by the National Oceanic and Atmospheric Administration, Department of Commerce. Each year, the USC Sea Grant program supports one or more research projects in each of the following areas: socio-economic systems, living marine resources, non-living marine resources, coastal engineering, marine education and advisory services.

Wave Uplift Pressure on Horizontal Platforms

by

Kamran Iradjpanah

USCSG-TR-01-84

This technical report is the result of a research project sponsored by the University of Southern California's Sea Grant Institutional Program, Institute for Marine and Coastal Studies, with funding from the National Oceanic and Atmospheric Administration (NOAA) of the Department of Commerce and the State of California.

Published and distributed by:

USC Sea Grant Institutional Program
Institute for Marine and Coastal Studies
University of Southern California
University Park
Los Angeles, CA 90089-0341

3/84

ACKNOWLEDGMENTS

I would like to take this opportunity to express my deepest appreciation and sincere gratitude to my thesis advisors, Professor J.J. Lee and Professor L.C. Wellford, Jr., for their guidance, constant encouragement, and valuable suggestions. I would like to thank Professor C.M. Ho for his assistance and careful review on the presentation of this material.

I would like to dedicate this dissertation to my parents who had constantly supported me in my educational pursuits for as long as I can remember, regardless of the personal sacrifices involved; to my wife, Afsaneh, for her infinite love, patience, and encouragement through my academic endeavors at the University of Southern California.

I wish to express my gratitude to Professor Raichlen of Caltech for his cooperation to the use of the facilities of the W.M. Keck Laboratory of Hydraulics and water resources at the California Institute of Technology for experimental study of this work; the valuable help of Mr. J. Skjelbreia is also appreciated.

I would also like to extend my thanks to my fellow student Mr. M. Sobhani for the many hours of discussions and interchange of information during study of this work; to Ms. Hilda Marti for her enthusiastic help in typing the manuscript, and to Mr. D. Howland for drafting the figures.

This research was supported by the NOAA SEA Grant Program under grant No. NA18AA-D-00094.

ABSTRACT

An analysis is presented to investigate aspects of wave hydrodynamic effects on a horizontal platform by numerical methods. A finite element procedure is developed to model the fluid region. The flow is assumed to be inviscid and irrotational. The two-dimensional model treats the full non-linear free surface equations along with Laplace equation. In this model, the physical domain is subdivided into segments. the hydrodynamic equations of motion for each segment are independently mapped using isoparametric procedure, into an assemblage of mathematical planes of simple geometry. Finite element modelling is done in the sequence of mathematical planes. The resulting discrete equations are solved iteratively using multi-grid methods. The water particle velocities are computed for different depths and locations along the platform and compared to the laboratory data using a two-dimensional Laser Doppler Velocimeter (LDV). The transmitted waves downstream the platform are also obtained and compared to that of experimental measurement. The uplift pressures time-history are found for different locations and platform underside clearances. The pressure profile is characterized by an impulsive peak pressure

followed by a slowly varying pressure which is first positive and then negative. The computed pressure-time results compared fairly well with the earlier laboratory measured data. The time-history of the uplift force is initially positive; increasing with time to a maximum which is greater than hydrostatic force; then decreases with time reaching negative values substantially larger than the positive force then returns to zero. Again, the computed force-time-history compares quite well with the available experimental data.

TABLE OF CONTENTS

LIST OF FIGURES

CHAPTER 1

INTRODUCTION

Due to growing efforts in the prospecting and harvesting of marine resources, offshore and nearshore construction activities have been steadily on the rise over the years. This makes the task of accurately determining the wave forces on coastal structures a very important one. These offshore structures may serve as platforms for prospecting and production of oil and minerals, for scientific research, and as weather stations or as piers.

In a storm or in the presence of unusual wave activities, marine structures, such as piers or offshore platforms, may be subjected to significant uplift pressures even if they are built above the still-water level. These pressures occur when progressive incident waves propagate beneath the structure and make contact with it. If these uplift pressures are not properly understood and accounted for in the design stage, they can ultimately destroy the structure.

There have been numerous reports of structural failures due to large incident waves or due to oscillations from sources not previously accounted for. Only when accurate estimates of the wave forces are available can economical coastal structures be designed and constructed.

Previous studies by El Ghamry (1963), Wang (1967), and French (1969) have demonstrated the existence of uplift pressure, but as yet, no satisfactory theoretical model has been provided. French (1969) conducted an experimental study on wave uplift pressures on a horizontal platform subjected to solitary waves of various amplitudes. His results indicated that uplift pressure are characterized by an initial peak pressure of considerable magnitude but of very short duration (impact pressure), followed by slowly varying uplift pressure of less magnitude but of considerable duration, which typically is first positive and then negative.

The major objective of the present study is to investigate aspects of wave hydrodynamic effects on a horizontal platform by numerical methods. A finite element modeling technique has been used to actually model

the fluid flow and predict the fluid kinematic behavior as a function of time. The flow is assumed to be inviscid and irrotational. The two-dimensional model treats the full nonlinear free surface equations along with Laplace equations. A solitary-type wave has been adapted as the incident wave for this analysis, since it represents a finite-amplitude ocean wave propagating through shallow water, and it is also conveniently mathematically representable. There are several mathematical theories for this type of wave, and a simulated wave can be generated easily in a laboratory with a high degree of reproducibility of wave height.

In Chapter 2, previous mathematical and experimental studies of uplift pressures on platforms and related phenomenon are surveyed. In Chapter 3, mathematical aspects of the free surface flow and the available methods of solutions are discussed. In Chapter 4, numerical schemes of the governing equations are presented. In Chapter 5, the experimental equipment and procedure for velocity measurements by means of a Laser-Doppler velocimeter are discussed. The results of the investigation are presented in Chapter 6. Conclusions are presented in Chapter 7.

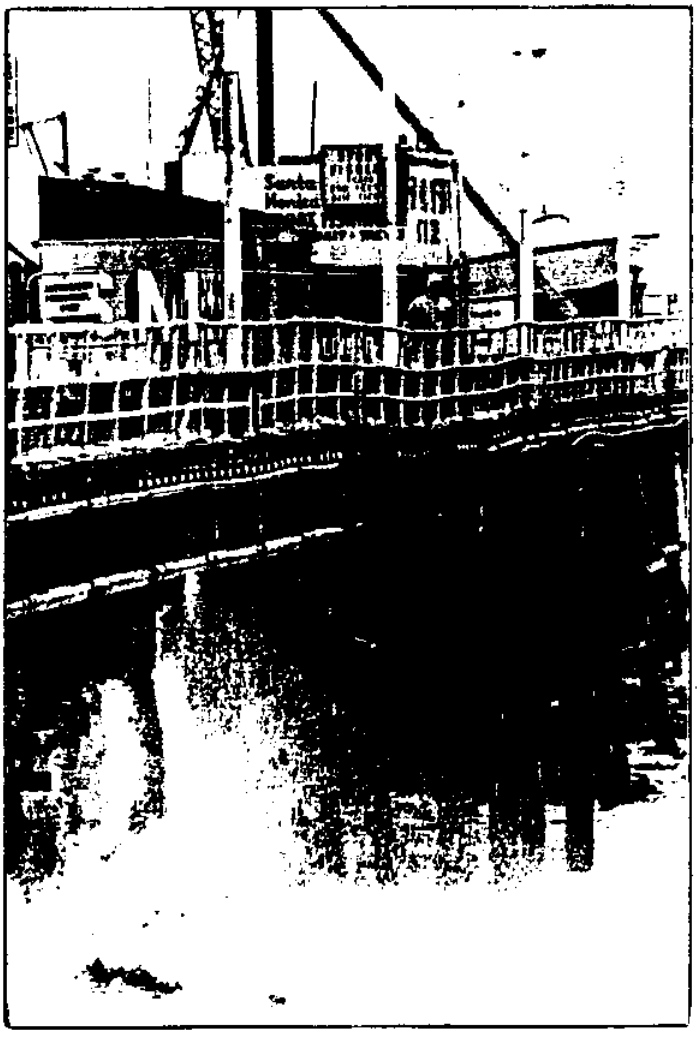

Fig. 1.1 Santa Monica Pier during a storm. (Courtesy of Evening Outlook, a Santa Monica, Ca. newspaper.)

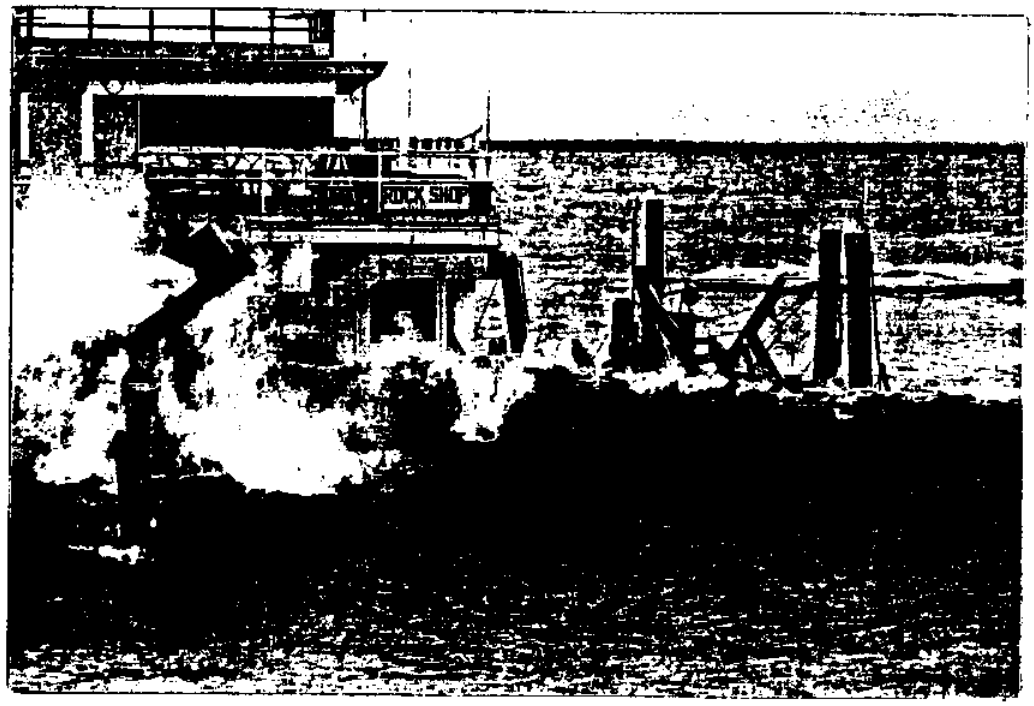

Fig. 1.2 Wind-tossed 10- to 12-foot waves impact on Santa Monica Pier during a storm. (Courtesy of Evening Outlook, a Santa Monica Ca. newspaper.

CHAPTER 2

LITERATURE SURVEY

2.1 General Fluid Loading On Marine Structures

An understanding of wave impact on marine structures has developed during the past decades and is continuing to develop through analytical and experimental methods. The general problem of hydrodynamic impact has been studied extensively for slender members of ocean structures and for large gravity structures involving components of relatively large sections. The uplift wave loading on a horizontal platform has been studied by several investigators through experimental and analytical methods, but as yet no clear mathematical model for flow hydrodynamic beneath the platform region has been developed. In this chapter, a survey of previous work is presented, but attention is focused mainly on wave impact on horizontal and rigid platforms.

There is considerable body of literature concerning wave-structure interaction for computation of wave forces on marine structural members. There are basically two different methods used for computation of fluid loading on

fixed or floating gravity structures, depending upon the relative dimensions of the structural members. Morison (1953) developed an empirical formula for the forces on a vertical slender cylinder. Morison's equation assumes that the fluid forces can be divided into two independent components, the drag force and the inertia force. The drag force is proportional to the square of the water-particle velocity, where the constant of proportionality is known as the drag coefficient C_D. The inertial force, or virtual-mass force is proportional to the horizontal component of acceleration of the particle velocity with a constant of proportionality known as C_M. The values of C_D and C_M have been chosen mainly on the basis of empirical data. In this equation, it is assumed that the fluid forces on stationary slender members in an unsteady motion are given by the linear superposition of a drag force and an inertia force, and the assumption that the kinematics of the undisturbed flow in the region near the structure do not change the incident wave direction. These assumptions are valid for a small ratio of diameter or equivalent section diameter of the structural member to the wavelength, which justifies the absence of wave scattering. However, for ocean structures that are not slender, such as gravity-type platforms or other

structures involving components of large sections, methods based on diffraction theory are used to estimate the wave forces.

Diffraction or potential flow theory refers to the inviscid, incompressible and irrotational solution of fluid-structure interaction corresponding to a fixed or moving body. This method has been described by several authors, including Ippen (1966) and Sarpkaya, et al. (1981). The linear diffraction problem arises when the wave amplitude is assumed sufficiently small. Then, the problem reduces to the solution of fluid-structure interaction satisfying the linearized free surface boundary conditions as well as the radiation condition which requires that at large distances from the structure the scattered wave corresponds to an outgoing wave. The limitations of the linear diffraction theory arise from the assumptions of zero viscosity of the fluid and small amplitude motion, as implied by the applications of the linearized free surface boundary condition. The nonlinear effects become significant only in the case of shallow-water and large-amplitude waves. Friedrichs and Lewy (1948) studied the two-dimensional dock problem as a special case of the problem of waves on a sloping beach with a slope angle of 180 . The problem was presented by

considering one half plane of an infinite water surface covered with a rigid plate against which sinusoidal waves of small amplitude propagate from the positive x-axis. The water flow was described by a complex potential function from which the velocity components could be derived, along with linear boundary conditions for the free surface. It was shown that there were two standing-wave solutions, one permitting the potential function to have a logarithmic singularity at the dock edge, leading to infinite wave height there and the other by considering a bounded solution leading to a finite-amplitude wave at the seaward edge of the dock.

2.2 Experimental Studies of Wave Uplift Pressure on Platform

El Ghamry (1963) performed an investigation, which concerns the prediction of wave forces that act vertically on a horizontal, even-bottom deck under the action of periodic waves. The main objectives of his investigation were: 1) to study the nature of the forces acting on a horizontal deck under the action of breaking and nonbreaking periodic waves and for certain geometrical conditions; 2) to determine the feasibility of using the existing theories in predicting the magnitude of these

forces; 3) to correlate these forces with measurable wave parameters; 4) to study the instantaneous pressures at some points along the deck; and 5) to provide information about the effects of some geometrical parameters on the relationships between the induced forces and the wave characteristics. (El Ghamry, 1963, p. 7).

In his theoretical consideration of nonbreaking waves, El Ghamry made use of Stoker and Fleishman's theory for floating bodies in shallow water, in which linearized version of potential fluid theory for free surface flow was used. He derived a relation for pressure distribution under the deck by substituting of potential function for simple harmonic waves into a linearized form of Bernoulli's equation.

In El Ghamry's experimental study, the dock model was placed in a wave tank 1.0 ft. wide, 3.0 ft. deep and 105 ft. long. A flap-type wave generator was located about 7 feet from one end of the flume. The dock was 4.0 ft. long and nearly as wide as the wave tank. To absorb unwanted wave reflections, a vertical wave absorber made of aluminum metal borings was placed behind the flap wave generator, and a long flat beach-type wave absorber was used at the opposite end of the channel. To measure the

pressure, two strain gauge-type pressure transducers were installed on the dock.

The wave pressures on the dock were measured for three cases, nonbreaking waves with no beach, waves breaking on a 1:5 slope without air entrapment and waves breaking on 1:5 slope with complete air entrapment.

For the case of nonbreaking waves, the tank bottom was kept horizontal beneath the dock and no beach was installed. He also concluded that the dock can be an efficient breakwater if a sufficient length and a proper underside clearance is used. The transmitted wave was found to be composed of different amplitude and phase shift.

For the case of breaking waves, the experiment was conducted on a beach slope. The statistical distribution of peak pressure within a cycle was found to be Gaussian for both cases both with and without air entrapment. For waves breaking on a 1:5 beach slope with no air entrapment, the total force was characterized by the existence of two peaks in each cycle. The first peak was due to the wave action before breaking and the second peak was caused by the wave after breaking. For the same condition of wave breaking but with complete air

entrapment, the pressure records indicated an impulsive shock component. The mean peak pressure in this case was about twice as high as when air was not trapped. The relative magnitude of both peaks was found to depend significantly on the wave period.

Wang (1967) studies wave pressure on a horizontal pier for the case of rigid, smooth, and horizontal platforms, and constant-depth ocean floor. His theoretical analysis was based on linear theory. He considered a general impulse-momentum relation for the impact pressure in terms of the mass of the amount of water responsible for the impact, and the effective velocity at the instant of contact. One important feature in the analysis concerned the estimate of this mass and the effective velocity. Wang adapted an approximation analysis, considering this mass of water to be equal to the mass contained in a semi-cylinder with the length of the pier and diameter of wetted length of the pier. The effective velocity was considered to be the vertical particle velocity of the free surface at the instant of contact. Wang then derived a relation for impact pressure, stating that the impact is proportional to the product of the vertical component of the water velocity at the point of contact and the rate of change of wetted

length at the instant of impact. To determine the slowly varying pressure, he made use of the Eulerian equation for an element of fluid in vertical direction, and derived a relation for slowly varying pressure in terms of incident wave characteristics.

In relation to slow varying pressure, wave characteristics of an undeformed wave at an elevation of the platform were used. This relation simply states that the slowly varying uplift pressure consists of two parts, the hydrostatic pressure and the pressure due to vertical local acceleration. For gravity waves, the vertical acceleration does not exceed the acceleration of gravity. Then the pressure head is equal to one to two times that the elevation of the local water surface, less the elevation of the platform above the still-water level. These relations for impact pressure and slowly varying pressure were applied in the analysis of standing wave, periodic progressive waves, and dispersive waves striking a narrow pier.

Wang conducted some experiments on dispersive waves as incident waves. The experiments were performed in the dispersive wave basin of the Naval Civil Engineering Laboratory. The wave basin is 95 ft. long, 92 ft. wide,

and 3 ft. deep. The test pier was a plexiglas plate 6 ft. by 1 1/2 in. The leading edge of the pier was wedged to 25 degrees in order to minimize the effect of horizontal impact force by the incident waves. The uplift pressure on the underside of the pier was measured by transducers placed on the underside of the pier at different locations from the leading edge of the pier. Two types of transducers were used to permit a complete measurement of the pressure induced by the waves on the underside of the pier. One was used for measuring slowly varying pressure, and the other (with its high natural frequency) measured shock loading with a rise time of microseconds. Waves generated by a plunger-type wave generator.

From Wang's experiment, it was concluded that the presence of the pier causes the waves to be attenuated in height, but their length and period remain almost unchanged. In the data reduction of the slowly varying pressure, the maximum components showed a wide range of scatter, but within the predicted range. The recorded impact pressures correlated poorly with theoretical values. Wang also suggested an empirical relation for estimating the duration of impact, which correlates the impact duration to the square root of a wave height by a

constant factor, varying between 15 and 40.

French's work (1969) is, to the writer's knowledge, the latest study of wave uplift pressure on horizontal platforms with positive soffit clearance. A rational analysis was derived for the nonuniform, unsteady, two-dimensional flow beneath the platform region as the wave strikes. The analysis was based on the assumptions that the viscosity and surface tension and the effect of air entrainment are neglegible; that the form of the free surface wave profile remains unchanged, meaning the celerity of propagation is constant for all points on the profile; that the induced fluid-particle velocity at the seaward edge of the platform by the incident wave and the water surface elevation at the seaward edge are not affected by the presence of the platform; that the pressure is hydrostatically distributed; and that the fluid velocity is independent of depth. The equation of continuity and equations of motion were then integrated over the flow region near and beneath the platform to derive a relation for the celerity of the wave front and wave of recession as the wave strikes and propagates beneath and in contact with the underside of the platform. The slowly varying uplift pressure, when positive, was related to wave-front celerity; when negative, it was

related to the celerity of wave recession. For both positive and negative slowly varying pressures, the analyses were subjected to the previously mentioned assumptions, and the flow may be approximated by a simple step form. Peak pressure at the wave front was considered to be the pressure at a stagnation point on the underside of the platform. Then, the Bernoulli integral equation was employed between the stagnation point and a point on the water surface far ahead of the wave.

The experimental study was performed in a horizontal channel 610 mm deep by 400 mm wide by 30 m long. A piston-type wave generator was used at one end of the channel to generate solitary waves as incident waves. The platform was made of an anodized aluminum plate 13 mm thick, and had a flat, horizontal underside with a flat vertical front face spanning the full width of the tank. The wave generator consisted of a flat vertical plate nearly as thick as the tank cross-section and a cam-driven piston generator. The plate was driven by a mechanical linkage in a time-displacement function that could generate the desired solitary waves. Uplift pressure on the platform was measured by a pair of pressure transducers mounted on the underside of the platform, one 12.8 mm in diameter and the other 3.2 mm in diameter. To

avoid the problem of spatial resolution it was found that it was necessary to use a sufficiently small transducer whose radius is less than one third the characteristic half-width of the pressure distribution to be measured. Despite the use f the smallest commercially available pressure transducer, the problem of spatial resolution could not be avoided entirely. An extrapolation procedure was employed to handle this problem. Another difficulty was a significant shift in output signal due to changes in temperature. This was due to the silicon semiconductor transducing element which was a heat source because it carries an electric current. The heat was conducted away from the platform and from the surrounding environment. When the wave was propagating beneath and in contact with the platform, the rate of heat conduction was significantly increased, causing a shift in pressure signal output. To solve the temperature shift, it was first decided to reduce the excitation voltage to the amount of heat generated. But this resulted in a small output voltage. A second alternative was to heat the water in the tank, which was found to be impractical because of the problem of temperature control. Finally, the problem was partially solved by mounting the transducer in an adaptor with an oil-filled chamber sealed

with an external diaphragm of polyethylene.

From French's experiment, it was concluded that the peak pressure was intrinsically subjected to considerable variance, because of the spume and entrained air in the flow near the wave front. However, the correct peak pressures for different incident wave systems increase with respect to wave height and decrease with increasing soffit clearance. With respect to the slowly-varying pressure, it was found that the positive slowly-varying pressure depends on wave height and soffit clearance, and the negative slowly-varying pressure depends on soffit clearnce, location, and with little dependence on wave height. The ratio of the durations of positive uplift pressure to negative uplift pressure decreases with the increase of the relative distance of measurement at a particular point from the upstream edge of the platform. Because of the severe oscillations in the pressure records, it was difficult to determine meaningful values of time of zero pressure. A curve was fitted through the region of oscillation to represent the mean value about which pressures varied.

CHAPTER 3

THEORETICAL CONSIDERATIONS

3.1 The Physical Problem

The theoretical aspects of the problem can be described by referring to Fig. 3.1 that shows the series of events which take place as a solitary wave approaches from $x=-\infty$ and strikes a fixed and rigid platform.

The two-dimensional case considered consists of a fluid region of constant depth, above which a platform, with underside clearance, S, is fixed. The fluid region has a depth of d and extends from $x=-\infty$ to $x=+\infty$. A solitary type of wave is chosen as an incident wave since it could represent a relevant model of ocean waves in shallow water, where piers or platforms are usually situated. This wave has a height, H, greater than the clearance, S, of the platform.

Initially, the wave approaches the platform from $x=-\infty$. As the wave strikes the platform, it continues to propagate beneath and in contact with the platform. A reflected wave disturbance propagates in the opposite direction from the platform. The transmitted wave, as it

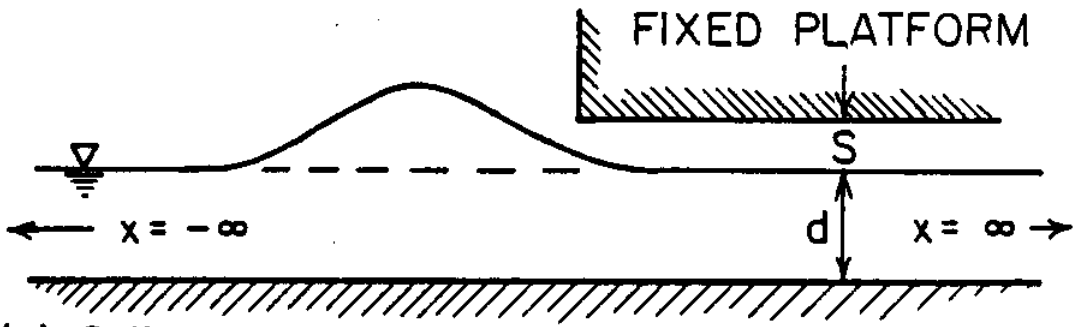

(a) Solitary wave approaching the platform shoreward.

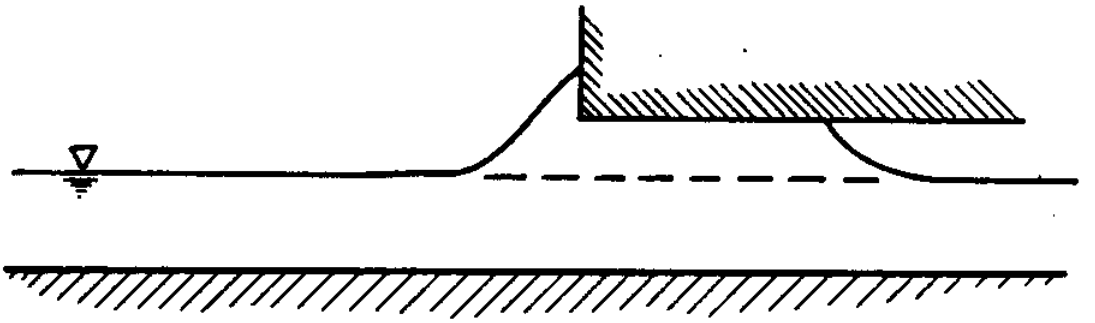

(b) Solitary wave striking the platform, causing uplift pressure.

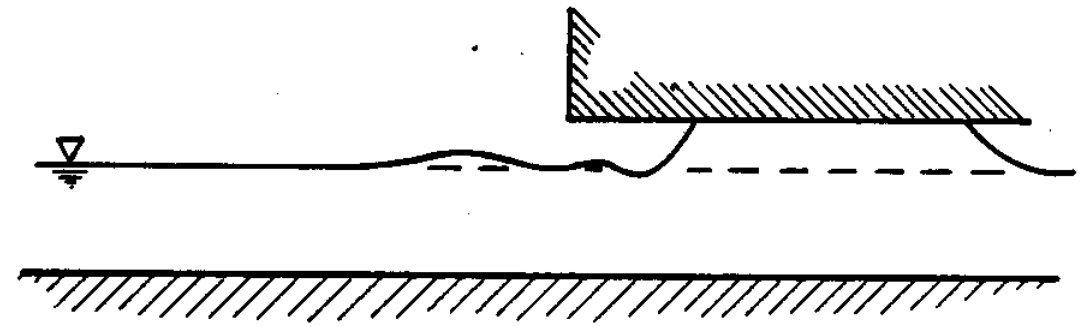

(c) Solitary wave propagating beneath and in contact with platform.

Fig. 3.1 Events taking place, as a solitary wave approaches a platform of horizontal soffit and positive clearance.

continues to propagate beneath and in contact with the platform, causes an initial peak pressure of large magnitude and very short duration, followed by a slowly varying uplift pressure of smaller magnitude but of considerable duration, which is initially positive and then negative (French, 1969).

3.2 Mathematical Formulation of Free Surface Flow

To introduce the basic system of equations governing free surface flows, we consider a two-dimensional flow situation in which a wave is propagating in water of constant depth, d, in a region of infinite horizontal extent. It is assumed that the wave maintains a permanent form and that there is no underlying current.

A definition sketch of the coordinate system is presented in Fig. 3.2. In this fixed Eulerian frame of reference, the x-coordinate is located along the still water surface, with the y-coordinate directed upward.

The displacement of the free surface from the still-water level is $\eta(x,t)$. The wave induces a flow field (u,v) where $U(x,y,t)$ and $V(x,y,t)$ are the horizontal and vertical velocity components, respectively, and t is the time.

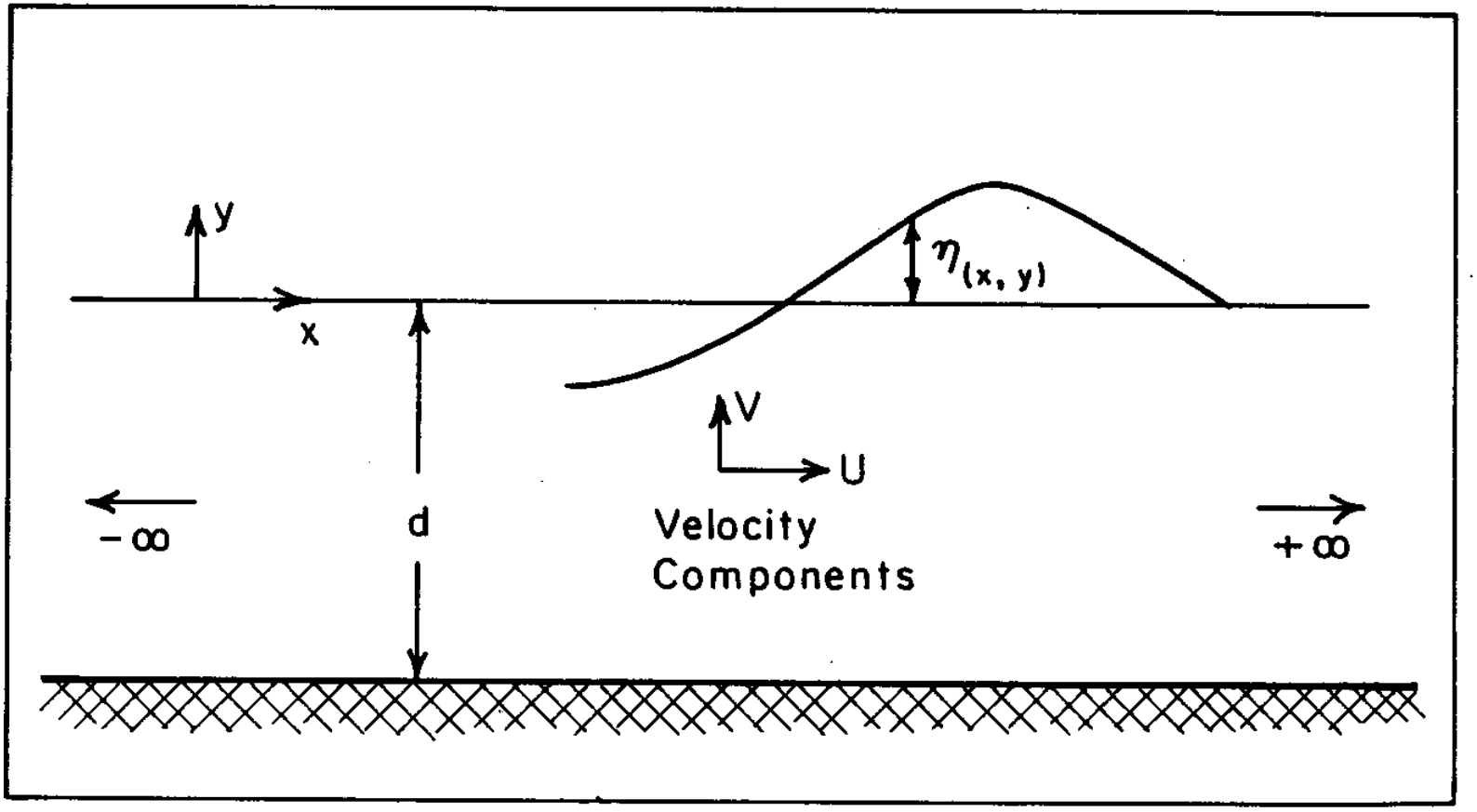

Fig. 3.2 Definition sketch of free surface flow problem.

3.2.1 Governing Equations

To simplify our analysis, the following physical reasonable assumptions are made which are valid approximations for many free-surface phenomena:

1. Incompressible homogeneous fluid
2. inviscid
3. Irrotational
4. Negligible surface tension
5. No air entrainment

Then the governing hydrodynamic equations are: the continuity equation;

$$u_{,x} + v_{,y} = 0 \tag{3.1}$$

the equations of motion in the x-direction;

$$u_{,t} + uu_{,x} + vu_{,y} + \frac{1}{\rho} P_{,x} = 0 \tag{3.2a}$$

the equations of motion in the y-direction;

$$v_{,t} + uv_{,x} + vv_{,y} + \frac{1}{\rho} P_{,y} + g = 0 \tag{3.2b}$$

and, the equation of vorticity,

$$u_{,y} - v_{,x} = 0 \tag{3.3}$$

Assumptions of inviscid, irrotational, and incompressible flow can be used to define a velocity potential $\phi(x,y,t)$. The velocity vector may be expressed as the gradient of a velocity potential; i.e.,

$$q = \nabla\phi$$

where $q(x,y,t) \equiv (u,v)$, is the velocity vector with u,v in the x,y directions, respectively, and the gradient operator ∇ defined as $\frac{\partial}{\partial x} i + \frac{\partial}{\partial y} j$. From the continuity equation for an incompressible fluid

$$\nabla \cdot \vec{q} = 0$$

and using the definition of the velocity potential, Laplace equations are obtained

$$\nabla \cdot \vec{q} = \nabla^2\phi = 0 \quad -d \leq y \leq \eta \tag{3.4}$$

3.2.2 Boundary Conditions

To solve the Laplace equation for a given body of fluid, it is necessary to define the boundary conditions on all boundaries of the fluid domain. Typical boundary conditions can be summarized as follows:

(i) Dynamic boundary condition at the free surface:

This condition imposes a constant pressure at the free surface

$$p = P(x,t) \quad \text{on } y = \eta$$

For inviscid flow and surface tension effects to be negligible, this condition is implemented through the Bernoulli equation which can be derived by substitutions of Eq. (3.3) into (3.2) and the integration of the latter equations. Then the Bernoulli equation in terms of velocity potential is

$$\phi_{,t} + \frac{P}{\rho} + \frac{1}{2}(\phi_{,x}^2 + \phi_{,y}^2) + g\eta = F(t) \quad \text{on } y = \eta$$

Without loss of generality, the pressure at the free surface can be taken to be equal to zero, and F(t) can be absorbed into the potential function. Then we have,

$$\phi_{,t} + \frac{1}{2}(\phi_{,x}^2 + \phi_{,y}^2) + g\eta = 0 \quad \text{on } y = \eta \qquad (3.5)$$

(ii) Kinematic boundary condition at the surface:

This describes the condition in which the fluid particle velocity normal to the free surface is equal to the velocity of the free surface itself in that direction, or a particle of fluid will always remain on the free surface.

The equation of the free surface can be written as

$$y - \eta(x,t) = 0$$

In order for this condition to be satisfied, we must have

$$\frac{D}{Dt}(y-\eta) = 0$$

Then, in terms of velocity potential, we have

$$\eta_{,t} + \phi_{,x}\eta_{,x} - \phi_{,y} = 0 \quad \text{on } y = \eta \tag{3.6}$$

(iii) No flow through the bottom boundary:

Finally, the boundary condition on the impervious boundary states that the velocity component normal to the boundary is zero

$$\phi_{,y} = 0 \quad \text{on } y = -h \tag{3.7}$$

The difficulty of the problem lies in the nonlinearity and coupling of the boundary conditions at the free surface, which is in motion. The free surface elevation is an unknown a priori and must be determined from the solution of the problem, along with Laplace Eq. (3.4) on the interior of the fluid region as well as the equations on the free surface.

Most wave theories satisfy the Laplace equation and the bottom boundary condition exactly. Then the different specializations of the free surface boundary conditions

give rise to different classes of solutions. But simplification without careful study of the problem, leads to qualitatively incorrect results.

3.3 Classes of Available Solutions

In the case of small motion (wave amplitude and velocity considered are small), the nonlinear terms of Eqs. (3.5) and (3.6) may be neglected. Furthermore, for small amplitude, these conditions may be applied at the original undisturbed surface level. The free surface displacement η can be eliminated between the linearized versions of equations; then, the resultant equation is

$$\phi_{,tt} + g\phi_{,y} = 0$$

The whole class of solutions to this equation is termed linearized solution or first-order wave theory, and the surface configuration is characterized by sinusoidal motion. The validity of the linearized equation is expressed by the inequalities

$$\frac{H}{L} << 1$$

$$\frac{H}{d} << 1$$

where H, L, and d are wave amplitude, wave length, and still-water depth. For small-amplitude waves, these inequalities are considered satisfied.

In order to treat finite amplitude waves, higher order approximations are required. Then the convective acceleration term cannot be set equal to zero, as was done for small amplitude waves.

To seek an exact analytical solution is almost impossible, as has been noted by many authors. Analytical solution is usually carried out by series solution and by using general perturbation schemes. In this case, a series solution for the potential functions is considered as

$$\phi = \sum_{0}^{\infty} \varepsilon^n \phi^n$$

where $\varepsilon << 1$ is a perturbation parameter. If this expansion is carried out to second-order, then the solution leads to Stoke waves. Stokes employed a successive approximation technique by inclusion of a large number of harmonic functions in series representation. But this is usually inconvenient and unsuitable for general solution of large-amplitude waves over a complete range of depths.

With the advent of high-speed computers, it is usually desired to solve the full nonlinear free surface equations as well as the Laplace equation in the interior regions by numerical methods. The difficulty arises from

the fact that the free surface boundary conditions cannot be handled by the usual means because the free surface is in motion. This is usually handled by repeated application of some numerical computational steps in sequence to construct the motion of the free surface. There have been previous studies to develop techniques for solving full nonlinear free surface problems with the advantage of being computationally stable and efficient. For long-term computations, the truncation errors of finite difference approximations of derivations are accumulated which will lead to unstable solutions. These errors are particularly bothersome in the presence of nonlinear advective terms and the coupling of free surface boundary conditions. The instability is usually observed by free surface oscillations which cause the computations to stop.

A major difficulty in long-term numerical integration of the equation of fluid motion by finite difference methods has been the nonlinear computational instability of the finite difference analogies of the governing differential equations, unless the finite difference expression for the advection term is restricted to a form which properly represents the interaction between grid points. One of the successful methods that was designed

to calculate the flow of a viscous incompressible fluid with a free surface is the Marker-and-Cell (MAC) method which is developed by Harlow and Welch (1965). The MAC method is based on a Eulerian finite difference model for the equations of continuity and the Narier-Stokes equations. The fluid surface is defined by a Lagrangian line, and the coupling between the equations in the interior and the equation on the Lagrangian is carried out by Marker particles that move through the stationary network of cells. The criticism of the MAC method is the lack of consistency between the particle model for the free surface and the finite difference model for the fluid region when the free surface is not regularly shaped. Several modifications to improve the free surface representation have been suggested by several authors, including Nichols and Hirt (1971).

There has been an effort to use the Galerkin method to solve large free surface problems. Preko (1968) and Easton and Catton (1972) used a combined analytical-numerical method which involved no linearization of free surface equations to compute such motions. In their method, the full nonlinear free surface equations were integrated numerically and were matched to a series solution of the continuity equation in the

interior region by the Galerkin method. Since the recent development of the finite element methods to flow analysis, great interest has been shown in finite element formulation of free surface problems in order to handle irregular and more general boundary conditions. A Eulerian-Lagrangian finite element has been formulated by several authors for incompressible flows with a free surface. Hughes, Liu, and Zimmermann (1978) used a mixed Lagrangian-Eulerian finite element scheme to solve incompressible viscous flows. Wellford and Ganaba (1981) developed a finite element scheme with a hybrid Langrange line to solve inviscid free surface problem.

The conclusions to be drawn from the above discussion are that linearization of any form must be avoided in free surface flow problems involving large free surface motions, and that the method of solution must provide minimum truncation errors, such as finite difference analog of derivatives, to avoid amplification of these errors by nonlinear terms. Some further conclusions may be drawn regarding a technique by which to handle the free surface boundary conditions, since the free surface is in motion and cannot be handled by the usual means. The computational procedure must also provide a consistent coupling mechanism for approximate solution of the

interior region and approximate solution of the free surface boundary.

3.4 Method of Solution

In the present study, our intention is to solve the full nonlinear free surface boundary condition along with the Laplace equation and solid boundary conditions by a finite element scheme. To handle a moving free surface, we adopt a mapping technique to transform the fluid region and its boundary into a regular geometry. Since it is necessary for the class of solutions proposed to be associated with some geometry, and some initial condition, the equations will be specialized to a two-dimensional, flat-bottom region, propagation of a solitary wave is considered.

A definition sketch of the solution domain is presented in Fig. 3.3, showing initially a solitary wave of height H propagating into a still water of constant depth d. The interior domain Ω contains an inviscid incompressible fluid. The flow is assumed to be irrotational. The boundary $\partial\Omega_1$, represents the free surface of the flow. The boundary $\partial\Omega_2$ represents a spatially fixed bottom on which fluid velocities are equal to zero.

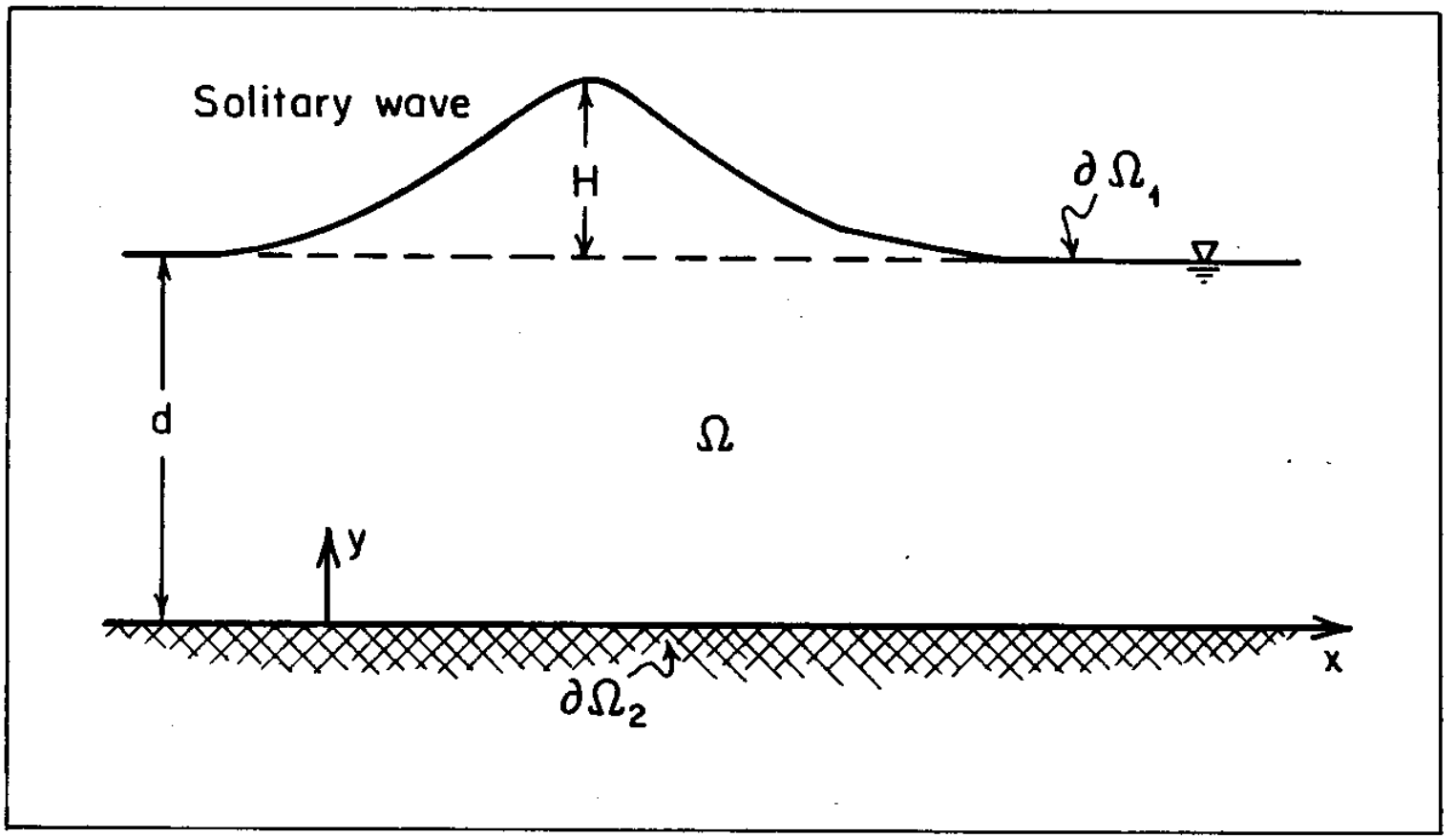

Fig. 3.3 Definition sketch of the solution domain.

Recalling the equations for free surface motion from previous sections

$$\phi_{,xx} + \phi_{,yy} = 0 \quad \text{in} \quad \Omega \tag{3.4}$$

$$\phi_{,t} + \frac{1}{2}(\phi_{,x}^2+\phi_{,y}^2) + g\eta = 0 \quad \text{on} \quad \partial\Omega_1 \tag{3.5}$$

$$\eta_{,t} + \phi_{,x}\eta_{,n} - \phi_{,y} = 0 \quad \text{on} \quad \partial\Omega_1 \tag{3.6}$$

$$\phi_{,y} = 0 \quad \text{on} \quad \partial\Omega_2 \tag{3.7}$$

To solve these equations with corresponding boundary conditions over the problem domain, a finite element approximation technique is employed. To ensure that a small number of elements can represent the curved free surface boundary, distorted rectangular-type elements are used. Isoparametric mapping is used as a technique to handle the free surface motion. No matter how large the free surface motion is, by this technique, the physical domain is mapped into a regular domain. The inherent idea of this technique is general and could be easily extended to analyze the problem involving free surface problems. The governing equations are then written in terms of regular domain coordinate. To apply the finite element analysis, the conventional discretization procedure of the

Galerkin weighted residual method is employed for approximation of the equations.

3.5 Discussion of the Assumptions

The previously made assumptions have permitted the development of potential flow analysis for wave impact on a horizontal platform. We shall now proceed to discuss the effect of each assumption in the flow region beneath the platform and, in particular, on the uplift pressure on the platform.

The assumption that viscosity has a negligible effect in our problem may be examined by analysis of Reynolds number and boundary-layer development. The Reynolds number for a rigid body of a given shape in a flow field is defined as

$$Re = \frac{LU}{\nu}$$

Where L is a length representing the linear dimensions of the body, U is the flow velocity characteristic, and ν is the kinematic viscosity of the fluid. The Reynolds number is a measure of the ratio of representative magnitude of inertia forces to that of viscous forces. When the Reynolds number is sufficiently large, viscous forces often play a negligible part in the equation of motion over nearly the whole flow region. According to the

Prandtl boundary-layer theory (Currie, 1974; p. 282) the pressure is independent of the transverse coordinate in boundary layers, then the pressure distribution along the boundary layer will be the same as that of the outer flow, providing that the thickness of boundary layer is much less than a characteristic length. When the boundary is a flat plate, the thickness δ which is defined as the distance y from the solid boundary, is

$$\delta/x = 5\ Re^{-1/2} \quad \text{Laminar boundary-layer}$$

$$\delta/x = .38\ Re^{-1/5} \quad \text{Turbulent boundary-layer}$$

In the present problem, the characteristic length of the body, such as the platform length, is large, and the viscosity of water is quite small, thus providing a sufficiently large Reynolds number Re. The effect of viscosity can therefore be neglected with a good approximation without affecting the uplift pressure on the platform.

Since the motion of a fluid at a large Reynolds number approximates that of a completely inviscid fluid, the assumption of irrotationality can be examined for the case of inviscid fluids. According to Kelvin's circulation theorem that has been established for an inviscid incompressible fluid of uniform density, a body

of inviscid fluid in irrotational motion continues to move in a manner wholly irrotational. When the incident wave propagates beneath and in contact with the platform, the flow condition beneath the platform resembles the flow between parallel plates. The main flow region can be considered to be irrotational since the motion induced by the incident surface wave before it strikes the platform may be assumed to be irrotational and vorticity diffuses across the surface bounding the fluid only by viscosity.

The assumption that surface tension has a negligible effect on pressure may be examined by considering the Bernoulli equation with the surface tension term included. The Bernoulli equation with surface tension for two-dimensional case can be written as

$$\frac{P}{\rho} + \phi_{,t} + \frac{1}{2}(\phi^2_{,x}+\phi^2_{,y}) + g\eta + \frac{\sigma}{\rho r} = 0$$

where σ is the surface tension per unit length and r is the radius of curvature of the interface. The importance of surface tension is usually expressed by a Weber, number which is a ratio of internal forces to surface tension force, i.e.,

$$We = \frac{\rho U^2 L}{\sigma}$$

where U is a velocity characteristic and L is a length

characteristic. When the Weber number, We, becomes large, the relative importance of surface tension force becomes very small compared with inertial force. The effect of surface tension is to increase the propagation speed of the wave, but for long waves the effect of surface tension can generally be neglected (Weigel, 1964, pp. 60).

For a platform of moderate geometric length scale, the Weber number We is sufficiently large and therefore the effect of surface tension force is negligible. Also, when a wave is propagating beneath and in contact with the platform, the radius of curvature of the interface of water is infinite for a smooth and horizontal platform, so the surface tension term can be neglected in Bernoulli equations with a good approximation.

Because of presence of friction and turbulence in the real case, there is always some effect of air bubble entrainment in the flow near the interface. Air bubbles entrained in the flow may cause some energy dissipation, as in a hydraulic jump in an open channel. This can be reduced by employing incident waves of moderate amplitude.

CHAPTER 4

NUMERICAL ANALYSIS

FINITE ELEMENT FORMULATION

The finite element method is a numerical approximation method of solving partial differential equations of boundary and initial value problems. This method was originally developed for structural problems, and its application was later expanded to nonstructural problems such as those involving fluid. Potential flow problems using finite element method was first initiated by Zienkiewicz (1977).

In the finite element analysis, the flow field is divided into small subregions called finite elements. These elements may be of variable sizes and shapes and their behavior is modeled adequately by writing differential equation as a linear combination of appropriate interpolation functions at nodes. Variational principles or weighted residual method are usually used for discretization of governing equations for local elements. Finally, these local elements are assembled to form a global system of differential or algebraic equations. Then the nodal values of the variables are

computed from the resulting system of equations.

4.1 Discretization of Physical Domain

For infinite flow domains, such as long channels, it is necessary to establish the significant zones to be included in the finite element discretization. This will involve determination of the geometrical extents of the zones and of adequate flow conditions on the discretized boundaries. For propagation of a solitary wave, it is assumed that its amplitude is zero for a small ratio of η/H, then the flow region could be considered undisturbed beyond the effective wave length of the solitary wave. The criteria for the evaluation of significant extents is then based on the distance of wave propagation. For discretization of the flow domains, we first consider a bounded domain that can be extended to a larger domain, simply by increasing the number of finite element modes.

In order to construct the finite element model for our problem, the region is discretized into six-node finite elements, (two midside nodes), either entirely into uniform or nonuniform generic length Δx. The curved-free surface boundary is approximated with straight-line segments to avoid the poor curve fitting properties of higher order polynomials. The ordinates of elements

represent the location of the free surface boundary. A typical finite element mesh for the flow region is shown in Fig. 4.1.

To develop a technique for handling the free surface motion, isoparametric finite element mapping is used to transform the physical domain into a regular nodal domain. Isoparametric is one of the natural coordinates since it uses nondimensionalized coordinates. The reason for using isoparametric element is derived from the fact that the same parametric function which describes the geometry may be used for interpolation of unknown functions within an element. Isoparametric mapping provides a one-to-one correspondence between the local coordinate (ξ,η) and the global Cartesian coordinate (x,y). Each element is related to parent element whose intrinsic coordinates (ξ,η) lie in the domain $(-1,+1)$. For each element, the coordinate transformation between the physical and parent element is given by

$$x = \sum_{i=1}^{N} \Psi_i(\xi,\eta) x_i \qquad (4.1a)$$

$$x = \sum_{i=1}^{N} \Psi_i(\xi,\eta) y_i \qquad (4.1b)$$

Where x,y are the coordinates of any point of the

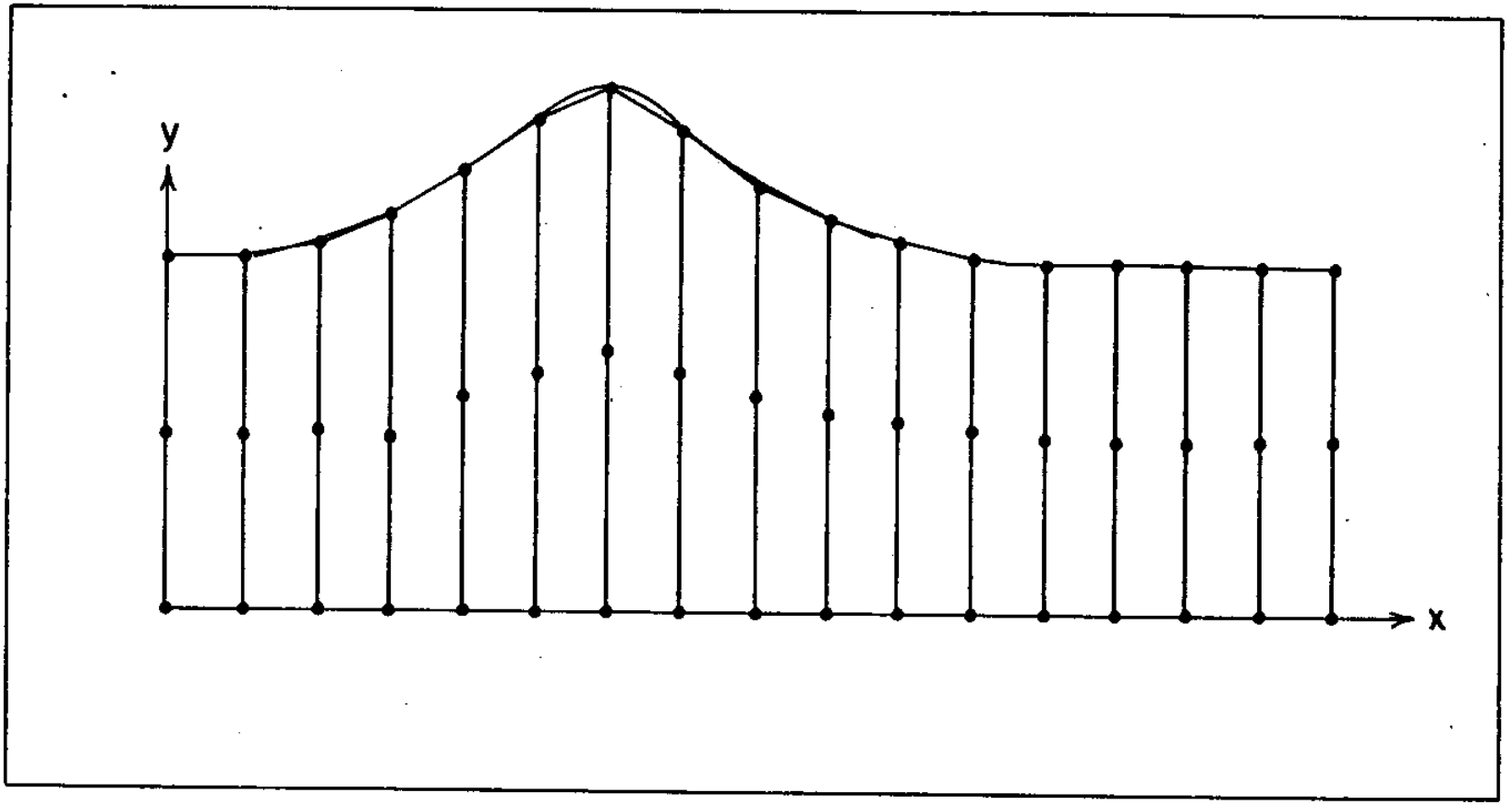

Fig. 4.1 Typical finite element mesh for the flow region.

element and x_i , y_i , i=1,...,6 are the global coordinates of the element modes. The interpolation function Ψ_i, are given in terms of the local coordinates to which a set of global Cartesian coordinates will correspond. The fundamental property of the interpolation function Ψ_i is that its value in the natural coordinate of system is unity at node i and is zero at all other nodes.

To construct the interpolation functions corresponding to the six-node elements in the physical domain, Lagrange interpolation tensor product is used, since rectangular types of elements (Lagrange family) are employed in the parent plane. This can be achieved by simple products of appropriate Lagrange polynomials in the two coordinates. Thus, in two dimension, if we label the node by its column and row number, I,J, we obtain

$$\Psi_i(\xi,\eta) = \Psi_{IJ}(\xi,\eta) = \alpha_I^n(\xi)\beta_J^n(\eta)$$

Where n and m are the number of subdivisions in each direction,and

$$\alpha_I^n(\xi) = \prod_{\substack{K=1 \\ K\neq I}}^{n} \frac{(\xi-\xi_K)}{(\xi_I-\xi_K)} \qquad (4.2a)$$

$$\beta_J^m(\eta) = \prod_{\substack{M=1 \\ M\neq J}}^{m} \frac{(\eta-\eta_M)}{(\eta_J-\eta_M)} \qquad (4.2b)$$

with Π denoting a product of the binomials of Eq. (4.2) over the range of K and M.

Consider the typical element in physical domain and its transform in parent plane shown in Fig. 4.2. With this configuration, the shape functions

$$\Psi_{IJ} = \prod_{\substack{K=1 \\ K\neq I}}^{2} \prod_{\substack{M=1 \\ M\neq J}}^{3} \frac{(\xi-\xi_K)(\eta-\eta_M)}{(\xi_I-\xi_K)(\eta_J-\eta_M)}$$

will take the following forms:

$$\begin{aligned}
\Psi_1(\xi,\eta) &= \frac{1}{4}\,\eta(\eta+1)(1-\xi) \\
\Psi_2(\xi,\eta) &= \frac{1}{4}\,\eta(\eta+1)(1+\xi) \\
\Psi_3(\xi,\eta) &= -\frac{1}{2}\,(\eta+1)(\eta-1)(1-\xi) \\
\Psi_4(\xi,\eta) &= -\frac{1}{2}(\eta+1)(\eta-1)(1+\xi) \\
\Psi_5(\xi,\eta) &= \frac{1}{4}\eta(\eta-1)(1-\xi) \\
\Psi_6(\xi,\eta) &= \frac{1}{4}\eta(\eta-1)(1+\xi)
\end{aligned} \tag{4.3}$$

The midside node numbers 3, and 4 corresponding to the straight sides can be omitted by setting the corresponding interpolation functions equal to zero.

4.2 Transformation of Governing Equations

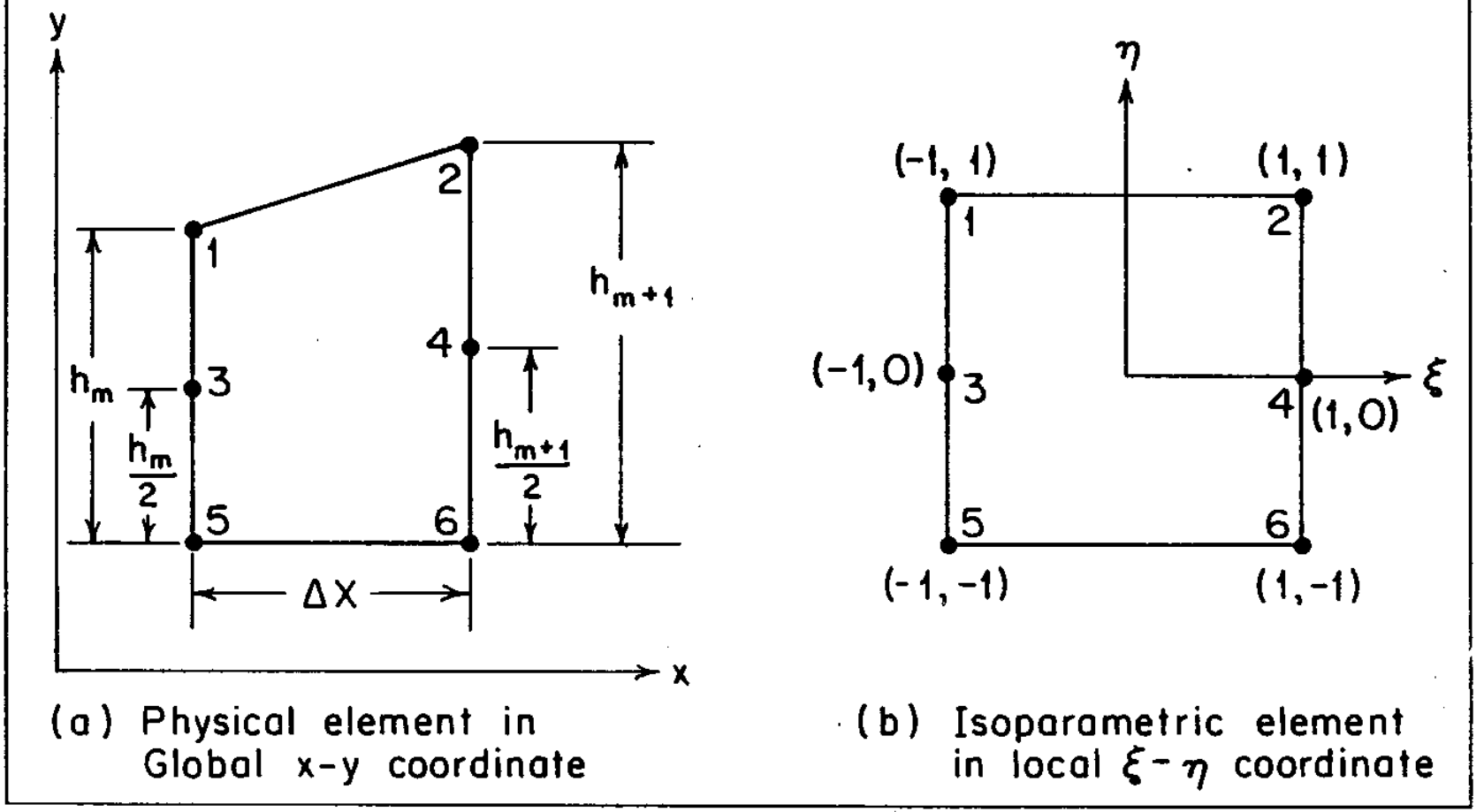

Fig. 4.2 Typical physical element and its transformed isoparametric element.

To perform finite element discretization, the governing equations in a global physical element must be written in terms of the local isoparametric coordinate (ξ,η). This requires that the following coordinate transformation of derivative be invoked. From the chain rule, we write

$$\phi_{,\xi} = \phi_{,x}\, x_{,\xi} + \phi_{,y}\, y_{,\xi}$$
$$\phi_{,\eta} = \phi_{,x}\, x_{,\eta} + \phi_{,y}\, y_{,\eta}$$

or in a matrix form

$$\begin{Bmatrix} \phi_{,\xi} \\ \phi_{,\eta} \end{Bmatrix} = [J] \begin{Bmatrix} \phi_{,x} \\ \phi_{,y} \end{Bmatrix}$$

and inverted as

$$\begin{Bmatrix} \phi_{,x} \\ \phi_{,y} \end{Bmatrix} = [J]^{-1} \begin{Bmatrix} \phi_{,\xi} \\ \phi_{,\eta} \end{Bmatrix} \qquad (4.4)$$

where [J] is the Jacobian matrix

$$[J] = \begin{bmatrix} x_{,\xi} & y_{,\xi} \\ x_{,\eta} & y_{,\eta} \end{bmatrix}$$

Here the derivatives $\phi_{,x}$ and $\phi_{,y}$ are determined from the inverse of the Jacobian and the derivatives $\phi_{,\xi}$ and $\phi_{,\eta}$. The numerical values of coefficients in [J] can be found from the coordinate transformation (Eq. (4.1)) along with the corresponding shape functions (Eq. (4.3)).

The transformation between local isoparametric and global derivatives can now be found by substituting Eq. (4.1) into the inverted chain rule (Eq. (4.4)), using the corresponding shape functions (Eq. (4.3)).

After substitutions and operations, the Jacobian matrix is found to be

$$[J] = \begin{bmatrix} \frac{\Delta x}{2} & 0 \\ \frac{1}{4}(\eta+1)(h_{m+1}-h_m) & \frac{1}{4}h_m(1-\xi)+\frac{1}{4}h_{m+1}(1+\xi) \end{bmatrix}$$

Since mapping the equations from the physical domain to the parent plane involves transformation of the second derivatives, it is necessary to determine the higher derivatives of the coordinate transformation functions. This can be done by direct differentiation of the coefficients in the inverted Jacobian matrix, which is defined as

$$[J]^{-1} = \frac{1}{\det\cdot|J|}\begin{bmatrix} \frac{1}{4}(h_m(1-\xi)+h_{m+1}(1+\xi)) & 0 \\ -\frac{1}{4}(\eta+1)(h_{m+1}-h_m) & \frac{\Delta x}{2} \end{bmatrix} = \begin{bmatrix} \xi_{,x} & \xi_{,y} \\ \eta_{,n} & \eta_{,y} \end{bmatrix} \quad (4.5)$$

Then the differentiation of coefficients in the Jacobian matrix gives

$$\xi_{,xx} = 0 \qquad \xi_{,yy} = 0$$

$$\eta_{,xx} = \left(\frac{8}{\Delta x^2}\right)\left\{\frac{(h_{m+1}-h_m)^2(\eta+1)}{[h_m(1-\xi)+h_{m+1}(1+\xi)]^2}\right\} \qquad \eta_{,xx} = 0 \quad (4.6)$$

The transformation of higher derivatives can then be carried out as

$$\phi_{,xx} = \phi_{,\xi\xi}\xi^2_{,x} + 2\phi_{,\xi\eta}\xi_{,x}\eta_{,x} + \phi_{,\eta\eta}\eta^2_{,x} + \phi_{,\xi}\xi_{,xx} + \phi_{,\eta}\eta_{,xx}$$

and so on. Therefore, Eqs. (3.4) through (3.6) become

$$\xi^2_{,x}\phi_{,\xi\xi} + (\eta^2_{,x} + \eta^2_{,y})\phi_{,\eta\eta} + 2\xi_{,x}\eta_{,x}\phi_{,\xi\eta} + \eta_{,xx}\phi_{,\eta} = 0 \qquad (4.7a)$$

$$\phi_{,t} + \tfrac{1}{2}\xi^2_{,x}\phi^2_{,\xi} + \tfrac{1}{2}\eta^2_{,x}\phi^2_{,\eta} + \tfrac{1}{2}\eta^2_{,y}\phi^2_{,\eta} + \xi_{,x}\eta_{,x}\phi_{,\xi}\phi_{,\eta} + g(h-d) = 0 \qquad (4.7b)$$

$$h_{,t} + \xi^2_{,x}h_{,\xi}\phi_{,\xi} + \eta_{,x}\xi_{,x}\phi_{,\eta}h_{,\xi} - \eta_{,y}\phi_{,\eta} = 0 \qquad (4.7c)$$

In this set of equations, $\eta(x,t)$, representing the free surface displacement, has been replaced by the terms (h-d), where h is the free surface height measured from he bottom, and d is the still water depth. The bottom boundary condition is a natural type of boundary condition that is automatically satisfied as a part of the finite element formulation; so, we simply drop this boundary condition.

The transformed governing equations have more complicated forms than the original governing differential

equations with the advantage that the solution region has a regular rectangular shape in the parent plane. The hidden nonlinearity of the moving free surface is no longer a problem in the transformed plane, because the free surface boundary has been mapped into straight-line segments in the isoparametric plane whose positions have an ordinate of +1 in terms of the natural coordinate. We could generalize the finite element mesh by increasing the number of nodes through the depth, since for a large water depth three nodes may not be enough to model the flow hydrodynamics. This can be done by regarding each rectangular cell in the parent computational domain (Fig. 4.3) as being separately mapped by a local bilinear mapping to a new isoparametric plane. This idea was first presented by Jameson and Caughey (1977) for transonic potential flow calculation using the finite volume method. Finite volume methods use general non-orthogonal coordinates and consider the governing integral equations as balances of mass, momentum and energy fluxes for each finite volume defined by the intersection of the coordinate surfaces. Jameson and Caughey (1977) applied the finite volume method to the steady full-potential equations by using mixed-type flux operators. Instead of assuming a single mapping of the entire region, they used

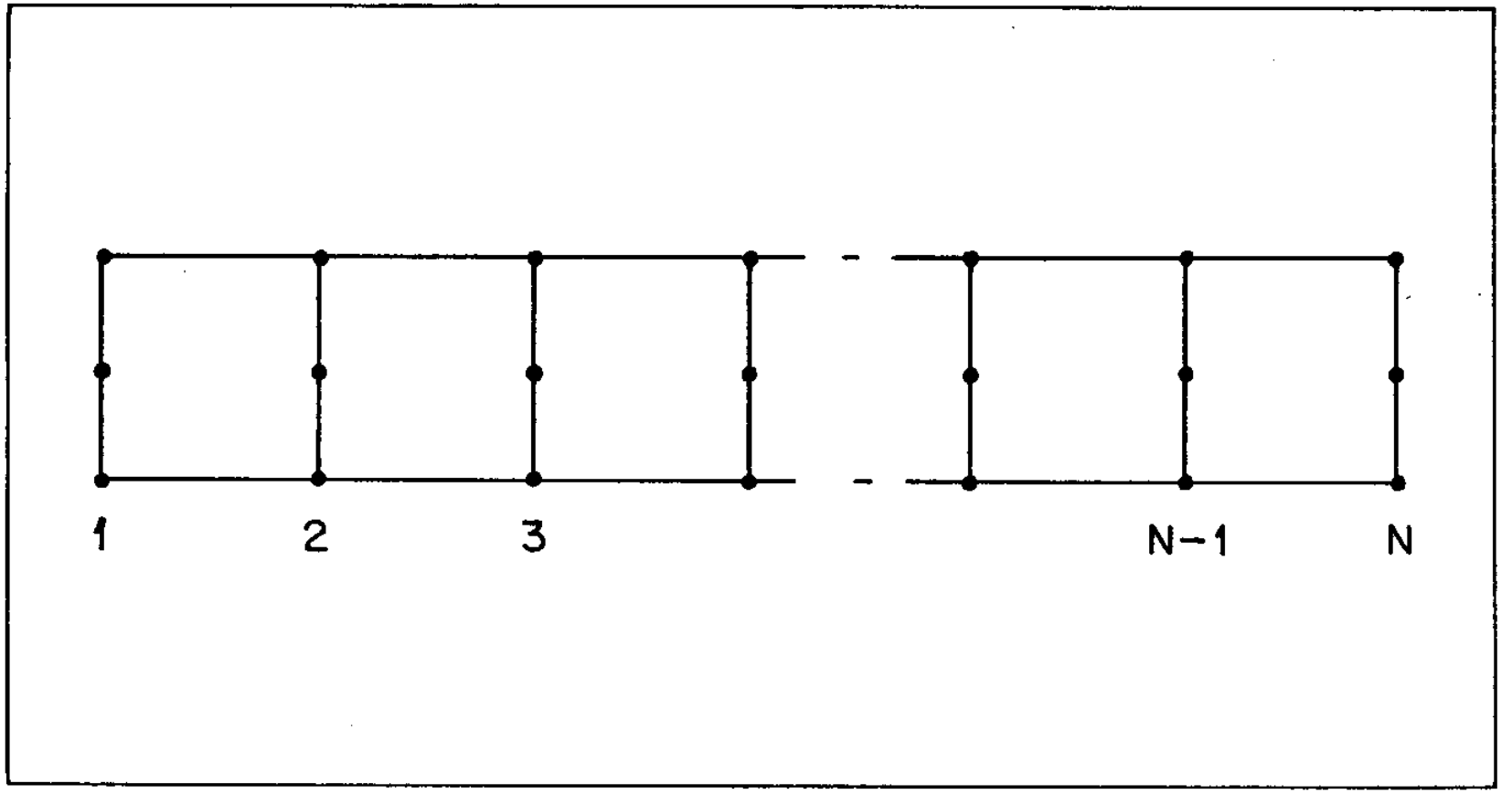

Fig. 4.3 Typical transformed finite element mesh of the physical domain.

a separate mapping for each rectangular cell in computational domain.

Consider the typical rectangular cell in the transformed plane which can be subdivided by four-node standard isoparametric elements (Fig. 4.4). The coordinate transformation is given by

$$\xi = \sum_{i=1}^{4} \bar{\Psi}_i(\bar{\xi},\bar{\eta})\,\xi_i$$

$$\eta = \sum_{i=1}^{4} \bar{\Psi}_i(\bar{\xi},\bar{\eta})\,\eta_i$$

where ξ and η are the coordinates of any point of the element, and ξ_i, η_i, $i=1,\ldots,4$ are the global coordinates of the element nodes. The interpolation functions for a standard four-node isoparametric element are defined as follows:

$$\bar{\Psi}_1(\bar{\xi},\bar{\eta}) = \frac{1}{4}(1-\bar{\xi})(1-\bar{\eta})$$

$$\bar{\Psi}_2(\bar{\xi},\bar{\eta}) = \frac{1}{4}(1+\bar{\xi})(1-\bar{\eta})$$

$$\bar{\Psi}_3(\bar{\xi},\bar{\eta}) = \frac{1}{4}(1+\bar{\xi})(1+\bar{\eta})$$

$$\bar{\Psi}_4(\bar{\xi},\bar{\eta}) = \frac{1}{4}(1-\bar{\xi})(1+\bar{\eta})$$

where the local coordinates $(\bar{\xi},\bar{\eta})$ vary on the interval $(-1,+1)$.

To write the differential equations in terms of the new system of coordinates, we use the chain rule. Then, in a matrix form, we obtain

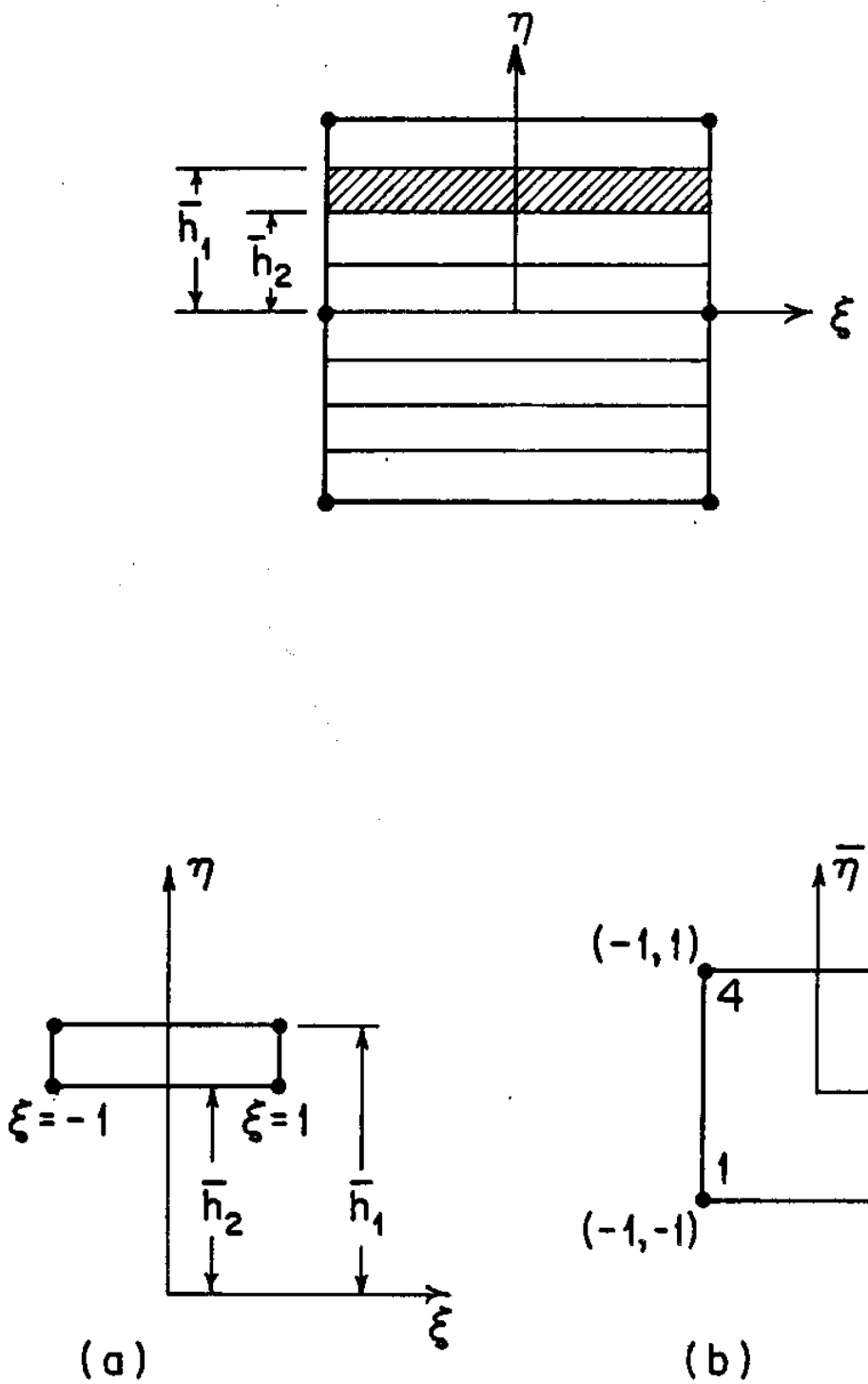

Fig. 4.4 Typical element in rectangular cell and its transformed isoparametric element.

$$\begin{Bmatrix} \phi,\bar{\xi} \\ \phi,\bar{\eta} \end{Bmatrix} = [\bar{J}] \begin{Bmatrix} \phi,\xi \\ \phi,\eta \end{Bmatrix}$$

and inverted as

$$\begin{Bmatrix} \phi,\xi \\ \phi,\eta \end{Bmatrix} = [\bar{J}]^{-1} \begin{Bmatrix} \phi,\bar{\xi} \\ \phi,\bar{\eta} \end{Bmatrix}$$

where $[\bar{J}]$ is the Jacobian of transformation given as

$$[J] = \begin{bmatrix} \xi,\bar{\xi} & \xi,\bar{\eta} \\ \eta,\bar{\xi} & \eta,\bar{\eta} \end{bmatrix} = \begin{bmatrix} 1 & 0 \\ 0 & \frac{\Delta\bar{h}}{2} \end{bmatrix}$$

and

$$[J]^{-1} = \begin{bmatrix} \bar{\xi},\xi & \bar{\xi},\eta \\ \bar{\eta},\xi & \bar{\eta},\eta \end{bmatrix} = \frac{2}{\Delta\bar{h}} \begin{bmatrix} \frac{\Delta\bar{h}}{2} & 0 \\ 0 & 1 \end{bmatrix}$$

where $\Delta\bar{h}$ is defined as $\bar{h}_2 - \bar{h}_1$ and is given by

$$\Delta\bar{h} = \frac{2}{NRow - 1}$$

NROW = number of nodes chosen through the depth.

The transformed governing differential, Eqs. (4.7a) through (4.7c) in this new computational plane, take the following form

$$A_{KM}\,\phi,_{\bar{\xi}\bar{\xi}} + B_{KM}\phi,_{\bar{\eta}\bar{\eta}} + C_{KM}\phi,_{\bar{\xi}\bar{\eta}} + D_{KM}\phi,_{\bar{\eta}} = 0 \qquad (4.9)$$

$$\phi,_t + \tfrac{1}{2}A_{KM}\phi^2,_{\bar{\xi}} + \tfrac{1}{2}B_{KM}\phi^2,_{\bar{\eta}} + \tfrac{1}{2}C_{KM}\phi,_{\bar{\xi}}\phi,_{\bar{\eta}} + g(h - d) = 0 \qquad (4.10)$$

$$h_{,t} + A_{KM} h_{,\bar{\xi}} \phi_{,\bar{\xi}} + H_{KM} \phi_{,\bar{\eta}} h_{,\bar{\xi}} - G_{KM} \phi_{,\bar{\eta}} = 0 \qquad (4.11)$$

where the coefficients are

$$A_{KM} = \xi_{,x}^2$$

$$B_{KM} = (\eta_{,x}^2 + \eta_{,y}^2) Q^2$$

$$C_{KM} = 2\xi_{,x}\, \eta_{,x} Q$$

$$D_{KM} = \eta_{,xx} Q^2$$

$$G_{KM} = \eta_{,y} Q$$

and

$$H_{KM} = \eta_{,x}\, \xi_{,x} Q$$

$$Q = \bar{\eta}_{,\eta} = \frac{2}{\Delta \bar{\eta}}$$

As can be seen, the governing differential equations in the physical plane are transformed to variable coefficient differential equations in an isoparametric computational domain. The finite element formulation of the differential equations can be performed by evaluating the coefficients at the center of each element in terms of the global coordinates. These local elements can then be collected together to form a global system of differential equations.

4.3 Finite Element Solution Algorithm

As shown previously, the entire water domain is

decomposed into subdomains with isoparametric transformations. The governing differential equations are transformed to the parent computational domain. In order to derive the discrete form of this set of differential equations, we must employ a finite element approximation technique. In one approach, a functional is defined by some integral over the entire domain and its boundary, in which the unknowns and their derivatives appear. In this approach, the discrete equations are obtained by introducing the approximate solutions of unknowns in terms of a set of interpolation functions and the determination of the extreme values of integrals. Extension to the non-linear potential flow problem, like our present problem, using variational concepts appeared theoretically difficult without certain assumptions.

A second approach requires prior knowledge of the differential equations governing the problem. The finite element approximation can then be derived directly from the differential equation by the methods of weighted residual. The basic idea is to find an approximate solution by replacing the unknown variables with a set of functions in terms of nodal values and appropriate interpolation functions. The orthogonal projections of the residual with a set of weighting functions are then

constructed and set equal to zero, which is equivalent to forcing the error of the approximate differential equation to be zero in an average sense. Various techniques can be used such as the Galerkin method, least-squares method, and colocation method. It has been verified that a method of weighted residual for a linear equation produces a computational form that is identical to extremization of the equivalent variational principle. However, since no linearity constraint exists in the application of the weighted residual method, it may be used for a finite element solution of nonlinear equations.

In this section, the Galerkin finite element method is used for the discretization of governing differential equations. In the Galerkin method, the same shape functions which approximate the unknown variables are used as weighting functions.

Here, we employ a local finite element approach in which approximating functions are constructed in local elements; thus, avoiding the difficult task of requiring satisfaction of global boundary conditions.

To derive the element stiffness matrix corresponding to the conventional Galerkin weighted residual method, the same standard isoparametric shape functions of coordinate

transformations are used to approximate the flow potential field within the element in terms of potential function at nodes 1 to 4 (Fig. 4.4a)

$$\phi^{(e)} = \sum_{i=1}^{4} \bar{\Psi}_i^{(e)}(\bar{\xi},\bar{\eta})\ \phi_i^{(e)}(t) \qquad (4.12)$$

Here, for simplicity, we drop the summation symbol Σ and the symbolic (e) denoting local elements. Since the analysis will be performed in the parent computational domain with the coordinate $(\bar{\xi},\bar{\eta})$, we may also drop the bar symbol (-) from the equations for simplicity in carrying out the operations. Then the Galerkin finite element model of the transformed Laplace equation (Eq. (4.9)) takes the form

$$\int_{-1}^{1}\int_{-1}^{1} A_{KM}\phi_{,\xi\xi} + B_{KM}\phi_{,\eta\eta} + C_{KM}\phi_{,\xi\eta} + D_{KM}\phi_{,\eta}\, d\xi d\eta = 0$$

As was previously mentioned, the coefficients in the equation are evaluated at the center of the element, where K and M represent the column and row number of the right lower node of the element. To obtain a symmetric stiffness matrix, the terms $C_{KM}\phi_{,\xi\eta}$ can be written as

$$C_{KM}\phi_{,\xi\eta} = \frac{1}{2} C_{KM}\phi_{,\xi\eta} + \frac{1}{2} C_{KM}\phi_{,\eta\xi}$$

By substituting this term into the integral and performing integration by parts, we obtain

$$A_{KM}\int_{-1}^{1}\int_{-1}^{1}\phi_{,\xi}\Psi_{j,\xi}\, d\xi d\eta + B_{KM}\int_{-1}^{1}\int_{-1}^{1}\phi_{,\eta}\Psi_{j,\eta}\, d\xi d\eta + \frac{1}{2}C_{KM}\int_{-1}^{1}\int_{-1}^{1}\phi_{,\eta}\Psi_{j,\xi}\, d\xi d\eta$$

$$+ C_{KM} \int_{-1}^{1}\int_{-1}^{1} \phi_{,\xi} \Psi_{j,\eta} d\xi d\eta - D_{KM} \int_{-1}^{1}\int_{-1}^{1} \phi_{,\eta} \Psi_{j} d\xi d\eta \qquad (4.13)$$

$$+ \text{ Boundary Terms } = 0$$

We drop the boundary terms since they will be cancelled out in the global assembled stiffness matrix. By introducing Eq. (4.12) into (4.13), we obtain the local finite element equation

$$K_{ij} \cdot \phi_i = 0 \qquad (4.14)$$

where

$$K_{ij} = A_{KM} \int_{-1}^{1}\int_{-1}^{1} \Psi_{i,\xi} \Psi_{j,\xi} d\xi d\eta + B_{KM} \int_{-1}^{1}\int_{-1}^{1} \Psi_{i,\eta} \Psi_{j,\eta} \, d\xi d\eta +$$

$$\frac{1}{2} C_{KM} \int_{-1}^{1}\int_{-1}^{1} \Psi_{i,\eta} \Psi_{j,\xi} d\xi d\eta + \frac{1}{2} C_{KM} \int_{-1}^{1}\int_{-1}^{1} \Psi_{i,\xi} \Psi_{j,\eta} d\xi d\eta \qquad (4.15)$$

$$- D_{KM} \int_{-1}^{1}\int_{-1}^{1} \Psi_{i,\eta} \Psi_{j} d\xi \, d\eta$$

For a typical element, whose right lower node is numbered by column K and row M, the element stiffness matrix can be found by evaluating the integrals in the above expression. This matrix is defined in Appendix A-1.

To establish the global finite element equations, we should derive the globally assembled stiffness matrix. This can be obtained by summing the individual stiffness

matrices appropriately. A complete set of typical element combinations for the flow region, except for the free surface, is shown in Fig. 4.5. The equation for the common node for each assembly of elements is derived in Appendix A-2. Having the free surface height and distribution of the potential function over the free surface, all the equations for the nodes can be collected to form system of equations that define the values of at the nodal points through the flow field. In later sections, we develop a fast solution algorithms to solve a system of linear equations resulting from the finite element discretization of the governing equation.

4.4 Finite Element Solution Algorithm for the Free Surface Equations

A major difficulty that has hindered progress in long-term numerical computation of the equations of free surface motion has been the nonlinear computational instability of the numerical model of the governing differential equations. Since this nonlinear instability has its origin in space-truncation errors, we will be concerned here with the proper form of a finite element analog of the space derivatives.

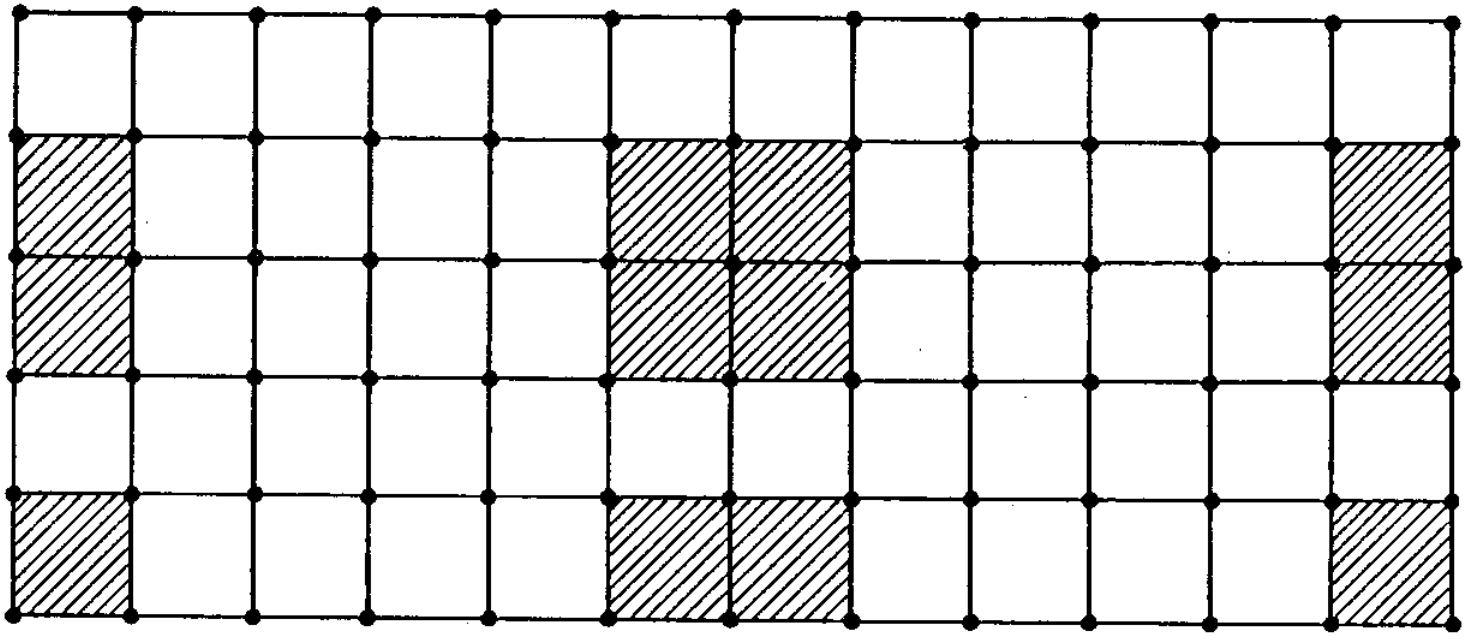

Fig. 4.5 Typical element combinations for the interior flow region.

Several investigators have undertaken the use of Galerkin techniques to solve this type of problem. These include Easton and Catton (1972) and Wellford and Ganaba (1981). In their work, only inviscid flows have been analyzed and potential functions formulation have been used. However, the inherent consistency of the Galerkin method in handling the nonlinearity of the free surface equations and matching of the equations in the fluid region is demonstrated in their work.

In our analysis, the approximate solutions of the free surface equations are sought using the Galerkin finite element method. Local models for the free surface displacement h and potential function ϕ are defined by standard isoparametric interpolation functions as

$$\phi = \psi_k(\xi, \eta)\phi_k \tag{4.26}$$

and

$$h = \beta_j(\xi)h_j \, . \tag{4.27}$$

For simplicity, we dropped the summation symbol Σ and the symbol (e) denoting a local element.

In the above approximations, K=1,...,4 and j=1,2, and ϕ_k and h_j are nodal values for potential function and

free surface height. The shape functions $\psi_i(\xi,\eta)$ are defined as before and

$$\beta_1(\xi) = \frac{1}{2}(1-\xi)$$

$$\beta_2(\xi) = \frac{1}{2}(1+\xi)$$

As a semidiscrete approximation for the dynamic free surface condition (Eq. (4.10)), the following Galerkin model is defined on a free surface element.

$$\int_{-1}^{1}\left\{\phi_{,t}+\frac{1}{2}A_{KM}\phi_{,\xi}^2+\frac{1}{2}B_{KM}\phi_{,\eta}^2+\frac{1}{2}C_{KM}\phi_{,\xi}\phi_{,\eta}+g(h-d)\right\}_{\eta=1}\beta_i d = 0 \quad (4.18)$$

A semidiscrete approximation for the kinematic free surface condition (Eq. (4.11)) is defined using a similar Galerkin model.

$$\int_{-1}^{1}\left\{h_{,t}+A_{KM}\,h_{,\xi}\phi_{,\xi}+H_{KM}\,\phi_{,\eta}h_{,\xi}-C_{KM}\,\phi_{,\eta}\right\}_{\eta=1}\beta_i\,d\xi = 0 \quad (4.19)$$

By introducing Eqs. (4.16) and (4.17) into (4.18) and (4.19), we obtain the local finite element equations for the free surface boundary as

$$M_{ij}\phi_{j,t} = N_{ij\iota}\phi_j\phi_\iota + P_{ij}h_j + Q_i \quad (4.20)$$

$$R_{ij}h_{j,t} = S_{ij\iota}h_j\phi_\iota + T_{ij}\phi_j \quad (4.21)$$

where $M_{ij} = \int_{-1}^{1}\left[\beta_i\,\psi_j\right]_{\eta=1}d\xi$

$$N_{ij\iota} = -\frac{1}{2}A_{KM}\int_{-1}^{1}\left[\beta_i\psi_{j,\xi}\psi_{\iota,\xi}\right]_{\eta=1}d\xi - \frac{1}{2}B_{KM}\int_{-1}^{1}\left[\beta_i\psi_{j,\eta}\right]_{\eta=1}d\xi$$

$$-\frac{1}{2}C_{KM}\int_{-1}^{1}\left[\beta_i\psi_{j,\xi}\psi_{\iota,\eta}\right]_{\eta=1}d\xi$$

$$P_{ij} = g\int_{-1}^{1} \beta_i \beta_j d\xi$$

$$Q_i = gd\int_{-1}^{1} \beta_i d\xi$$

$$R_{ij} = \int_{1}^{1} \beta_i \beta_j d\xi$$

$$S_{ij1} = -A_{KM}\int_{1}^{1} \left[\beta_i \beta_j, \xi \Psi_{1,\xi}\right]_{\eta=1} d\xi$$

$$- H_{KM}\int_{-1}^{1} \left[\beta_i \beta_j, \xi \Psi_{1,\eta}\right]_{\eta=1} d\xi$$

$$T_{ij} = G_{KM}\int_{1}^{1} \left[\beta_i \Psi_{j,\eta}\right]_{\eta=1} d\xi$$

Equations (4.20) and (4.21) represent approximate forms of the dynamic and kinematic free surface equations.

The global finite element model of the free surface can be obtained by proper assembling of the free surface elements. Figure 4.6 presents typical groups of assembled elements. The assembling of the elements is performed and the resulting equations are shown in Appendix A-3. The resulting equations are nonlinear and coupled in terms of the potential function ϕ and the free surface height h. These equations can be integrated in time at a discrete set of points, given a sufficient set of initial conditions. Integration of the free surface boundary equations through one time step leads to a new distribution of potential function over a new free

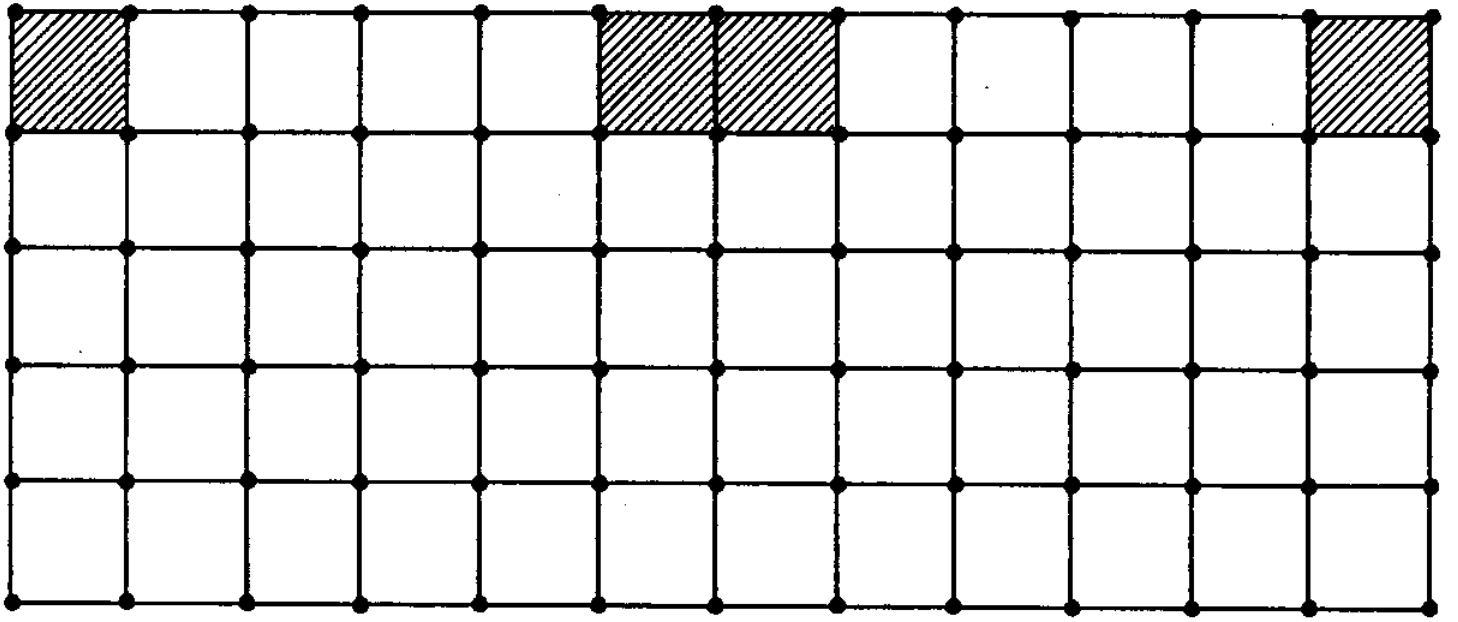

Fig. 4.6 Typical element combinations for the free surface.

surface h. The current values of ϕ and h can then be used to define the potential function through the flow region by solving a linear system of equations (Eq. (A-1)). Repeated applications of these computational steps in sequence gives a construction of the motion of the free surface as an initial value problem.

4.5 Numerical Integration of the Free Surface Equations in Time

In this section, we discuss the numerical integration of the time-dependent, free surface equations to advance ϕ and h in time, over the free surface boundary. The method of solution considered for our problem treats time-dependent, free surface boundary conditions as a set of coupled initial problems. A major difficulty in numerical integration of the free surface conditions is the nonlinear computational instability and the coupling of the free surface displacement and potential function. Approximation of derivatives by numerical methods introduces truncation errors. These errors are amplified by nonlinear terms and accumulate at large time, eventually degrading the accuracy of the solution. To overcome such difficulties, the proper choice of the integration method and the time step must be employed to

perform long computations.

The finite element discretization of the free surface boundary conditions lead to discrete equations (Eqs. (4.20) and (4.21)). The element matrices M_{ij} and R_{ij} are non-diagonal and can therefore be called consistent mass matrices (analog-to-mass matrices resulting from dynamic analysis of structural problems). The consistent mass (non-diagonal) matrices introduce coupling between the time rate-of-change of ϕ and h at adjacent nodes which essentially demand the use of implicit methods. It should be realized that the coupling between the time derivatives of the nodal values of ϕ and h resulting from finite element discretization is different from the inherent coupling between the dynamic and kinematic free surface conditions. In dynamic analysis of structural problems, the relative speed and simplicity of explicity methods has lead to the concept of mass lumping. Mass lumping eliminates any coupling between the time derivative of unknowns at adjacent nodes and converts the mass matrix to a diagonal form. The accuracy of the lumping technique usually depends on the number of nodes used to describe the element. In some problems, this approximation reduces the computer storage and computational steps with only a small loss of

accuracy. Gresho et al. (1978) employed mass lumping of the time derivative terms in applying the Galerkin finite element to the advection-diffusion equation in an incompressible flow field. Reasonably good success has been reported in their work.

In our work, we employ a mass lumping technique in which the procedure of lumping can be performed by summing the rows of consistent mass matrix and placing the results on the diagonal in the element mass matrix. In terms of global discrete equations (Eq. (A-2)), the mass lumping can be invoked by summing the coefficient of the coupled time-derivative terms and placing the results as the coefficient of the time-derivative term at the computational node. For instance, the left-hand side of Eqs. (A-2e) and (A-2f) can be written as

$$\frac{2}{3}\phi_{,t}(K-2,M)+\frac{8}{3}\phi_{,t}(K-1,M)+\frac{2}{3}\phi_{,t}(K,M) \equiv 4\phi_{,t}(K-1,M) \qquad (4.22)$$

$$\frac{1}{3}h_{,t}(K-2,M)+\frac{4}{3}h_{,t}(K-1,M)+\frac{1}{3}h_{,t}(K,M) \equiv 2h_{,t}(K-1,M) \qquad (4.23)$$

We were primarily interested in finite element approximation of spatial derivatives, and we applied a semidiscrete finite element method in which the independent variable t is not included in the shape functions, and in which the time derivatives of the

variables at nodes are replaced by a finite difference operator. Thus, a proper finite difference scheme must be employed to avoid instability and inaccuracy in final results.

Generally, the different schemes are classified as explicit and implicit. In explicit methods, the solution of an unknown at the new time step $(n+1)\Delta t$ is based on using the information at the old time step $n\Delta t$. Considering the following differential equation

$$u_{,t} = F(u,t)$$

The time derivative can be replaced by finite differences of various forms, such as,

$$u^{n+1} = u^{n} + \Delta t F^{n} \qquad \text{(Forward difference)}$$

where the superscripts refer to the time step. Using a stability analysis, it can be shown that explicit integration schemes require the use of a time step Δt smaller than a critical time step. thus, explicit techniques are said to be conditionally stable. If a time step larger than the critical time step is used, then any errors resulting from the numerical integration or round-off error calculation of spatial domain accumulate and grow, resulting in inaccuracy of the final results. Another class of integration schemes which are

unconditionally stable are called implicit schemes. The important role of unconditionally stable integration is derived from the fact that there is no restriction on selecting the time step Δt to obtain accuracy in integration. In some cases, time step for implicit method can be selected at orders of magnitude larger than the critical time step in the explicit method. The only restriction on Δt for implicit representation is to keep the truncation error at the reasonable level. In the implicit method, the calculation of a new time increment of an unknown requires knowledge of the previous time step and the current time step; for example,

$$u^{n+1} = u^{n} + F^{n+1}$$

In this case, the function F(u,t) must be evaluated at the new time step. Then one must solve a set of simultaneous equations to obtain u^{n+1}. Although the implicit equation has the advantage of accuracy and of permitting the use of larger time step, it is no longer possible to solve the resulting system of equations in a simple manner in two-dimensional cases. One of the methods usually employed in using implicit scheme is the alternating-direction-implicit or ADI method. In this method, calculations are simplified by preserving the stability of the algorithm. The finite difference

equations are reformulated so that the resulting algebraic problem consists of a set of linear equations with a tridiagonal matrix in each coordinate direction. Then, each time step Δt is divided into halves, and each half-step is used to solve the equation in each coordinate direction. The two successive time step constitute a cycle of the calculation. Fairweather and Navon (1980) proposed a new ADI method for the approximate solution of the shallow-water equations.

In the solution of the coupled nonlinear partial differential equations, as in the present problem, implicit methods result in nonlinear algebraic equations in terms of the free surface height h and velocity potential ϕ which are coupled through the free surface equations. Then, the solution to this set of nonlinear algebraic equations requires extensive matrix manipulations which may become very inefficient and costly.

Explicit methods can be classified by the order of accuracy of schemes. This can be shown by the development of the Taylor series for U about (t,x), which gives

$$U(t+\Delta t,x) = U + \Delta t U_{,t} + \frac{(\Delta t)^2}{2!} U_{,tt} + 0\left[(\Delta t)^3\right] \quad (4.24)$$

In a method of m^{th}-order of accuracy, the Taylor series for the finite difference equation is identical to the above expansion up to and including the term multiplied by the m^{th} power of the time increment. Euler-explicit or the forward difference is simply the first-order approximation

$$U_{,t} = \frac{1}{\Delta t}\left[U^{n+1} - U^{n}\right] + 0\left[\Delta t\right]$$

where $0(\Delta t)$ represents the asymptotic notation for the truncation error of this approximates. An example of a second-order approximation is the central difference or leap-frog which can be found by substracting the Taylor series for $u(t-\Delta t,x)$ and $u(t+\Delta t,x)$. Another example of second-oder approximation is the Lax-Wendroff time integration scheme which can be obtained by retaining up to the second-order terms in expansion (Eq. (4.24). In this case, the computation of the values of u_{tt} requires a lot of computational time.

An integration with second-order accuracy does not mean that its application will always result in a more accurate technique than other first-order techniques. Test calculation on several nonlinear problems reported by Richtmyer and Mortor (1967) showed that the use of the leap-frog scheme yielded solutions which exploded

exponentially, while for the corresponding linearized problem the scheme showed stable or slightly unstable behavior. They also showed that the leap-frog scheme, even in the linearized case, is marginally stable. Easton and cotton (1972) surveyed and used six integration techniques for solving the nonlinear, transient motion of a liquid with a free surface. The stability and performance of integration schemes were checked by monitoring the total energy of the system.

In the present study, we simulate the time derivatives by the forward difference scheme which is the most commonly used technique in explicit integration of nonlinear fluid dynamic equations.

To define our integration model, we first rewrite the discrete free surface equations in a simpler form. Using relations (4.22) and (4.23), Eqs. (A.2e) and (A.2f) can be written as,

$$4\phi_{,t}(K-1,M) = F_1(\phi,h)$$

$$2h_{,t}(K-1,M) = F_2(\phi,h)$$

where $F_1(\phi,h)$ and $F_2(\phi,h)$ represent the right hand sides of Eqs. (A.2e) and (A.2f).

The time integration of the above equations can be obtained by using a forward difference procedure which

assumes linear variations of potential functions ϕ and free surface height h over the time step Δt. Thus, the above equations may be replaced by the following algorithm

$$\frac{4}{\Delta t}\left[\phi^{n+1}(K-1,M) - \phi^{n}(K-1,M)\right] = F_1^n(\phi,h)$$

and

$$\frac{2}{\Delta t}\left[h^{n+1}(K-1,M) - h^{n}(K-1,M)\right] = F_2^n(\phi,h)$$

where the value of n is increasing from 0 to the desired location in the t coordinate. The above relations can be rearranged as,

$$\phi^{n+1}(K-1,M) = \phi^{n}(K-1,M) + \frac{\Delta t}{4} F_1^n(\phi,h) \qquad (4.25)$$

$$h^{n+1}(K-1,M) = h^{n}(K-1,M) + \frac{\Delta t}{2} F_2^n(\phi,h) \qquad (4.26)$$

Since the right-hand sides of the above equations are known at the start of the time interval $(t,t+\Delta t)$, Eqs. (4.25) and (4.26) can therefore be solved directly for the nodal values of ϕ and h at the end of the time interval.

As was previously discussed, explicit schemes require that the time step chosen be smaller than some critical Δt determined in terms of the size of the other increments for stability condition to prevent the accumulation of truncation errors and round-off errors. In practice, if

this condition is not met, the symptoms of instability show up in a small number of cycles. For linear and constant coefficient differential equations, stability can be determined by using Fourier method or matrix method. But for nonlinear cases neither of these methods can be used directly to study the stability without a prior linearization. Courant, Friedrichs, and Lewy (1928) used a finite difference approximation to linear wave equations. Their stability condition which is called CFL or Courant condition states that numerical wave speed $x/\Delta t$ must be greater than the propagation speed. Violation of the Courant condition results in numerical oscillations and exponentially growing instability in the solution. This condition can also be used for nonlinear propagating problem such that

$$\Delta t < \frac{\Delta x}{NC} \tag{4.27}$$

where c is the propagation speed and N is an integer number.

For a nondissipative problem, such as the present one, the computational stability is more critical than is the dissipative problem, since the viscosity itself will damp out some of the numerical oscillations. The integration schemes with the first-order accuracy are

usually inadequate if a discontinuity or an abnormal oscillation exist in the solution.

4.6 Convergence and Accuracy

The accuracy and stability of the scheme is tested by numerical experiments. A measure of the accuracy of a numerical scheme is the accuracy with which quantities that are conserved analytically are also conserved numerically. In the present numerical model, since the effects of viscosity and air entrainment are not included, these conserved quantities are the volume and total energy of the system.

The total energy of wave system consists of the potential and kinetic energy components. To evaluate the potential energy of a progressive wave per unit width, we choose the horizontal bottom as datum and consider a small column of water h high, and Δx long (Fig. 4.7a). Then the potential energy can be expressed as,

$$\Delta(P.E.) = \frac{1}{2}\gamma\left[\frac{h_{m-1} + h_m}{2}\right]^2 \Delta x$$

Then,

$$(P.E.) = \sum_{m=1}^{NCOL} \frac{1}{8}\gamma(h_{m-1} + h_m)^2 \Delta x$$

The kinetic energy of a small element Δx long, h

high, (Fig. 4.7b) and of unit width and velocity components u, v, is given by

$$\Delta(K.E.) = \frac{1}{2}\frac{\gamma}{g}(U_m^2 + v_m^2)\,\Delta h_m\,\Delta x$$

or

$$\Delta(K.E.) = \frac{1}{2}\frac{\gamma}{g}(U_m^2 + v_m^2)\left[\frac{h_{m-1} + h_m}{2(NRow-1)}\right]\Delta x$$

Thus,

$$\Delta(K.E.) = \frac{1}{4}\frac{\gamma}{g}\sum_{m=1}^{NCOL}(U_m^2 + v_m^2)\left[\frac{h_{m-1} + h_m}{NRow - 1}\right]\Delta x$$

where γ is the specific weight of water.

The numerical experiments involve first setting up the initial conditions for a solitary wave with height H and some specified wave length. Then, the shape of the wave for some propagation period is examined, and the ratios of initial-to-final volumes and initial-to-final energies are calculated. The time step is reduced using the CFL conditions until there is no oscillation in the wave shape and the ratios of volumes and energies have a high degree of accuracy.

For numerical purposes, the amplitude of a solitary wave is assumed to be zero where the ratio of wave height to maximum amplitude is less than 0.01. Considering the Boussinesq solitary wave profile

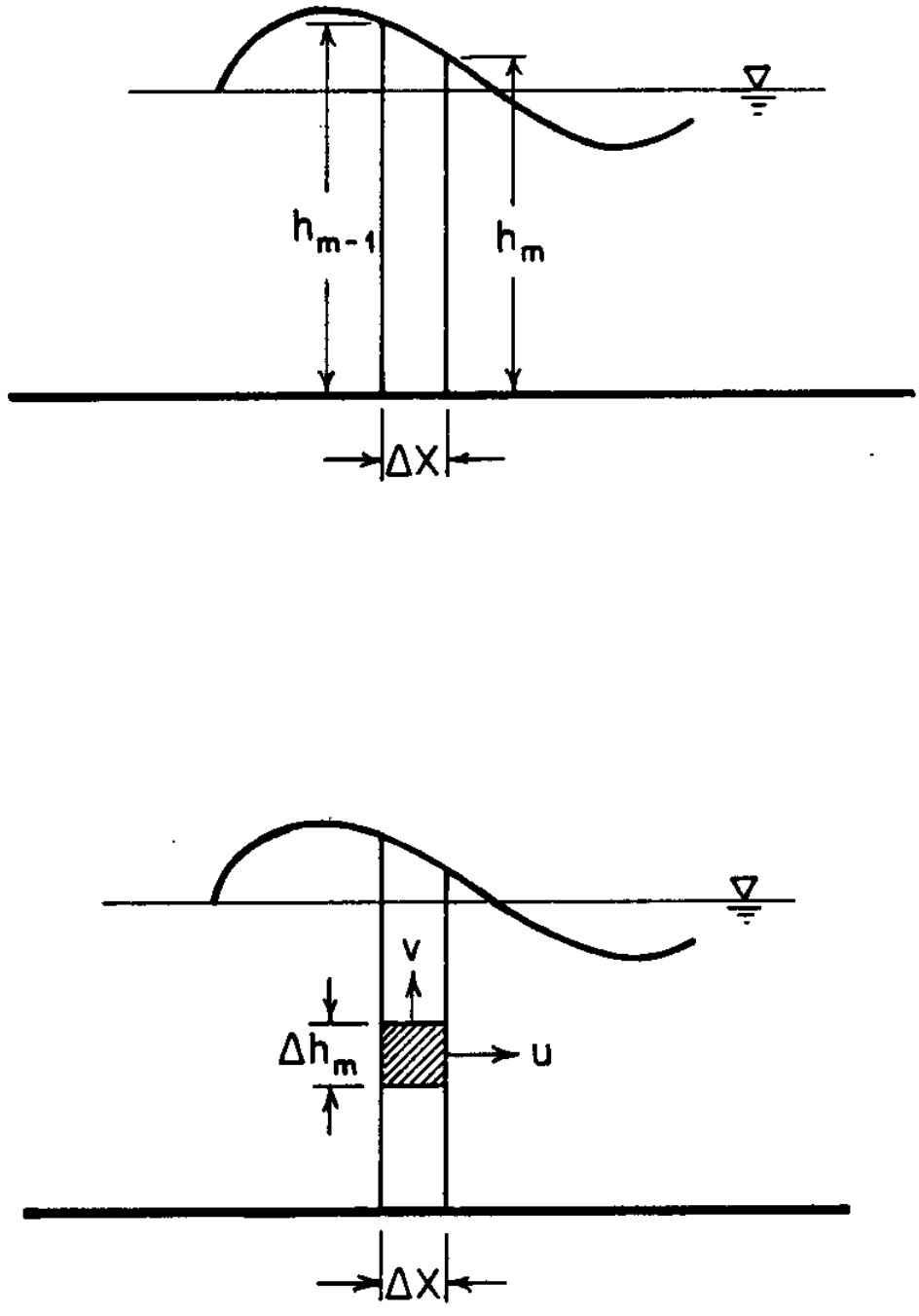

Fig. 4.7 Definition sketch for kinetic and potential energy.

$$\eta(x,t) = H\,\mathrm{Seh}^2\sqrt{\frac{3}{4}\frac{H}{d^3}}\,(x-ct) \qquad (4.28)$$

where

$$C = \sqrt{g(d+H)}$$

The finite length of the wave can be defined as,

$$L = \frac{5.98}{K}$$

where

$$K = \sqrt{\frac{3}{4}\frac{H}{d^3}}$$

To advance the free surface location and velocity potential in time, we should define the initial free surface profile as well as the initial velocity potential distribution over the free surface boundary. The velocity potential over the free surface can be derived by integration of horizontal or vertical velocity components.

The wave profile (Eq. (4.28)) can be written as

$$\eta = H\,\mathrm{Seh}^2\,\frac{\alpha}{d}\,(x-ct)$$

where

$$\alpha = \sqrt{\frac{3}{4}\frac{H}{d}} \qquad (4.29)$$

In shallow water to the first-order approximation, the horizontal water particle velocity can be expressed as,

$$U = \frac{\eta}{d}\,c \qquad (4.30)$$

While the vertical velocity v is approximately $\partial\eta/\partial t$.

Hence, by using the velocity potential definition and the above approximations, the expression for the velocity potential over the free surface can be obtained as,

$$\phi = \frac{cH}{\alpha} \tanh \frac{\alpha x}{d}$$

The nodal spacing can be found by selecting the number of nodes, Nx, over which the wave is described. This can be shown as,

$$\Delta x = \frac{L}{Nx}$$

The time step Δt can be determined from Eq. (4.23) as,

$$\Delta t = \frac{\Delta x}{N \sqrt{g(H+d)}} \qquad (4.31)$$

where N is an integer number which should be determined from the numerical experiments.

In Chapter 6, the numerical stability of the wave system is tested by numerical experiments. A test program is chosen to present propagation of a solitary wave for different time increments (different CFL numbers). The optimum Δt is obtained by using the relation (4.31) and reducing Δt until the result of the numerical experiment does not change significantly.

As noted in Chapter 6, the convergence and numerical stability of the numerical model is obtained only for small value of time increment Δt. This implies that a substantial computational work is required for propagation of a solitary wave for large times, since each time step involves the solution of the algebraic system of equations resulting from the global form of Eq. (4.14). The computational time can be reduced by developing a fast-solver algorithm for the present model.

In Section 4.8, we will discuss different methods for solution of an algebraic system of equations resulting from finite element discretization and will develop a multi-grid algorithm for the present model.

4.7 Artificial Viscosity Effects

As indicated in Chapter 6, the sequence of wave impact on a horizontal platform is studied and described by the numerical model. An initial solitary wave of height H propagates through the still-water depth d, and reaches the horizontal platform mounted a distance, s, above the still water level. The undisturbed wave front, where water first wets the platform, propagates beneath the platform, while the high vertical front face of the platform causes a jet of fluid to shoot upward. As the

wave advances further, the height of run-up created by the platform has grown wider, and reflected wave train can be formed at the front edge of the platform. This discontinuity in the free surface profile causes a severe oscillation at the front face of the platform for the larger time.

As previously mentioned, in non-dissipative, nonlinear problems, any symptom of discontinuity in the solution may be amplified by nonlinear terms and may accumulate at large time, eventually degrading the accuracy of the solution. The oscillation in regions of rapid change, such as the front face of the platform, could be related to the nonlinearities or the rapid variation of the coefficients.

Several investigators have studied similar problems for treatment of shock waves in gas dynamics and interfaces separating two different fluid. Von Neumann and Richmyer (1950) discussed an approximate method of calculation for fluid dynamic problems in which a dissipative mechanism like viscosity or heat conduction is introduced into the governing equations to smooth the shock transition. In this method, the surface of discontinuity is replaced by a thin transition layer in

which quantities change rapidly, but not discontinuously. According to Richmyer (1967), the problem of flow between a detached shock and a rectangular body was investigated by Berstein. In this problem, there are two regions of very rapid change - the shock layer and the neighborhood of the corner of the body, where the flow changes rapidly from subsonic to supersonic. The calculation is found to be unstable in both regions unless a viscosity term is included in the equations. The Lax-Wendroff treatment of shock waves (1960) was based on the idea of constructing a difference scheme as a means of containing the effect of viscosity. They developed and used difference schemes for systems of conservation laws by including an additional quadratic operator in the equations. Hafez et al. (1978) studied the effect of artificial viscosity to smooth out a shock wave, by employing a Galerkin finite element procedure to the transonic equation with an additional artificial viscosity term.

In accordance with the form of the free surface equation, we may include an artificial viscosity term $\nu h_{,xx}$ in the kinematic free surface equation, i.e.,

$$h_{,t} + \phi_{,x} h_{,x} - \phi_{,y} - \nu h_{,xx} = 0$$

where ν is a positive artificial viscosity parameter. For

relatively small ν, the viscous term will be effective only where $|h_{,xx}|$ is large. It should be pointed out that the artificial viscosity term does not represent any loss of energy or other conserved quantities. Thus, the presence of the artificial viscosity term does not alter the stability of the usual algorithm for smooth fluid flow.

The above equations can be expressed in terms of parent computational coordinates as,

$$h_{,t} + A_{KM}h_{,\xi}\phi_{,\xi} + H_{KM}\phi_{,\eta}h_{,\xi} - G_{KM}\phi_{,\eta} - E_{KM}h_{,\xi\xi} = 0$$

where

$$E_{KM} = \nu\xi_{,x}^2$$

and A_{KM}, H_{KM}, and G_{KM} are defined as before.

Employing the same procedure as was used to develop Eq. (4.19), the following Galerkin model is defined as,

$$\int_{-1}^{1}\{h_{,t}+A_{KM}h_{,\xi}\phi_{,\xi} + H_{KM}\phi_{,\eta}h_{,\xi}-G_{KM}-E_{KM}h_{,\xi\xi}\}_{n=1}\beta_i d\xi = =$$

After integration by parts, we get

$$\int_{-1}^{1}\{h_{,t} + A_{KM}h_{,\xi}\phi_{,\xi}+H_{KM}\phi_{,\eta}h_{,\xi} - G_{KM}\phi_{,\eta}\}_{\eta=1}\beta_i d\xi+\int_{-1}^{1}E_{KM}h_{,\xi}\beta_{i,\xi}d\xi+B.T. = 0$$

We simply drop the boundary terms, since they will be cancelled out in the global form of the free surface equations. By introducing Eqs. (4.16) and (4.17) into the above equations, we obtain the local finite element equation for the kinematic boundary condition with the

artificial viscosity included.

$$R_{ij}h_{j,t} = S_{ij\iota}h_j\phi_\iota + T_{ij}\phi_j + Z_{ij}\cdot h_j$$

where

$$Z_{ij} = -E_{KM}\int_{-1}^{1}\beta_{i,\xi}\beta_{j,\xi}\,d\xi$$

Employing the same procedure as was used for Eq. (4.21), the assembling, mass-lumping, and explicit temporal discretization for the artificial viscosity analogue of the free surface equation can be obtained.

The numerical value of the artificial viscosity parameter is determined by numerical experiments. In Chapter 6, the numerical results for the free surface profile with and without the artificial viscosity term are presented and discussed in detail.

4.8 Solution Methods for Discrete Equations

The finite element discretization procedures result in a system of linear of nonlinear algebraic equations which must be solved by numerical techniques. Linear equations are solved either by direct or iterative methods to obtain solutions to the system of linear equations resulting from the finite element discretization. Nonlinear problems are analyzed by iterative methods, or sequences of direct or iterative procedures. Even in solving nonlinear systems of equations, we can often

approximate the nonlinear system with a sequence of linear equations, as in Newton's method. Solving a linear system of equations can be generally categorized either by the direct method which yields solutions in a finite and predictable numbers of operations, or by the indirect or iterative techniques that start from a first approximate solution and become more accurate when the number of iterations increases until a sufficient accurate solution is obtained. Iterative methods are preferred for large sparse systems of equations where direct methods are suitable for quite large sets of equations having handed coefficient matrices. Both solution schemes has certain advantages and disadvantages.

The most effective direct solution algorithms used are applications of Gaussian elimination procedures for solving systems of algebraic equations. However, the effectiveness in finite element analysis depends on the properties of the finite element stiffness matrices. These techniques have proved to be particularly effective when the stiffness matrices resulting from finite element discretizations are symmetric and positive definite, and when bandwidths are small compared to the total number of equations.

In using direct methods for solving a system of linear equations resulting from finite element discretizations, the active column solution, or the skyline reduction method can be used to improve the efficiency of the direct Gaussian elimination procedures. It is an advantage of the finite element analysis that the resulting stiffness matrices are not only symmetric and positive definite but also handed. In active column solution algorithm, no operations are performed on zero elements outside the skyline. Another direct method used in solving a system of linear equations resulting from finite element discretization is known as Choleski's method. It is only suitable for the solution of positive definite systems for which all diagonal elements are positive. In Choleski's method, there is a factorization that can be carried out without any need for pivoting or scaling, which decomposes the coefficient matrix into a lower triangular matrix that can be related to a symmetric version of Gaussian elimination.

The wave front or frontal method is also an implementation of Gaussian elimination in which instead of assembling the complete stiffness matrix, it combines the assembly and elimination phases of the analysis before the entire set of the coefficient matrix is formed. In a

frontal algorithm, the efficiency of the method depends on the effectiveness of bookkeeping and not on the algorithm. It has the disadvantage of requiring high computer storage necessary for large systems.

In structural models, substructuring techniques such as static condensation procedures are used to reduce the order of the system matrices by the elimination of internal variables within the substructures, and the assembling of the substructural models containing only the variables on the boundaries of substructures to define the final system of equations. In condensing out the internal variables within the substructure, part of the total Gaussian solution is carried out.

For linear systems that are too large to solve by the direct method because of the storage required, the iterative technique is often the only possible method of solution. It is also an effective scheme in problems where a model is reanalyzed with slight changes (e.g., time-dependent problems). Then the previously obtained solution is a good starting approximation for the solution of new systems of equations. Another advantage of iterative method is that there is a no need to form the complete stiffness matrix because the iteration sweep can

be carried out over the element level. Iterative methods have been found to be suitable schemes for solving systems of equations resulting from finite difference and finite element discretizations of fluid mechanics problems.

There are basically two classical iteration methods - Gauss-Jacobi and Gauss-Siedel methods - that are applicable in finite element analysis. In the Gauss-Siedel method, unlike the Gauss-Jacobi, as each new value of an unknown is computed it replaces the old value. In iterative methods, only one computer storage location is required for each unknown, and the iteration is stopped when a convergence criterion (for certain error tolerance) is satisfied. The number of iterations depends on the accuracy of the starting approximation and on the condition number of the stiffness matrix. Convergence of iterative methods does not depend on the initial guess for starting approximations; it depends on the character of the equations.

To improve the convergence rate of the fundamental iterative methods, various schemes have been employed since most iterative methods have a regular pattern in which the error decreases. The relaxation is usually used to accelerate the convergence. In this method, a

relaxation parameter ω is introduced to modify the value of each unknown, by Gauss-Siedel iteration, before the value is stored for the next iteration. The calculation of ω is difficult except in simple cases, and it is usually obtained by trial and error. In the successive-over-relaxation (SOR) technique, the value of ω is chosen greater than one but less than two and it is usually employed to accelerate an already convergent iterative algorithms.

Similarly, other methods such as the line relaxation procedure and the alternating direction implicit technique have frequently been used in finite difference discretizations, but they have not been employed in finite element analysis, in particular, because of irregular meshes characteristic. This is because the line relaxation and ADI methods are usually used in simple geometrical mesh patterns.

Recently, another method called the multi-grid method has been proposed to accelerate the convergence rate of the basic iterative algorithm by using coarser grids on the same domain of the problem to eliminate the low frequency of the errors, and relaxing on finer grids to smooth high-frequency errors. In this method, the overall

error of the iterative scheme is reduced at a rapid rate. This method has gained a great attention in finite difference discretization of differential equations.

Later in this section, we will discuss the basic idea of the multi-grid method and construct an efficient multi-grid algorithm for our problem. To investigative the convergence properties of the multi-grid method, the basic Gauss-Seidel and SOR methods are also discussed for the purpose of comparison.

4.8.1 Successive-Over-Relaxation Method

The successive-over-relation (SOR) method basically consists of a single modification of Gauss-Seidel's method by introducing a relaxation parameter in operational equations. For example, we consider the system of linear equations

$$Ax = B$$

The point relaxation operational equation can be defined as

$$x_i^{(K+1)} = x_i^{(K)} + \omega R_i^{(K+1)}$$

where the residual, R, is defined by

$$R_i^{(K+1)} = x_i^{(K+1)^*} - x_i^K$$

where (K+1) is the current iteration and (K) is the

preceding iteration, the quantity $x^{(K+1)^*}$ is the current approximate solution obtained by Gauss-Seidel iteration, and ω is an arbitrary parameter in the range $1<\omega<2$ for SOR method. The optimum value of ω should be chosen such that the convergence rate is maximized. The optimum relaxation parameter is usually found by trial and error for a particular problem. For $\omega=1$, the method obviously reduces to Gauss-Seidel's method.

The successive relation method was discussed and used by Lomex and Steger (1975), Fix and Larsen (1971) to solve linear systems of equations arising from elliptic boundary-value problems. Fix and Larsen (1971) stated that if , the relaxation parameter has its optimum value for a particular problem, SOR iteration for finite-element systems converged like the SOR iteration for finite-difference equations.

In the present problem, the value of optimum ω is found by a series of numerical experiments in the test problems. Then the convergence rate of the scheme will be compared with multi-grid method.

4.8.2 Multi-Grid Method

The idea of the multi-grid is to employ not only a

fine grid for the domain of the domain but a sequence of coarser grids. This method employs periodic interruption of the iterative solution on a fine grid to eliminate the low-frequency error by solution of residual equations on coarser grids, to speed the convergence of the relaxation scheme which involve the final solution of unknowns on the finest grids. The multi-grid method is particularly effective for second-order elliptic equations, since the error reduction for this class of problem is proportional to the number of grid points.

The solution of the large systems of equations, arising from finite element discretization, is actually an approximations to the exact solution of the governing partial differential equation. Then, the system of equations can itself be approximated by a smaller system of equations defined on coarser grids. This numerical algorithm can be carried out for an algebraic system of equations resulting from the application of finite element discretizations with Drichlet and Neumann boundary conditions, with no restrictions on shape functions normally required by the finite element methods. Acceleration techniques using multi-grid methods were introduced by several investigators, including Sattari and Aziz (1973), who generalized additive correction methods

for the iterative solution of matrix equations resulting from finite difference discretizations of elliptic and parabolic partial differential equations; by Wachspress (1977), who described a two-level acceleration techniques using variational methods; by Nicolaides (1975, 1977) who proposed a convergent algorithm using multiple-grid techniques for solving elliptic equations; and by Brandt (1977) who developed and used a multi-level technique for the solution of algebraic equations resulting from discretization of boundary value problems.

The technique used in our work is of multi-grid type that was introduced by Brandt (1977) and used for the finite difference cases. We will demonstrate the workability of the multi-grid scheme in solving a linear system of algebraic equations resulting form finite element discretization. We will compare the convergence rate of this method with other methods, such as, SOR.

To illustrate the multi-grid idea, we consider the following boundary value problem

$$LU(x) = G(x) \quad \text{in } \Omega$$

$$\Lambda U(x) = H(x) \quad \text{on the boundary } \partial\Omega$$

where L and Λ are linear differential operators in the domain Ω and on the boundary $\partial\Omega$.

Let the entire domain Ω be divided into K nonoverlapping subdomains, with corresponding mesh size D_K. Then for different grid size D_K, we have a set of grids Ω_K approximating the domain. Let Ω_K be a grid and with $D_{K-1} > D_K$, so that Ω_K is a subgrid of Ω_{K-1}.

Finite element approximation of the differential equation leads to a system of discrete equations of the form,

$$AU = F \tag{4.32}$$

where A is the coefficient matrix or stiffness matrix and F is the right-hand side vector.

In our physical problem, we are interested in the solution of this discrete system of equations on the finest grid Ω_N. The objective of the multi-grid technique is the elimination of low-frequency error components by the use of coarser grid operations, which involves solution of much smaller algebraic equations and then interpolating the solution from the coarser grid to a fine grid to smooth out high-frequency error components. To construct the most efficient algorithm, the said suggestion can be modified for different problems, but the

main concept is a valid one.

Let u^K be an approximate solution to the problem on any grid Ω_K found by the relaxation method. Then the residuals can be defined as

$$r^K = A^K u^K - F^K \tag{4.33}$$

The residual functions can be used to find the correction v^K which satisfies the residual equations

$$A^K v^K = r^K \tag{4.34}$$

then the exact discrete solution is

$$U^K = u^K + v^K \tag{4.35}$$

Now, if we could solve Eq. (4.34) with some inexpensive operations, then the correction obtained can be interpolated to a good approximation to solve Eq. (4.32).

To carry out the solution of residual equations, coarser grids are used with projection of residuals from fine grids to coarser grids. The projection of residuals will result in a meaningful approximation on coarser grids if the residuals are not rapidly fluctuating on the fine grid. This can be done by relaxation sweep on the fine grid to smooth out the high-frequency error since as long

as the relaxation on the fine grid exhibits fast convergence the residuals are not smoothed out, and as soon as the residuals are smoothed out, the convergence rate decreases.

The criteria for slow convergence rates may be determined by error analysis. Consider

$$A^K U^K = F^K$$

Suppose there exist a diagonal matrix N and a matrix M such that

$$N^K U^K = F^K + M^K U^K \tag{4.36}$$

then, the operational equations for the relaxation sweep can be defined as

$$N^K U^K_{(m+1)} = F^K + M^K u^K_{(m)} \tag{4.37}$$

then the error is found by substracting Eq. (4.37) from Eq. (4.36) as

$$N^K e^K_{(m+1)} = M^K e^K_{(m)}$$

or

$$e^K_{(m+1)} = E^K e^K_{(m)}$$

where

$$E^K = (N^K)^{-1} M^K$$

The rate of convergence of Eq. (4.36) depends on the eigenvalues and eigenvectors of E . But, practically, the behavior of the error is simple for algebraic equations resulting from elliptic equations, and usually after a few relaxation sweeps, the size of any error norm decreases by approximately a constant factor at each step. The slow convergence criterion is independent of mesh size and may be found by trial and error on a coarse grid (Brandt 1977).

In the current study, the slow convergence criterion, C, is determined by numerical experiments. Then, a switch to a coarse grid is made if

$$\frac{\left\| U^{K}_{(m+1)} - U^{K}_{(m)} \right\|}{\left\| U^{K}_{(m)} - U_{(m+1)} \right\|} \geq C \qquad (4.38)$$

where the norm used is a L_2 norm.

For solving algebraic system of equations resulting from elliptic equations with variable coefficients, the value of C varies over the computational domain since L_2 norm of the error varies for each node. Then, to make sure that all the high frequency of error components are smoothed out, the largest value of C should be used.

Several numerical experiments were performed to find the approximate value of C. This was done by using a

series of trial values for C. Then the effectiveness of the coarse grid corrections were examined by checking the performance of the fine-grid algorithm. It was found that the overall efficiency of the algorithm was not very sensitive to a range of values near the optimal C.

As was previously discussed, the residual equations are fully solved on the coarse grid, and the solution of the coarse grid problem is then used to update the related fine-grid iterate solution by an additive correction scheme. This is done to eliminate the low-frequency of the error components. To increase the efficiency of the algorithm, we should detect when these low-frequency errors are eliminated, and stop the iteration on the coarse grid when some convergence criterion is met.

A crude node analysis by Brandt (1977) showed that iteration on coarse grid can be stopped when the following convergence criterion is met.

$$\left\| u^{K}_{(m+1)} - u^{K}_{(m)} \right\| \leq \gamma \left\| u^{K+1}_{(m+1)} - u^{K+1}_{(m)} \right\| \qquad (4.39)$$

where these norms are comparable norms, such as L_2, L_∞, and the constant γ can be found by trial and error and is independent of the mesh size. To find the optimum value of γ, several trial values of γ are used in the numerical

experiment to detect the situation at which more improvement is obtained by relaxation on the fine grid.

Efficiency of the algorithm was examined for different values of γ. It was found that the efficiency is not very sensitive to values in a range of optimum γ.

The interaction between different levels in multi-grid method involves projecting residuals from a fine grid to next coarser grid and transferring corrections from a coarse grid to the next finer grid. For algebraic systems of equations resulting from finite difference discretizations, the interpolation used should involve proper weights that do not convert small low-frequency errors into large high-frequency errors. Brandt (1977) stated that the order of interpolations from a coarse grid to a fine grid, I_{K-1}^{K}, should not be less than the order of the differential equations and the polynomial interpolation should be made with polynomials of degree > n-1, where n is the degree of differential equation. Otherwise, even a small and smooth residual may produce large high-frequency residuals which involve more computational work to smooth them out. This effect was supported by numerical experiments.

For a system of equations arising from finite element discretizations, the interpolation of corrections from a coarse grid to a fine grid is a simple transfer of identical nodal values, since interpolation procedures follow automatically from the variational formulation and the fact that grid Ω_K is a subspace of Ω_{K-1}.

The interpolation of residuals from a fine grid to the next coarser grid can be performed by some weighted average of the residuals in neighboring nodes on a fine grid identical to the next coarser grid nodes. That is,

$$r^{K-1} = I_K^{K-1}(r^K - A^K u^K)$$

In our work the trivial weighting is used because it requires the computation of residuals r^K only at the coarser grid Ω_{K-1} points, But, nontrivial weighting requires computation of the residuals at all Ω_K points which increases the computational time.

Numerical experiments were also performed for nontrivial weighting interpolations but no improvement was obtained.

4.8.3 Multi-Grid Algorithm and Iterative Procedure

In this section, steps taken in carrying out the

multi-grid procedure are defined and a typical flowchart is presented in Fig. 4.8.

The algorithm is superficially similar to the algorithm proposed by Brandt (1977). The various features of the multi-grid algorithm are examined by testing the algorithm on the system of algebraic equations resulting from Galerkin finite element discretization of the transformed Laplace equation, i.e., the global form of Eq. (4.14).

To construct the multi-grid algorithm, the domain of the problem, Ω, is approximated by a set of uniform grids $\Omega_1, \Omega_2, \ldots, \Omega_N$ with corresponding mesh-sizes $D_1 > D_2 > \ldots > D_N$. For simplicity, let

$$D_K = D_1/2^{(K-1)}$$

where D_1 represents the horizontal mesh size of the coarser grid. The transformation of the nodal values from a coarse grid to the identical nodes in the next finer grid or from fine to coarser grid can be performed by employing a one-dimensional array.

For the purpose of solving the residual equations (4.34) on a coarse grid, and artificial inhomogeneous term is added to our system of equations (Eq.(4.14)), such that

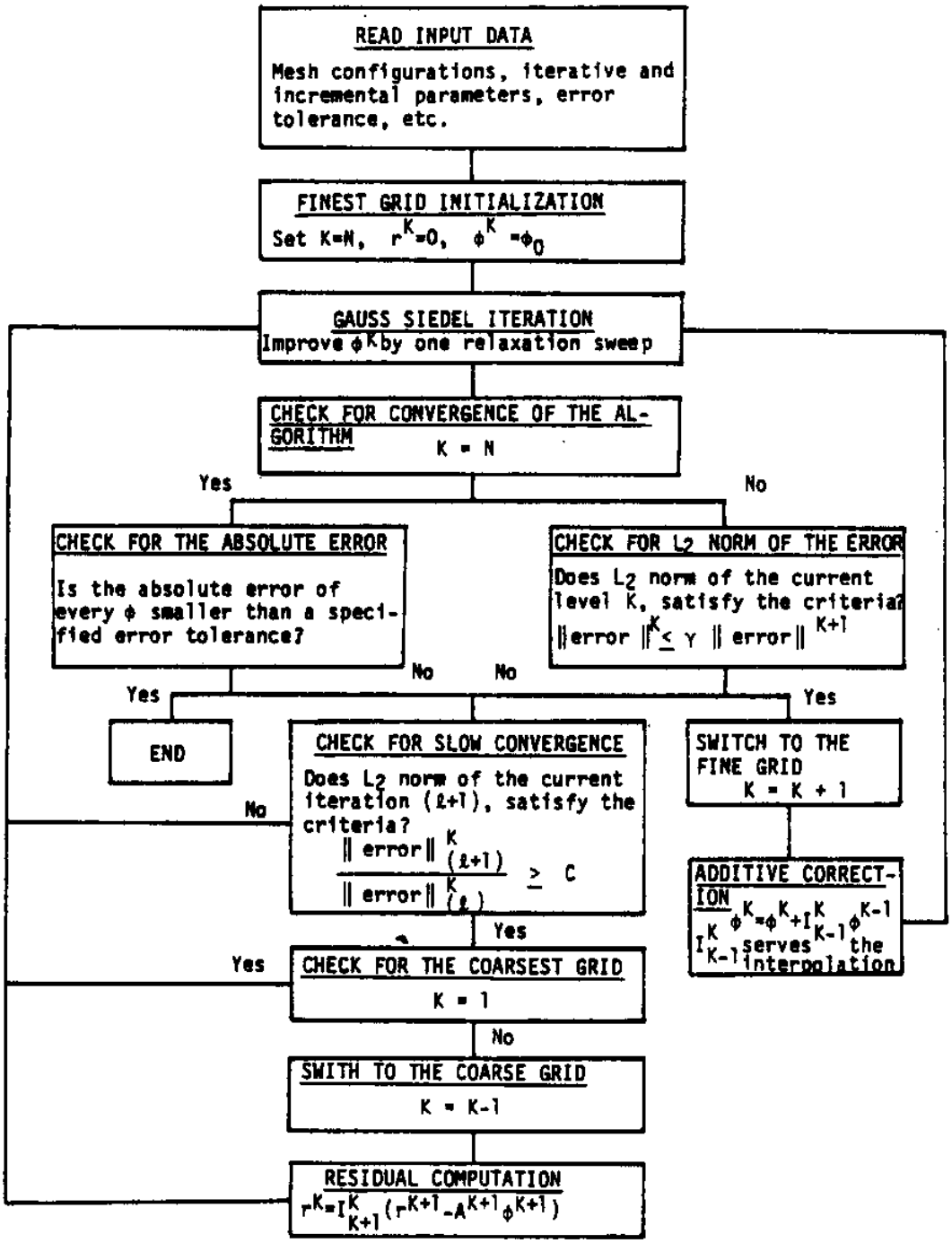

Fig. 4.8 Multi-grid algorithm flowchart.

its values are set equal to zero on the finest grid, , and serve as residuals on coarser grids.

As is illustrated in Fig. 4.8, the algorithm is started by relaxation sweep on the finest grid, and introducing the given Direchlet boundary values (velocity potential distribution over the free surface) as the first approximation. At this step, the equations are the original ones, i.e.,

$$K = N, \quad \phi^K = \phi_0, \quad r^K = 0$$

After one relaxation sweep, the calculations are checked for convergence. The calculation in the finest grid is terminated when the absolute convergence of the form

$$|\phi^{(\ell+1)} - \phi^{(\ell)}| < \varepsilon$$

is satisfied for all ϕ. In the above relation $(\ell+1)$ represents the current iteration and ε is the specified error tolerance found by numerical experiments. The convergence for grids other than the finest grid is examined by comparing the L_2 norm of the working level and the preceding level, using relation (4.39). If the relaxation has not sufficiently converged, a check is made for slow convergence rate using the criterion (Eq. (4.38)). The relaxation sweep continued if slow convergence has taken place at the coarsest grid Ω_1;

otherwise, a switch is made to the next coarser grid. For the coarse grid solution, the residuals in the finer grid are computed and then injected in the coarse grid. When the sufficient convergence is obtained on a coarse grid, the solutions are used to serve as additive corrections on the next finer grid. These steps continue until the relaxation sweep has converged for all of the unknowns on the finest grid.

4.8.4 Numerical Results for the Multi-Grid Algorithm

To evaluate the convergence behavior of the multi-grid algorithm, it was tested together with simple Gauss-Seidel and SOR methods, with a series of numerical model problems of different mesh sizes. The test problem was chosen based on discrete equations resulting from finite element approximate of the Laplace equation along with a specified free surface boundary conations for a solitary wave at its initial position. Thus, the model to be used represents a boundary value problem.

For illustration, a solitary wave with the amplitude H/d=.15 was used and the following model problems with rectangular elements were studied numerically by the said methods.

Model Problem 1. $\Delta x=2$ and 5x65 nodes

Model Problem 2. $\Delta x=1$ and 5x130 nodes

Model Problem 3. $\Delta x=.5$ and 5x260 nodes

The purpose of using the simple Gauss-Seidel and SOR methods was to demonstrate the workability of the proposed algorithm by the numerical work required to perform each method. In employing the SOR method, the optimum value of relaxation parameter, $\omega=1.45$, was found by numerical experiments, which were used in our analysis.

To employ a multi-grid algorithm, which is rather insensitive to the choice of parameters for different mesh-sizes, several numerical experiments were conducted for our model problems. The optimum value of C, the slow convergence criteria, and γ, the convergence criteria for the coarse grids, were found by trial and error. For the values of C=.75, and γ=.5, the algorithm showed the best convergence rate. A calculation was terminated when, for some iteration the absolute error at every node was less than the error tolerance, 10^{-6}, on the finest grid. All calculations were done in double-precision arithmetic.

Comparison of the results is in $\|R\|_2$ -N form, where $\|R\|_2$ is the L_2-norm of the error and N is the equivalent

number of iterations based on the finest grid. The results of these experiments are presented in Table 4.1 and Figs. 4.9 through 4.11. A typical computer output of multi-rid L_2-norm of residual error for each level is presented in Appendix B.

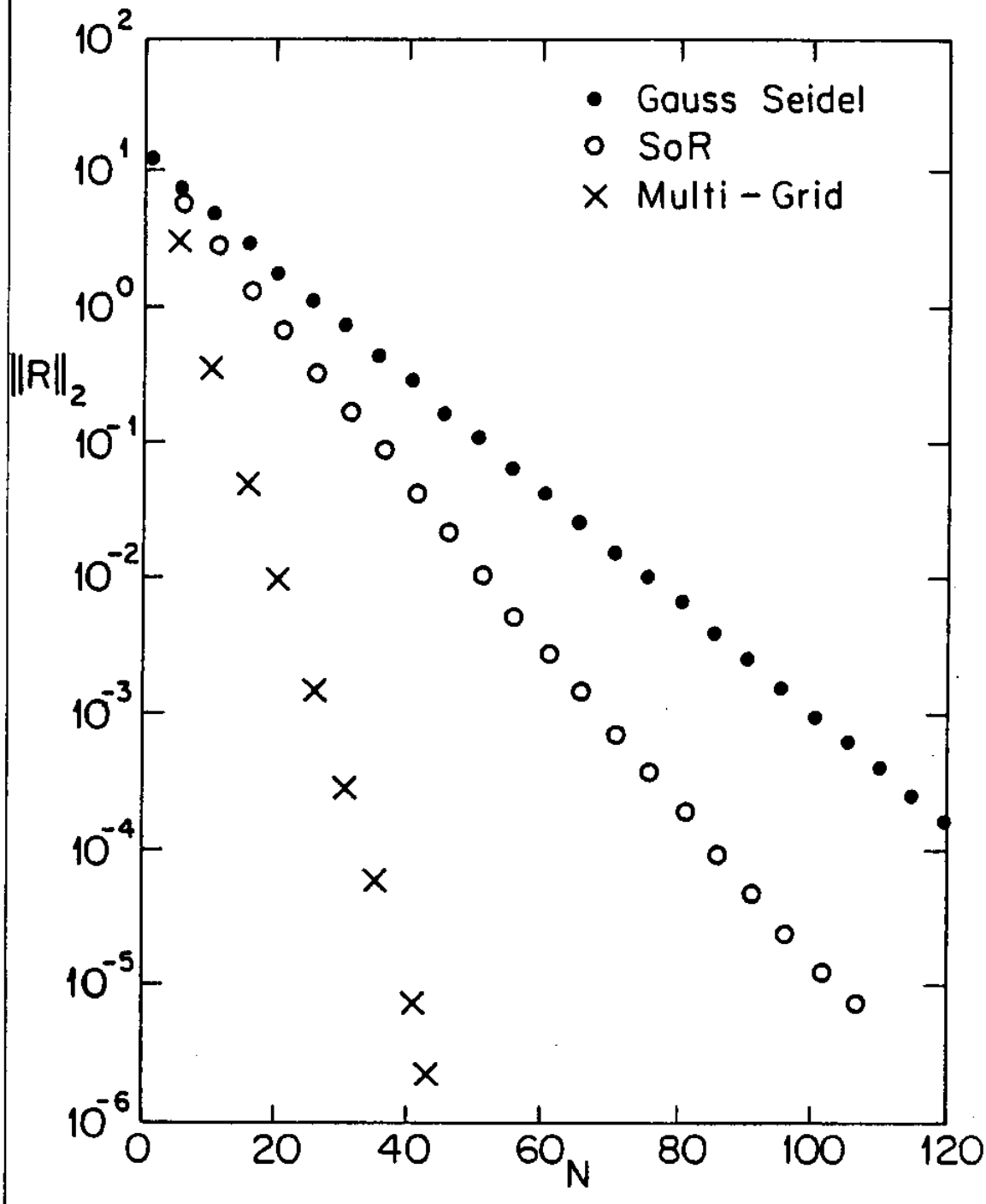

Fig. 4.9 Convergence behavior of the multi-grid algorithm (Model 1).

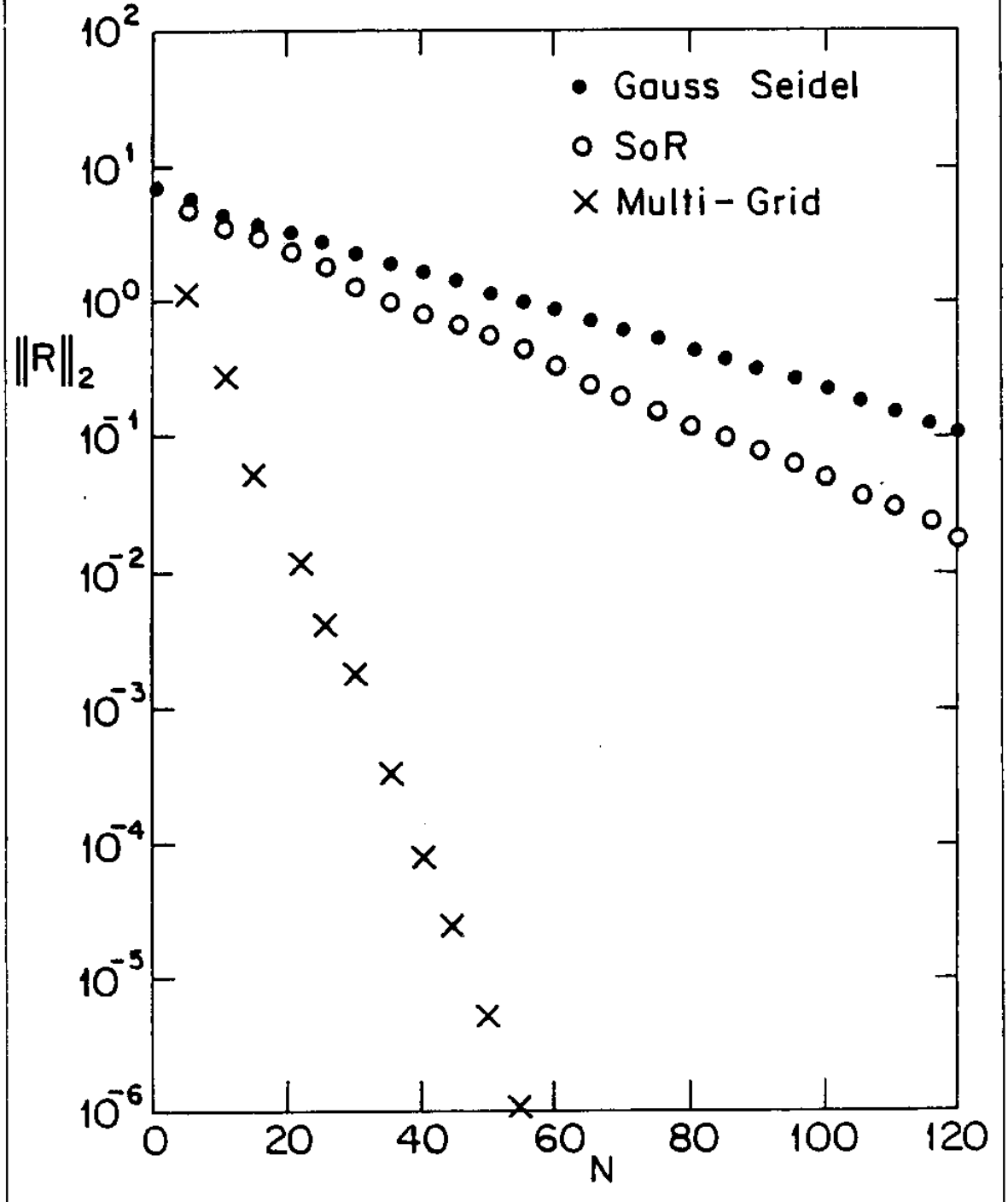

Fig. 4.10 Convergence behavior of the multi-grid algorithm (Model 2).

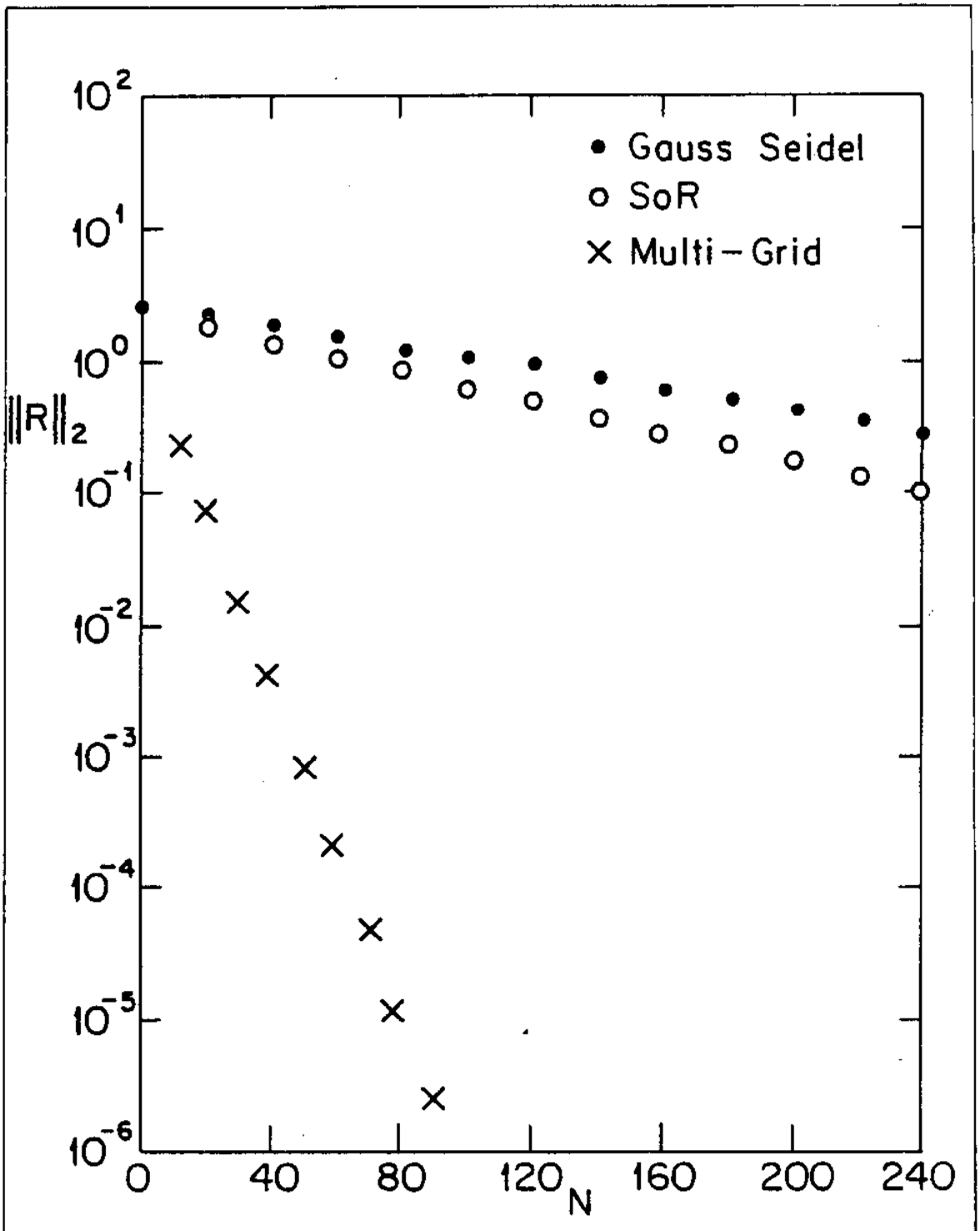

Fig. 4.11 Convergence behavior of the multi-grid algorithm (Model 3).

TABLE 4.1 NUMBER OF ITERATIONS REQUIRED TO OBTAIN AN ERROR OF $\varepsilon = 10^{-6}$ AT EVERY POINT.

Model Problem	Gauss-Seidel	SOR	Multi-Grid
1	154	105	42
2	409	280	56
3	1472	898	92

CHAPTER 5

EXPERIMENTAL EQUIPMENT AND PROCEDURE

5.1 Experimental Objective

The primary objective of experiments was to obtain the water particle velocities beneath a platform as an incident wave strikes the platform for the purpose of comparing with the numerical results. The velocity measurements were conducted using a two-dimensional Laser-Doppler velocimeter (LDV), developed by Raichlen & Lee (1982, 1983). No probe was introduced into the flow field beneath the platform, so the flow was not artificially disturbed. Three different depths were chosen - near the still-water level, mid-depth, and near-the-botom in order to define the depthwise variation of the velocities in the flow beneath the platform region. Two parallel-wire resistance wave gauges were used to measure incident wave and transmitted wave, one upstream and downstream of the platform.

Experiments were conducted at the Keck Hydraulic Laboratory of the California Institute of Technology with the kind permission given by Professor Fredric Raichlen of

Caltech. The wave tank, the wave generation system, and the Laser-Doppler velocimeter system were developed by them over several years of research and development in this general area of long wave experiments. The author does not claim credit in this aspect, instead is very grateful for the assistance received so that the accuracy of the numerical results can be ascertained with the help of the experiments.

5.2 Experimental Equipment

The experimental equipment have been described by a number of publications, for example, Lee, Skjelbreia, & Raichlen (1982), Raichlen & Lee (1982, 1983). However, it is thought that a brief description can be provided here for those readers who do not want to have too much details in this regard.

5.2.1 Wave Tank

The experiments were conducted in a 130 ft. (40 m) tilting flume (Fig. 5.1), located in the Keck Laboratory. The flume has been described in detail by Vanoni et al. (1967).

The channel has a cross-section 43 in. (110 cm) wide and 2 ft. (61 cm) deep. The tank has a glass sidewalls

Fig. 5.1 Photograph of Caltech's 40-m wave tank.

0.5 in. (12.7 m) thick in panels 5 ft. (152.4 cm) long. The bottom of the flume and the short sections of the wall at the ends are made of stainless steel plates.

For the present study, the wave tank was kept horizontal. Circular rails attached to the top of the walls of the flume were adjusted to be parallel to the bottom to form precision tracks for the instrument carriage.

5.2.2 Wave Generator

A piston-type wave generator was installed at the upstream end of the wave tank. The wave generator, shown in Fig. 5.2, consists of the piston which has a vertical plate structure fixed to the underside of a carriage mounted on linear hall bushings and running a horizontal rails, one on each side of the tank. The plate is slight narrower than the wave tank so that it can move freely between the walls. The piston is driven, in a prescribed manner, by an electronically programmed hydraulic system. The principle of the system is the conversion of a programmed input voltage signal into a displacement proportional to the magnitude of the voltage. The overall electro-hydraulic system, shown in Fig. 5.3, consists of a hydraulic power supply, accumulators, a servo-valve, and

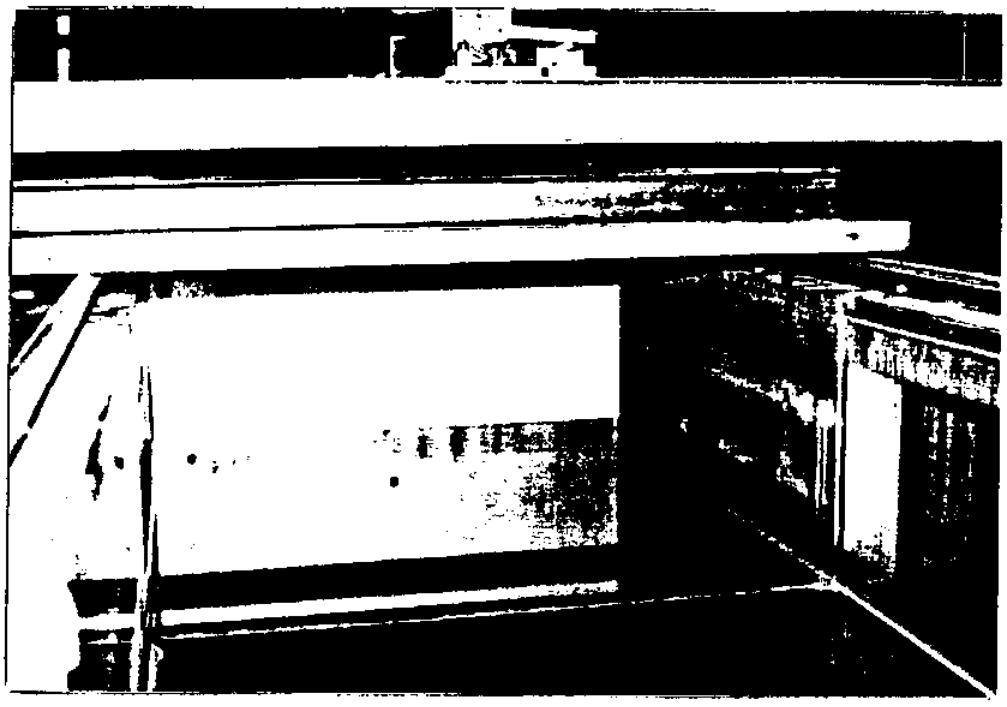

Fig. 5.2 Photograph of the vertical plate wave generator.

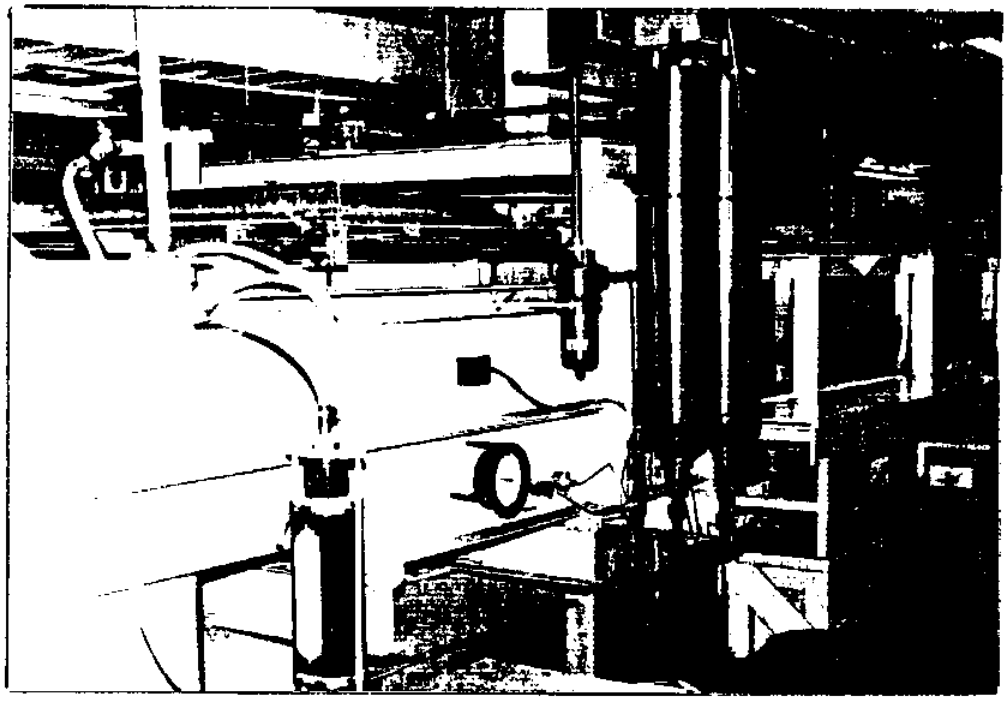

Fig. 5.3 Photograph of the hydraulic supply system.

an electro-servo system. The hydraulic power supply is usually used to charge the accumulators which provide oil volume for operating conditions. The servo-valve directs the hydraulic fluid to either end of a double-acting hydraulic cylinder for a specified voltage from the function generator. The function generator provides the voltage time history which is proportional to the desired displacement-time history; that is, the trajectory of the wave plate.

The motion of the wave is programmed for these experiments using a method described by Goring (1979). The basic principle is simply to drive the wave generator in such a way that it would follow the motion of the water particle velocity under the solitary wave. For long waves, the particle velocity is approximately constant depthwise so that the velocity of the plate is,

$$\frac{ds}{dt} = \bar{u}(s,t)$$

where u(s,t) is the average velocity over the depth, and s is the plate trajectory. Thus, for a given wave of permanent form, this equation can be integrated to define the trajectory of the plate. A typical trajectory s(t) for a solitary wave is shown in Fig. 5.4. An example of the programmed wave plate displacement and actual water

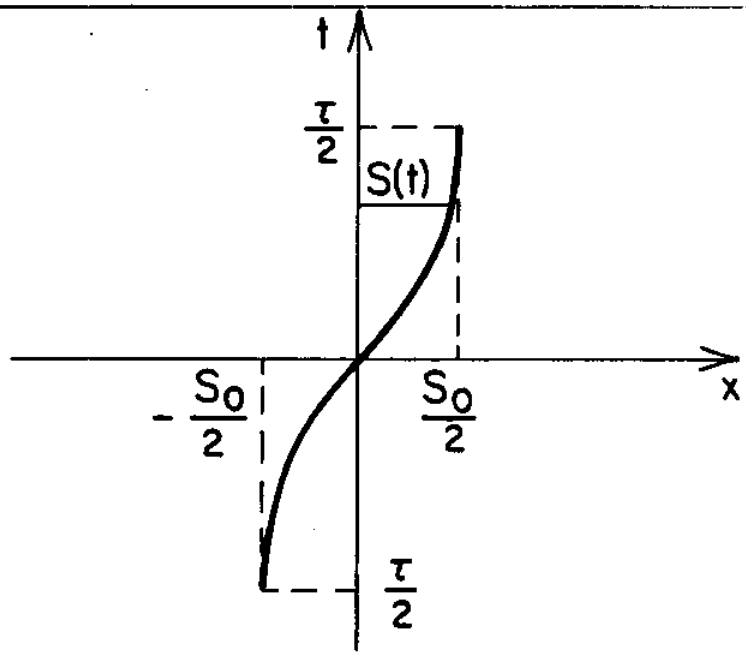

Fig. 5.4 Typical wave plate trajectory for a solitary wave. (S_0=Plage stroke, τ= duration of motion).

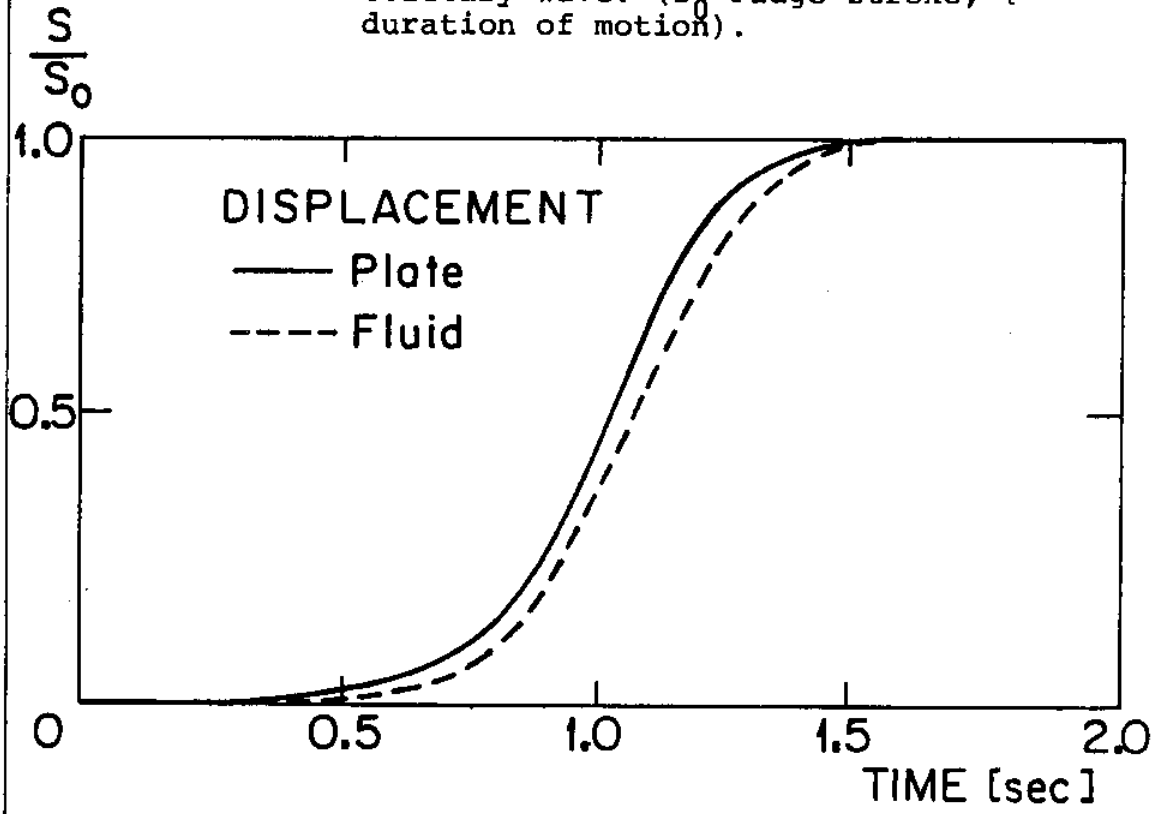

Fig. 5.5 Example of the programmed plate displacement and actual water particle displacement for a solitary wave.

particle displacement is shown in Fig. 5.5.

5.2.3 Platform

The platform constructed for the experiment had a flat, horizontal underside, and a vertical front face as high as the wave tank sidewalls to prevent incident waves from splashing over the top of the platform.

The platform, constructed from wood material, was 4 ft. (122 cm) long and slightly narrower than the tank. It was placed approximately 25 m from the wave generator. Weights were placed inside the platform box to prevent upward movement; clamps were used to resist horizontal movement of the structure due to incident wave forces.

5.2.4 Measurement of the Wave Amplitude

Parallel-wire resistant wave gauges were used to obtain variations of the water surface profile with time. The wave gauges, composed of 0.01 in. (.025 cm) in diameter of stainless steel wires, were spaced 0.12 in. (.31 cm) apart. The wires were stretched and parallel to a frame constructed of a stainless steel rod. The wires were electrically insulated from each other and from the frame. When the gauge was immersed in water, a current which varies with the depth of immersion could pass from

one wire to the other. The output signal from the wave gauge was proportional to the resistance in the circuit which, in turn, was proportional to the depth of immersion of the wires.

Before each set of experiments, the wave gauge was calibrated by immersing it in still-water to various known depths and then retracting it.

Two wave gauges were used to measure the water surface upstream and downstream the platform; mainly, the incident waves and transmitted waves.

5.2.5 Water Particle Velocity Measurement

A two-dimensional Laser-Doppler velocimeter (LDV) system was used to make velocity measurements. The reference beam method (Fig. 5.6), developed by Raichlen & Lee (1982, 1983), was used in the system. Only the basic principles of Laser-Doppler velocimeter are discussed here; a complete description of the LDV system used for the present study is given by Raichlen & Lee (1982, 1983).

In using the reference beam method, a laser beam from a 5-mw Helium-Neon laser is divided into two reference beams and a scattering beam. The two reference beams are very much dimmer than the scattering beam. These beams

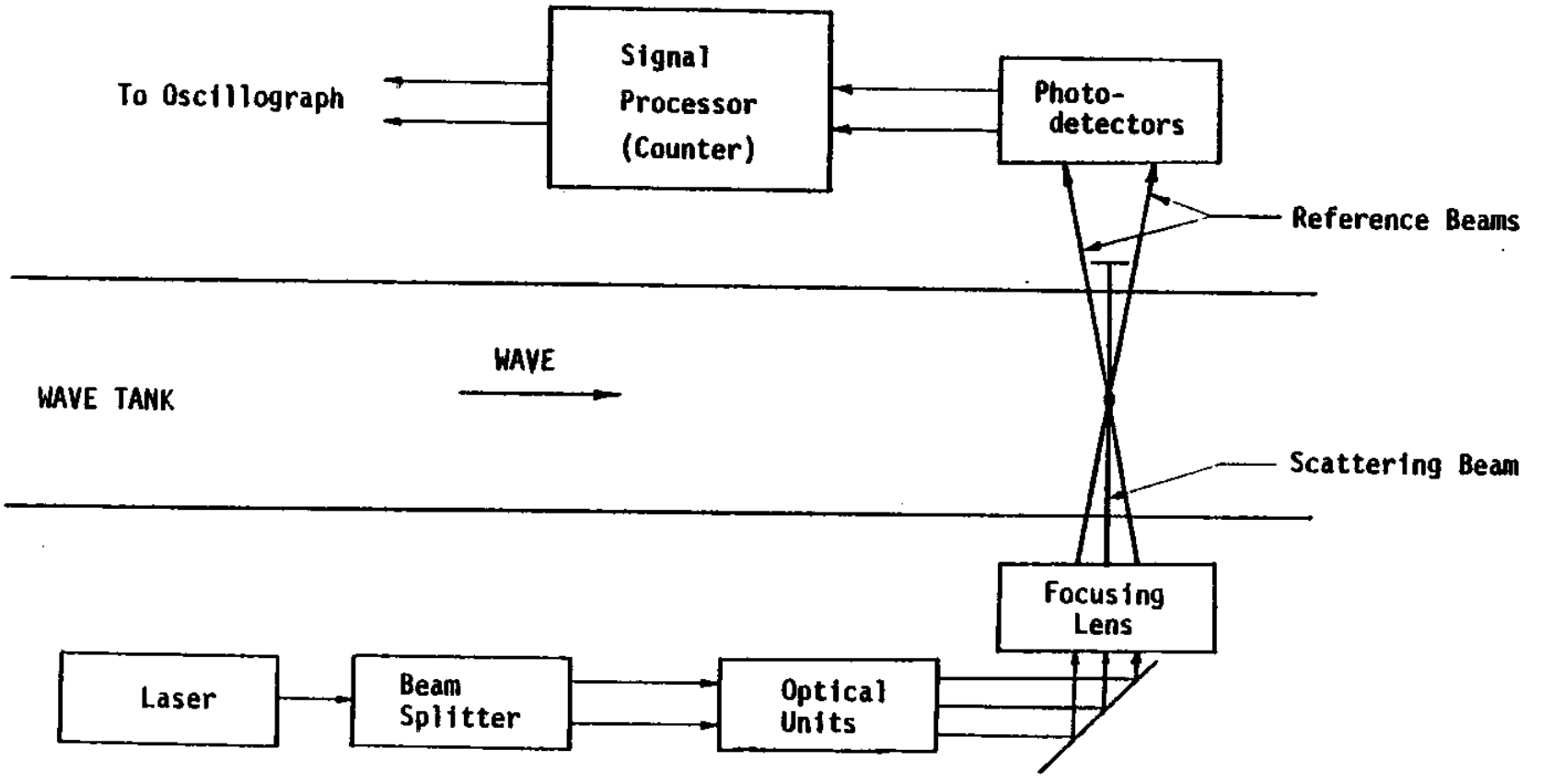

Fig. 5.6 Schematic diagram of the two-dimensional LDV system.

pass through two Bragg cells for the purpose of frequency shift. The two reference beams and the scattering beam are focused by an optical system to a location near the center of the wave tank; each reference beam is then directed into a photodetector. When a small particle in the fluid crosses the focal volume of the three beams, it will scatter a small amount of light from the scattering beam in the direction of the reference beam with slight frequency shift caused by the water particle velocity. This frequency shift is denoted as the Doppler frequency, . The light from the reference beam and the scattered light produce a current from the photodetector which has the amplitude

$$I(t) = A(t)\cos(\nu_d t)+C(t) \qquad (5.1)$$

where t is the time, and the parameters A(t), and C(t) depend on the intensities of the light beams and the optical properties of the particle. The quantity ν_d is measured by a photodetector and associated electronics; it can be expressed as,

$$\nu_d = \frac{2n}{\lambda} \vec{u} \cdot (\vec{e}_r \cdot \vec{e}_s) \qquad (5.2)$$

where

n is the index of refraction of the medium,

$\vec{u}$ is the particle velocity,

λ is the wavelength of the laser light in vacuum,

$\vec{e}_r$ is the unit vector in the direction of reference beam, and

$\vec{e}_s$ is the unit vector in the direction of scattering beam.

The Doppler signal output based on Eqs. (5.1) and (5.2) cannot define the direction of the velocity components. In order to overcome this difficulty, the LDV system used is equipped with a frequency shifter. The frequency shifter consists of two Bragg cells (which operate at a nominal frequency of about 40 MHz) and a frequency synthesizer with phase-locked-loops (PLL). The prefrequency shift between the reference beams and the scattering beam used for the present experiments is 86.92 KHz. Based on the orientation of the laser beams for the present experiments, the velocity components can be determined as follows:

$$u = 1.979\ [(\nu_{d_1} - 86.92) - 0.961597\ (\nu_{d_2} - 86.92)]$$

$$v = -2.044\ [(\nu_{d_1} - 86.92) + 1.030055\ (\nu_{d_2} - 86.92)] \qquad (5.3)$$

where u represents the measured horizontal component of water particle velocity in cm/sec, v is the measured vertical component of water particle velocity in cm/sec,

ν_{d_1} and ν_{d_2} of the measured Doppler frequency in KHz of the two reference beams.

The Doppler signal from transmitting optics (Fig. 5.7) mounted on one side of the flume is received by the photodetector mounted on the other side of the flume and is processed with an electronic counter. When the system detects a Doppler signal corresponding to the passage of a particle through the focal volume, it first amplifies and filters the signal, then with a sufficient amplitude and period of the Doppler frequency, a voltage proportional to the Doppler frequency is provided.

The counter was calibrated before and after each experiment by imposing sinusoidal signals with known frequencies; in this way, the voltage output from the counter was related to the Doppler frequency. Once the Doppler frequency, ν_{d_1}, was evaluated the water particle velocities could be computed from Eq. (5.3).

5.2.6 Laser-Doppler Carriage

The Laser-Doppler and its optical components were firmly attached to a carriage which was isolated from the wave tank and rested on three legs (Fig. 5.8). The laser optics were mounted on one side of the carriage and the

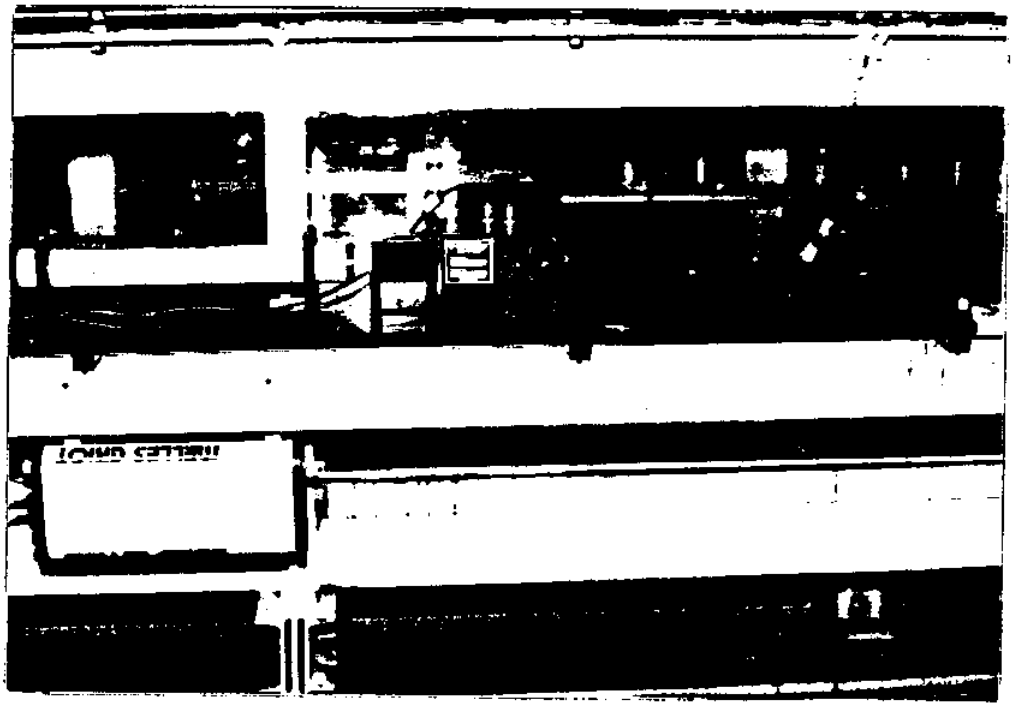

Fig. 5.7 Photograph of the transmitting end of the Laser-Doppler velocimeter.

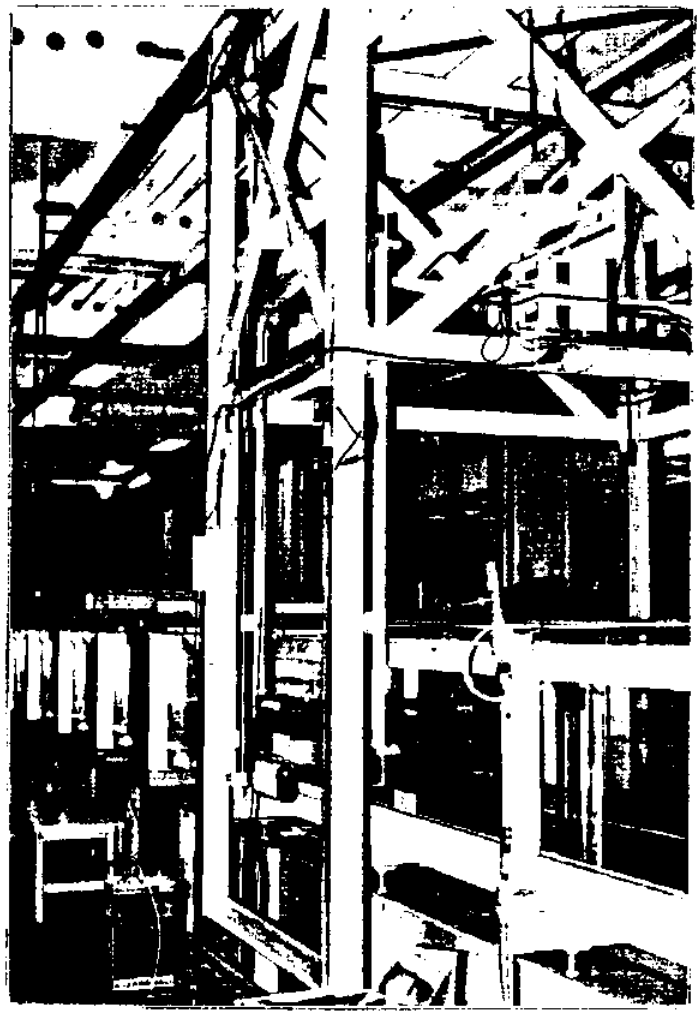

Fig. 5.8 Photograph of the Laser-Doppler velocimeter carriage.

photodetector was mounted on the other side. The carriage was provided to facilitate moving the laser along the channel and through the depth without changing the orientation of the laser beams. A precision scale was attached to the side of the carriage for measuring the vertical position of the carriage.

5.3 Experimental Procedure

In all of the experiments, the platform was placed approximately 21 m. from the wave generator. Two resistance wave gauges were used to measure the incident wave and transmitted wave; upstream and downstream of the platform, respectively.

Each set of experiments consisted of generating a reproducible solitary wave and measuring the velocity components at two positions: near the leading edge, some distance from the leading edge along the platform, and at different depths at each position. Wave and geometric parameters, such as the wave height, the still-water depth, and the soffit clearance were kept the same during each set of experiments.

Before the beginning of each set of experiments run, the still-water surface elevation was adjusted to the

proper level height, and the wave generator was programmed to generate the desired wave. The wave gauges were calibrated by immersion to different known depths, returning the gauge to its original position, and noting the corresponding voltage change for each change by computer. The Laser-Doppler velocimeter was calibrated using an electronic counter by relating voltage output from the counter to the Doppler frequency. To measure the velocities at different vertical positions, the laser focal volume was moved using the carriage. The variation of the water surface elevation and the voltage output from the LDV counter system were recorded, as a function of time, by digital computer and later were plotted.

CHAPTER 6

PRESENTATION AND DISCUSSION OF RESULTS

Numerical and experimental results are presented in this chapter which deal with the wave hydrodynamic effects on a horizontal platform. In Section 6.1, a brief summary of the solitary wave theory is provided and different theories are discussed. In Section 6.2, the water particle velocities within a solitary wave are computed and compared to Laser-Doppler measurement to demonstrate the usefulness of LDV techniques in velocity measurement. Section 6.3 examines the numerical stability of a solitary wave traveling in uniform depth. In Section 6.4, the effect of artificial viscosity is examined through numerical experiments to examine the applicability of this method to damp the unwanted surface oscillations. Numerical and experimental results of water particle velocities beneath a platform at various depths and locations along the platform are presented in Section 6.5 and the difficulties encountered in LVD measurement are reviewed. In Section 6.6, the results of transmitted wave downstream a platform are showed. Section 7 concludes the chapter by presenting the numerical and experimental

results of wave uplift pressure on a platform.

6.1 Incident Wave

As mentioned previously, it was important to choose a type of incident wave which represents a finite-amplitude wave which was propagating through shallow water, and it can be conveniently represented mathematically. In Chapter 1, it was stated that a solitary type of wave was chosen as the incident wave. A solitary wave is a permanent two-dimensional and irrotational flow of fluid which consists of a single wave form lying entirely above the still water level and propagates at constant velocity without a change in form. There are three theoretical solutions of the solitary wave equations which are often referred to in the literature. Boussinesq (1871) obtained an analytical solution for the wave profile, wave propagation speed, and the water particle velocities. McCowan (1891) carried out the solution to the first-order approximations and determined the wave profile and other characteristics of the solitary wave. Laitone (1963) obtained a solution similar to that of Boussinesq, but his solution contains higher-order terms. Although McCowan and Laitone solitary waves result from higher-order theories, the Boussinesq solution is found to fit

experimental data with better accuracy. In the following, the solutions of Boussinesq (1871) will be summarized.

1. Wave profile:

$$\eta = H \operatorname{sech}^2 \sqrt{\frac{3H}{4d}}\ \frac{x}{d} \quad \text{(where } x = x - ct\text{)}$$

2. Wave speed:

$$c = \sqrt{g(d+H)}$$

3. Water particle velocity:

   a. horizontal component:

$$\frac{u}{\sqrt{gd}} = \frac{\eta}{d}\left\{1 - \frac{1}{4}\frac{\eta}{d} + \frac{d}{3}\left(\frac{d}{\eta}\right)\left[1 - \frac{3}{2}\left(\frac{y}{d}\right)^2\right]\frac{d^2\eta}{dx^2}\right\}$$

   b. vertical component:

$$\frac{v}{\sqrt{gd}} = -\frac{y}{d}\left\{\left[1 - \frac{1}{2}\frac{\eta}{d}\right]\frac{d\eta}{dx} + \frac{1}{3}d^2\left[1 - \frac{1}{2}\frac{y^2}{d^2}\right]\frac{d^3}{dx^3}\right\}$$

Based on the theoretical expressions summarized in the previous section, a solitary wave is completely defined for a given still-water depth, d, and amplitude H. Experimental results by French (1969) indicated that no theoretical profile fits the experimental data better than that of Boussinesq in the region of the wave crest. Since much of the wave impact on a platform whose underside is situated above he still-water depth involves the region

near the crest of the wave, the Boussinesq profile is then a proper model for this study.

6.2 Water Particle Velocities in Solitary Waves

To test the accuracy of our numerical model, it is constructive to compare the computed velocity components to that of Boussinesq solutions and LDV experiments. The velocity components can be obtained by having the nodal values of the velocity potential in the numerical model. This can be shown by using the definitions of velocity potential, that is,

$$u = \phi_{,x} = \phi_{,\xi}\xi_{,x} + \phi_{,\eta}\eta_{,x} \quad Q$$

$$v = \phi_{,x} = \phi_{,\eta}\eta_{,y} \quad Q$$

For a typical element, we can write

$$u = \sum_{i=1}^{4} \left[\xi_{,x}\psi_{i,\xi}(\xi,\eta) + \eta_{,x} Q \psi_{i,\eta}(\xi,\eta) \right] \phi_i$$

and

$$v = \sum_{i=1}^{4} \eta_{,y} Q \ \psi_{i,\xi}(\xi,\eta)\phi_i$$

where u, and v are considered to be evaluated at the center of the element. The velocity components at a particular depth can then be obtained by a simple interpolation of computed velocities on the elements.

The horizontal and vertical water particle velocities within a solitary wave for relative wave height of $\varepsilon = 0.11$ are computed and compared with that of Boussinesq's theory and Laser-Doppler velocimeter measurement obtained by Lee, Skjelbreia & Raichlen (1982). The results of the horizontal water particle velocities are presented in Figs. 6.1 through 6.3 and the vertical water particle velocities are shown in Figs. 6.4 through 6.6 for three different depths. These depths vary from about mid-depth to near-the-still-water level ($z/d = 1.0$). Each figure shows the variation of the normalized water particle velocity with normalized time, $t\sqrt{g/d}$. The depths chosen are $z/d = 0.92$, 0.78, and 0.45.

The numerical results of the horizontal water particle velocity at these depths are slightly larger than the Boussinesq theory; the maximum deviation is about 4%. In general, the experimental results agree better with the numerical results for $t\sqrt{g/d} < 0$. The maximum deviation of about 2% can be observed between the numerical and experimental results. The slight deviation between the numerical results and that of Boussinesq's theory may be explained by the fact that lowest-order solution is used to define the velocity potential at the free surface in the numerical model. However, the numerical results agree

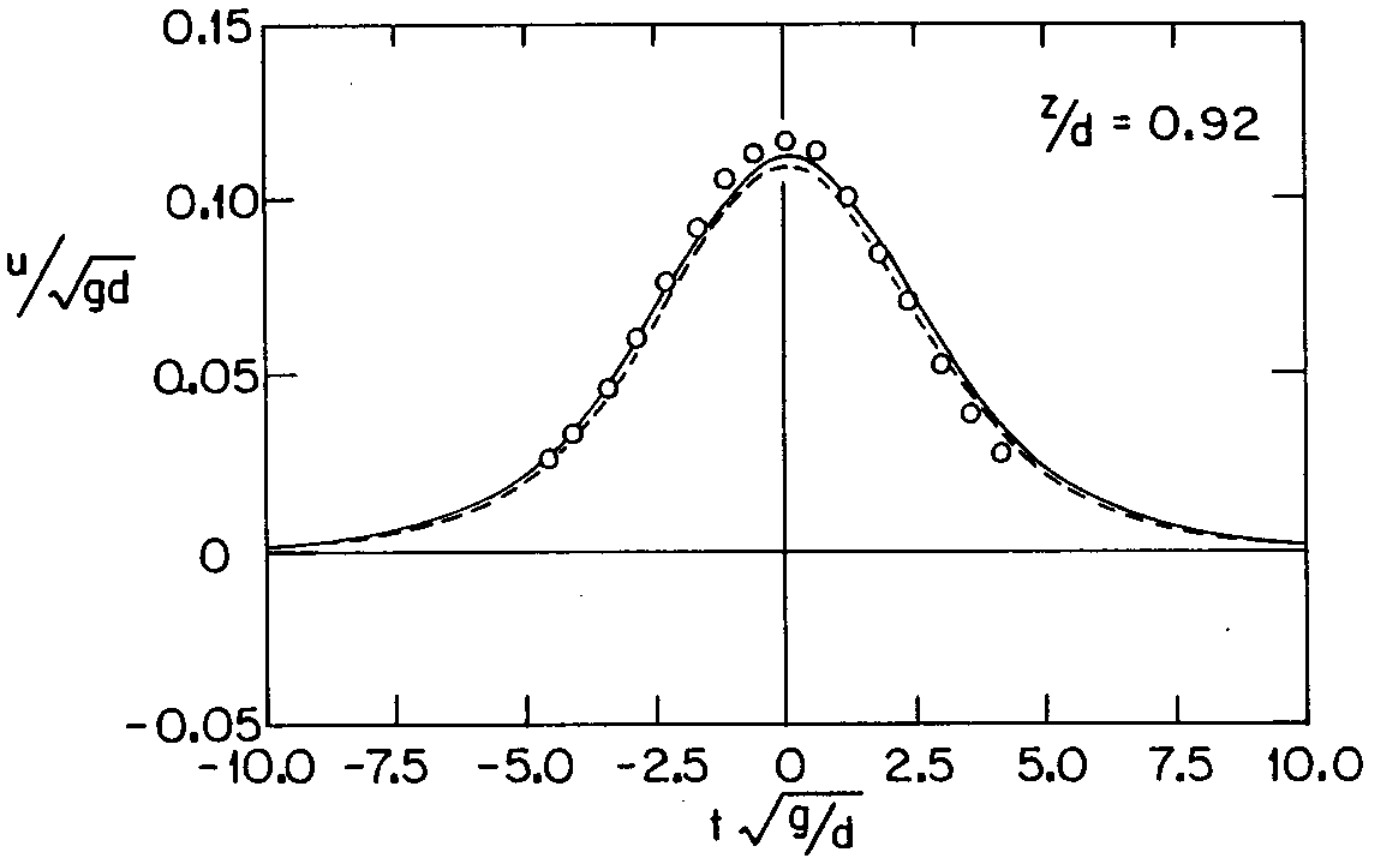

— present numerical model ○ experiment - - - Boussinesq's equation

Fig. 6.1 Horizontal water particle velocity in a solitary wave. (ε= 0.11, z/d = 0.92).

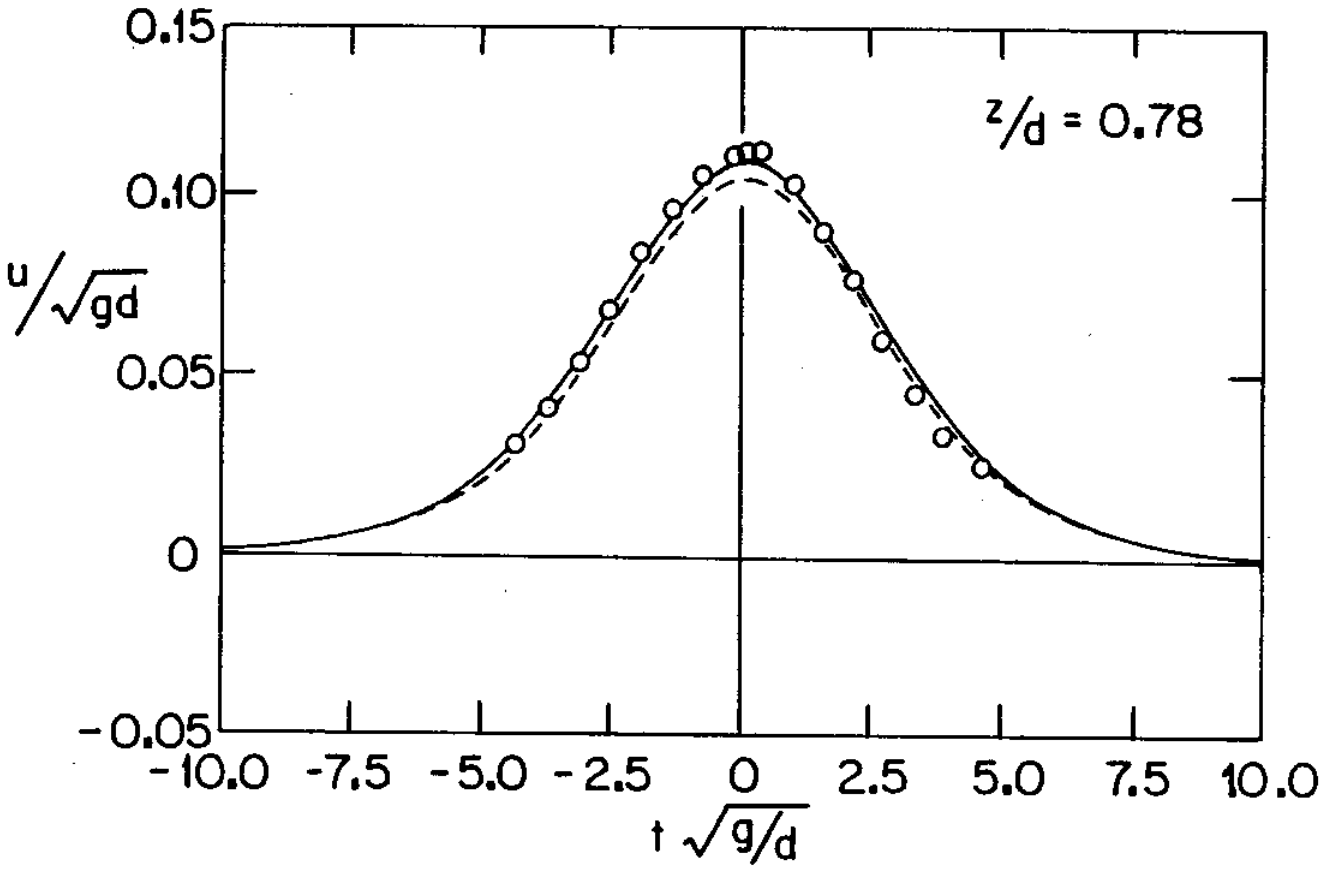

Fig. 6.2 Horizontal water particle velocity in a solitary wave. (ε=0.11, z/d=0.78).

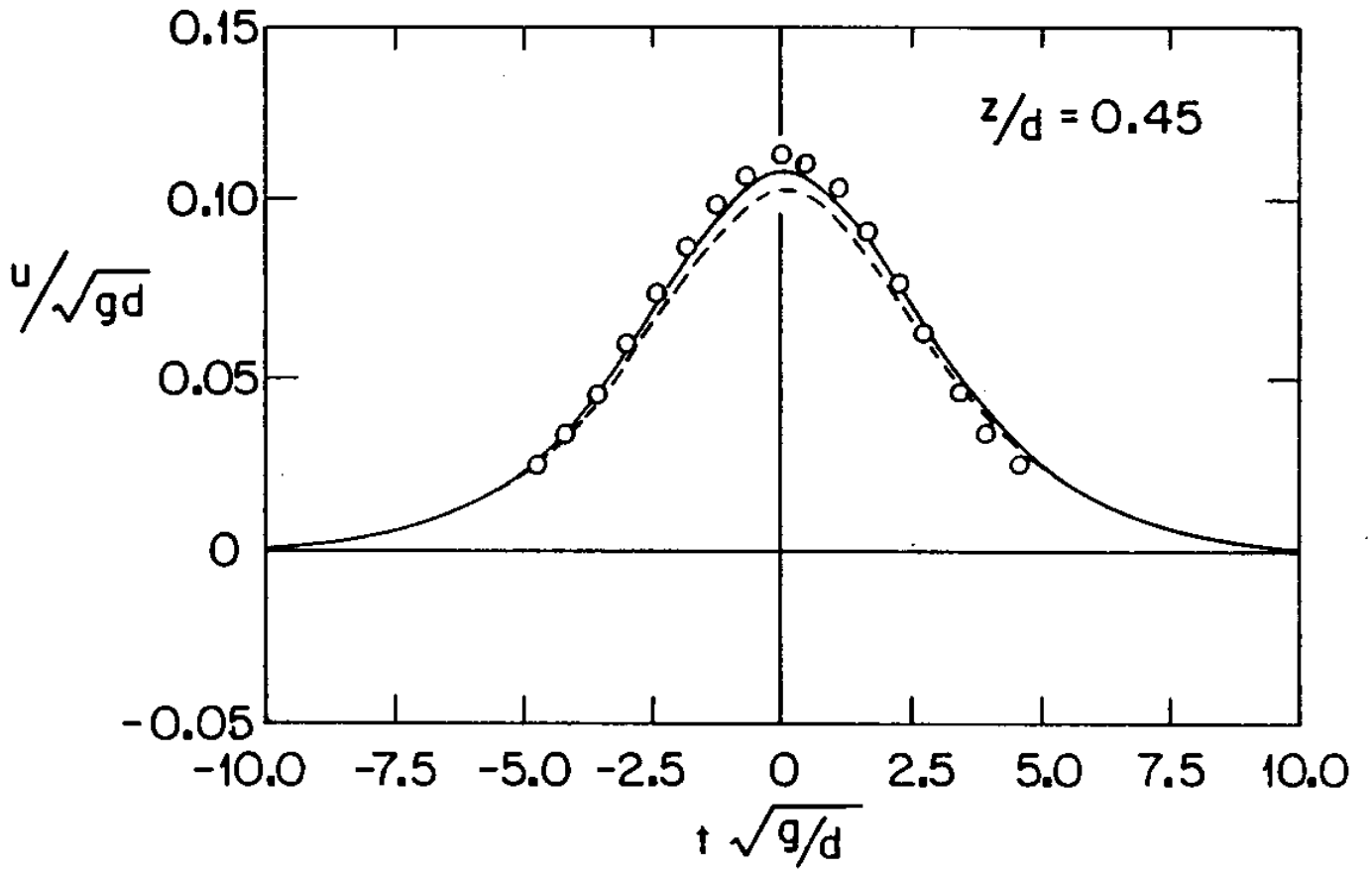

—— present numerical model ○ experiment - - - Boussinesq's equation

Fig. 6.3 Horizontal water particle velocity in a solitary wave. (ε=0.11, z/d=0.45).

well with the experimental data, perhaps agreeing better than Boussinesq's theory.

The vertical water particle velocities for three different depths are shown in Figs. 6.4 through 6.6. As can be seen, the numerical results agree well with that of Boussinesq's theory as well. The experimental data show more critical comparison for vertical velocities than horizontal water particle velocities. But, considering the magnitude of the vertical velocity and its rapid phase shift from positive to negative, it can be concluded that the deviation of the experimental data is not as severe as it appears. The asymmetric nature of the experimental data which appear to be more evident in vertical velocity components is probably due to the asymmetry of the experimentally generated wave profile (see Lee, Skjelbreia & Raichlen (1982) for discussion of explanation of the results). These results demonstrate the usefulness of the Laser-Doppler measurement as a mean of comparison for the present study.

6.3 Propagation of Solitary Waves in a Constant Depth Region

As was previously discussed in Chapter 4, to construct the free surface motion, the equations of

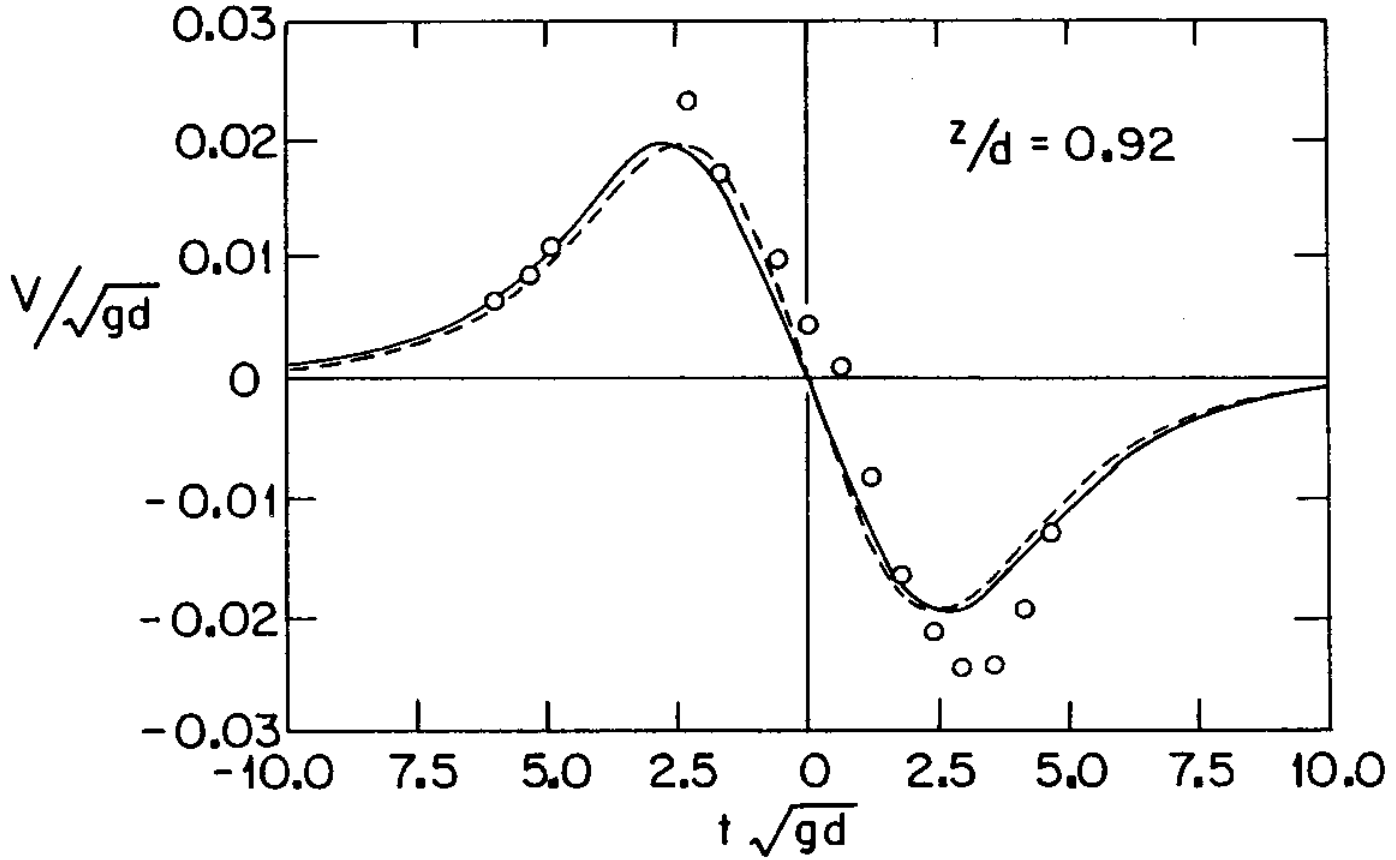

Fig. 6.4 Vertical water pargicle velocity in a solitary wave. (ε=0.11, z/d=0.92).

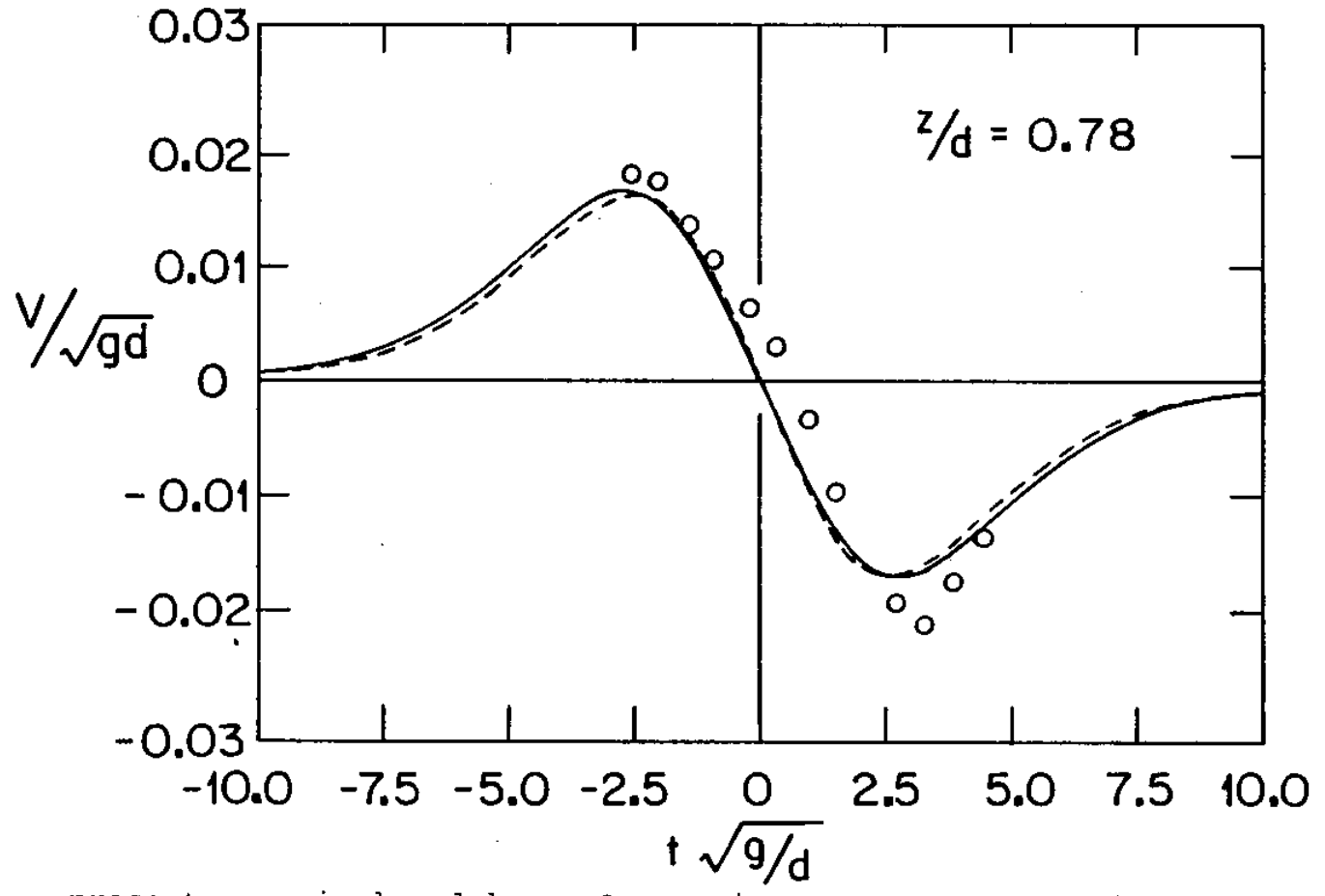

Fig. 6.5 Vertical water particle velocity in a solitary wave. (ε=0.11, z/d=0.78).

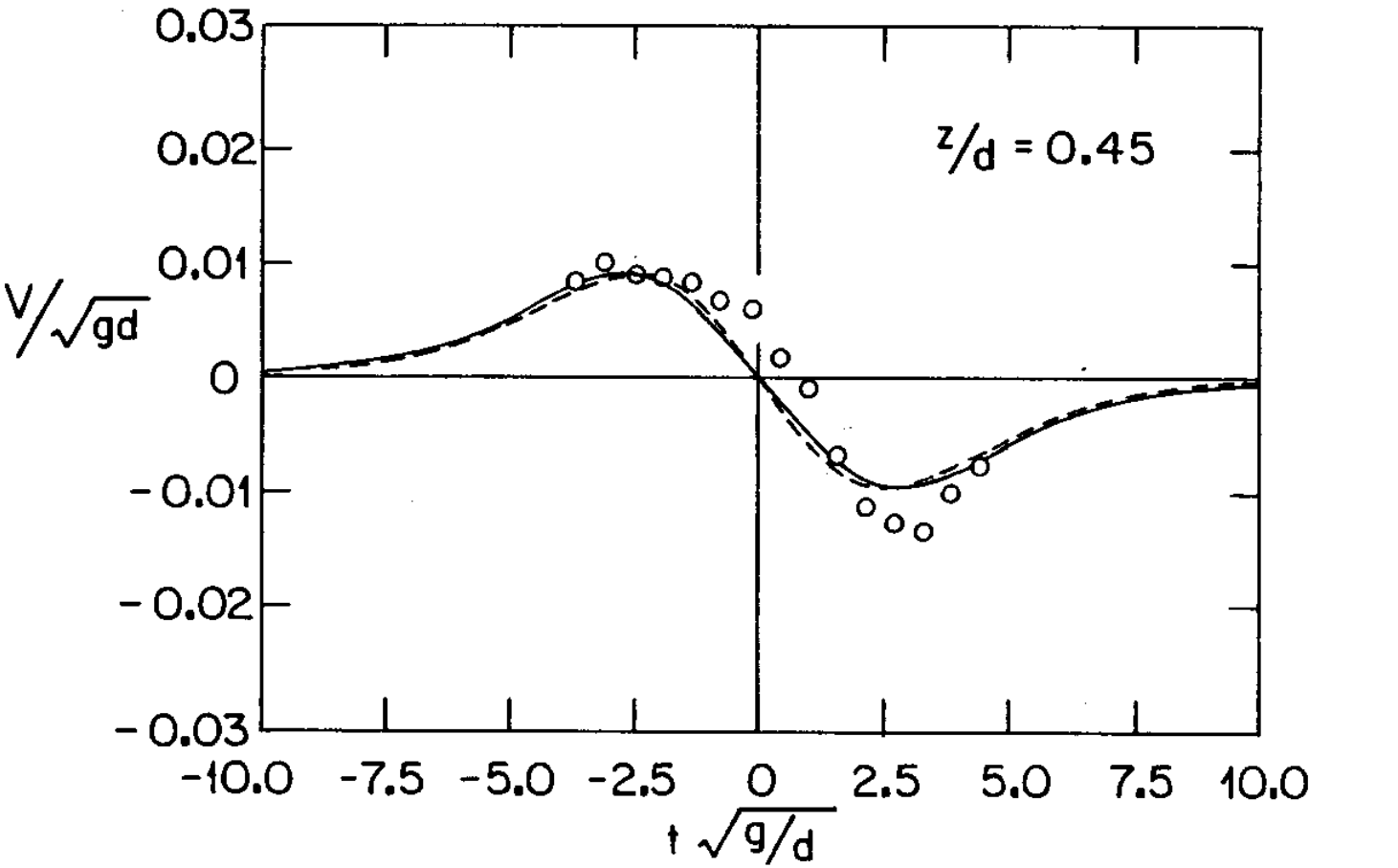

Fig. 6.6 Vertical water particle velocity in a solitary wave. (ε=0.11, z/d=0.45).

kinematic and dynamic boundary conditions are integrated in time by using an explicit scheme. In practice, the explicit schemes require the time step be chosen smaller than some critical time increment for a stability condition to be satisfied. In the present problem, the Courant, Friedrichs, and Lewy (1928) condition is used. Recalling the relation (4.27), the time increment is chosen such that,

$$\Delta t < \frac{\Delta x}{NC}$$

Numerical experiments are usually performed to determine the time increment, Δt, with which the numerical model exhibits stable condition.

In the test program, a solitary wave with relative height of $H/d = 0.1$ is considered. The mesh sizes are chosen based on four elements through the depth and $\Delta x = 2.0$ in. The number of nodes in the x-direction is chosen large enough to provide enough region for the wave to propagate inside the x-coordinate. The time increment Δt is then found by the numerical experiments.

Figures 6.7 through 6.10 represent the numerical results of the propagation of a solitary wave with a relative height of $H/d = .1$, in a uniform region. The initial profile and the profiles after the wave has

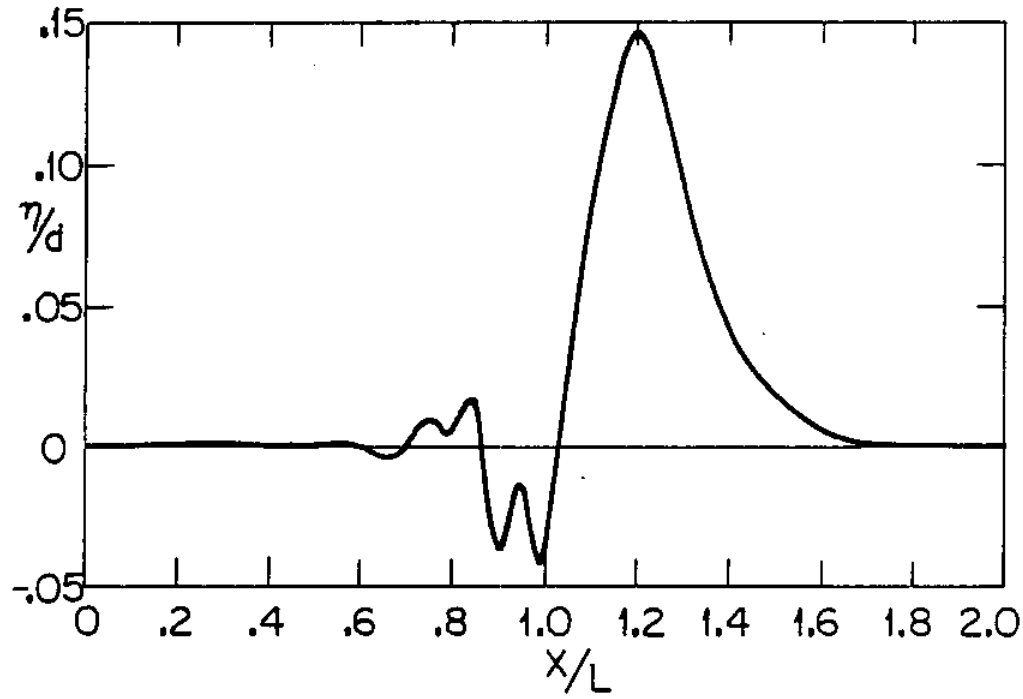

Fig. 6.7 Wave profile calculated using the numerical scheme. (CFL = 1).

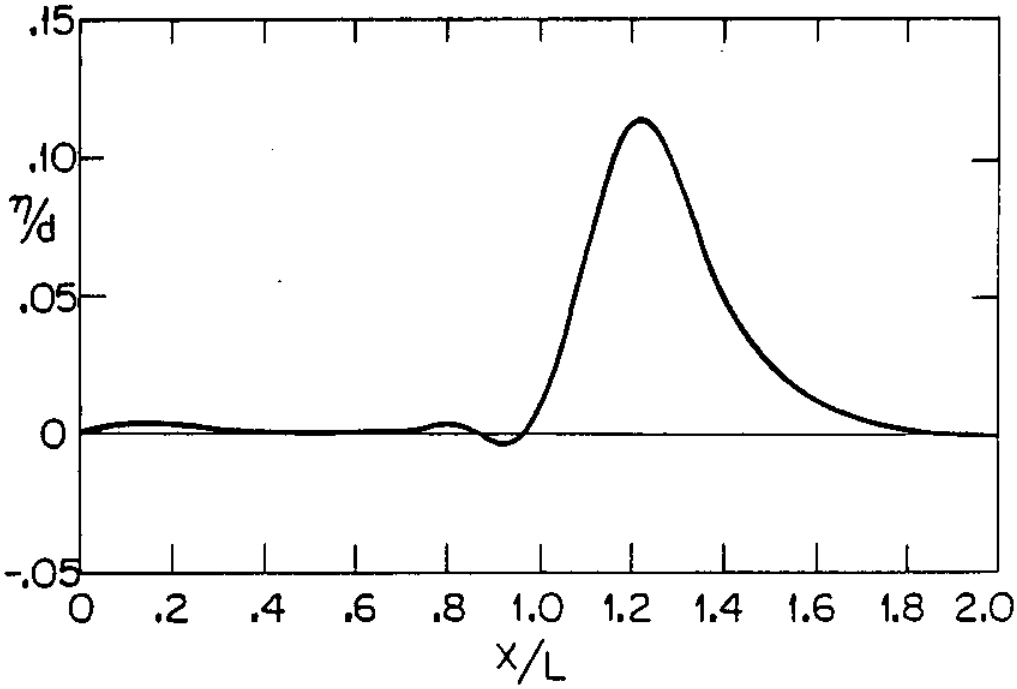

Fig. 6.8 Wave profile calculated using the numerical scheme (CLF = 1/2).

traveled one wave length are examined for different time increment (different CFL number).

As indicated in these figures, for large time increments the shape of the original solitary wave changes and its amplitude increases after it propagates for some time. Some small numerical oscillations also exist at the trailing edge of the solitary wave. As Δt reduces, these oscillations get smaller and the solitary wave remains more the same as the original profile. However, the oscillations at the trailing edge of the wave cannot be completely avoided, but the percentage of oscillations (referring to the negative wave amplitude at the tail end of the wave divided by the maximum amplitude at the wave crest) can become quite minor by selecting small time increments Δt. These small oscillations are errors probably due to the truncation and round-off errors inherent in the numerical method. Figure 6.11 presents the numerical results of the propagation of a solitary wave with the amplitude ratio H/d = .1, using CFL equal to 1/8. The initial profile and the profiles obtained after 160 steps, 340 steps, and 520 steps of computation are also shown for comparison. As it can be seen, the amplitude of the solitary wave after 520 times steps of computation remains the same as the original profile. The

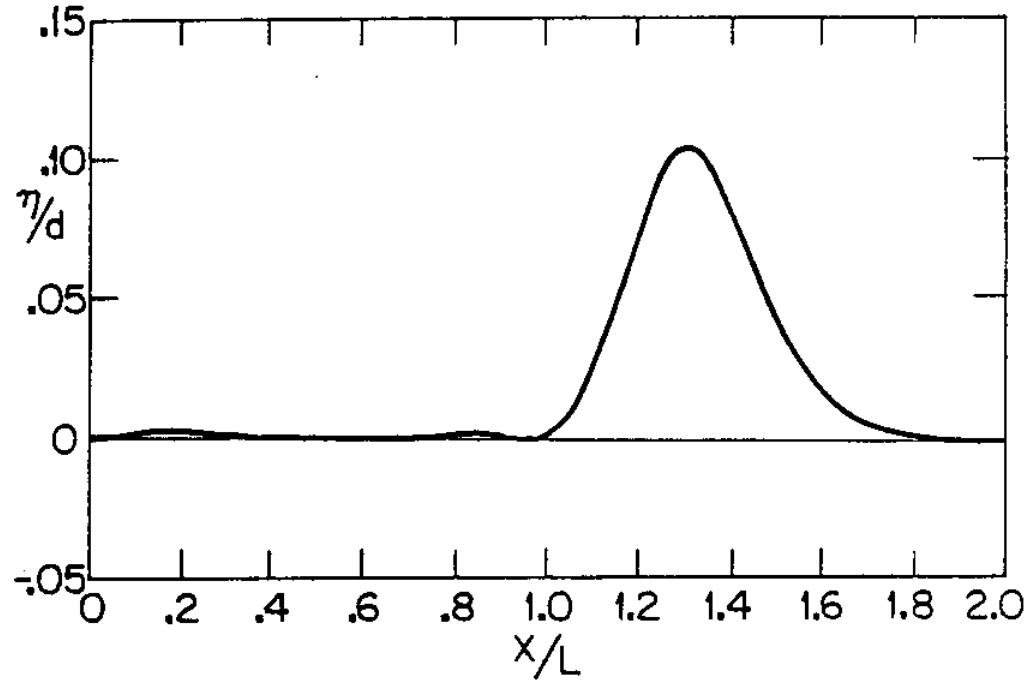

Fig. 6.9 Wave profile calculated using the numerical scheme (CLF=1/4).

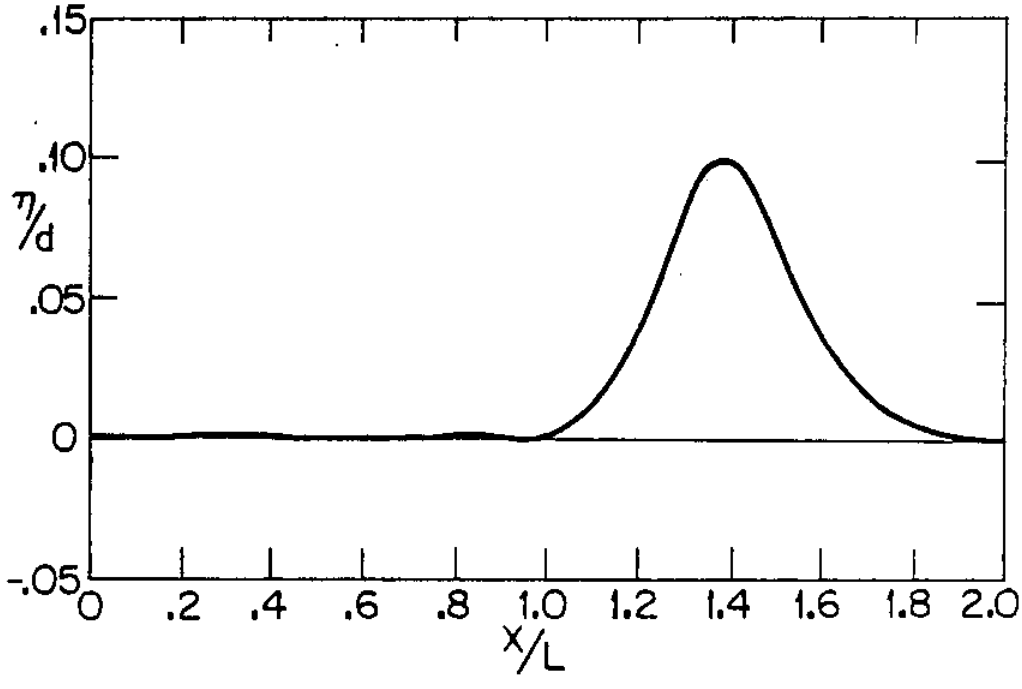

Fig. 6.10 Wave profile calculated using the numerical scheme (CFL=1/8).

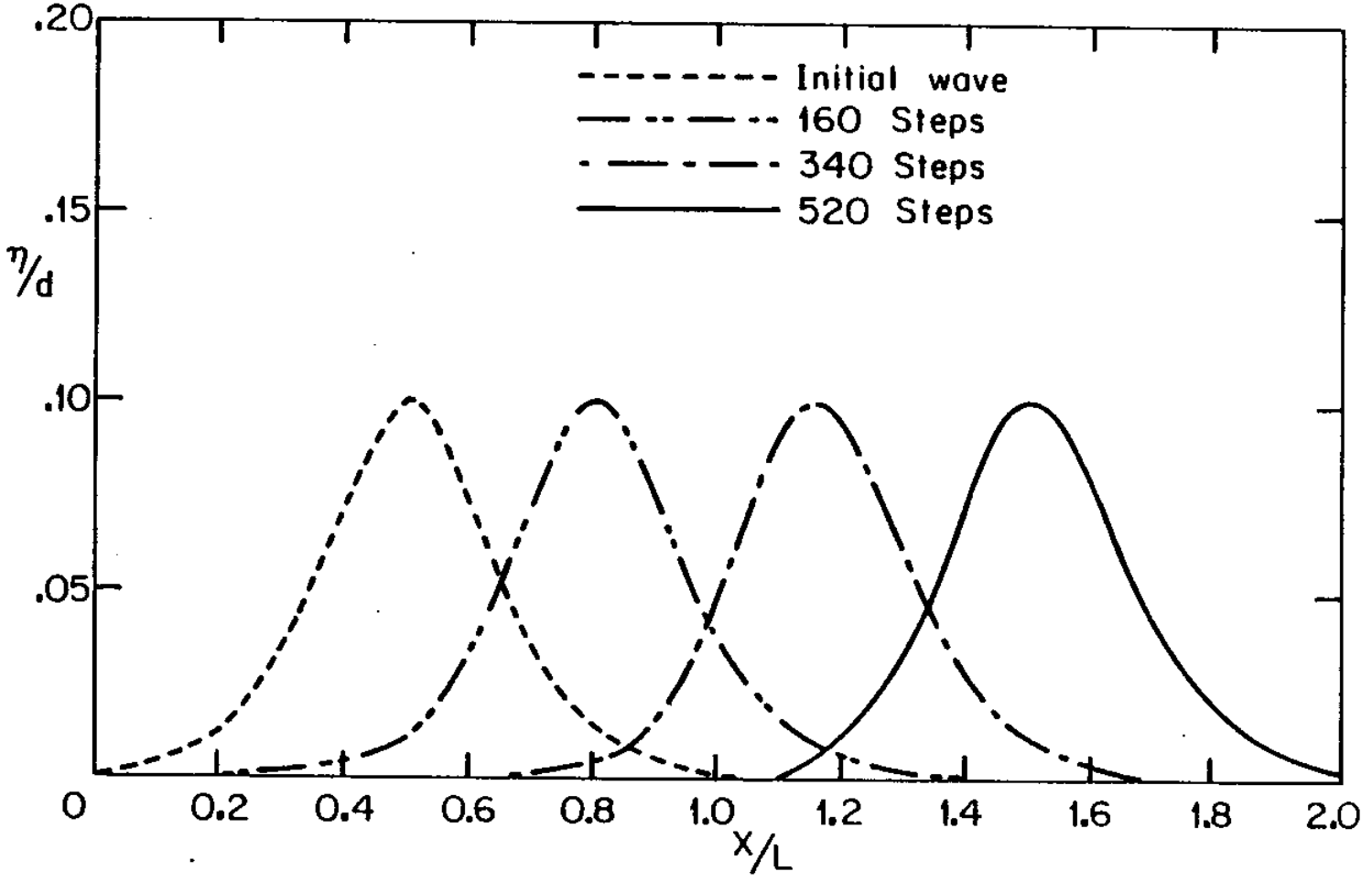

Fig. 6.11 Numerical results for the propagation of a solitary wave in a uniform water depth.

ratios of initial-to-final volumes and initial-to-final energies are found to be 1.0003 and 0.9999, respectively, which show errors in the volume and energy ratios are negligible.

As was pointed out, the time increment, Δt, has to be reduced to a certain value for the convergence of the algorithm. The value of $\Delta t = 0.005$ was found for the test model. This implies that a substantial computational work is needed for propagation of a wave for large times, since each time step involves the solution of the algebraic system of equations resulting from global form of (4.14).

As was previously discussed in Chapter 4, the multi-grid algorithm be used very effectively in the present problem to speed the convergence time by several orders of magnitude.

6.4 Solitary Waves Striking the Platform

In this section, the sequence of the wave impact on a horizontal platform is studied and described by the numerical model. In the test model a platform whose underside is above the still water level and has a relative soffit clearance of $S/d = 0.1$, is inserted in the flow region. An initial solitary wave of relative height

of H/d = 0.15 propagates through the still water depth d = 30.48 cm, and reaches the horizontal platform mounted above the still water level (Fig. 6.12). To view in sequence the progress of the wave impact as it approaches, strikes, and propagates beneath the platform, the numerical results are presented for several instants in Figs. 6.12 through 6.16. Each figure represents the variation of normalized surface profile with normalized distance. These results are obtained for instants of 0, 160 Δt, 240 Δt, 400 Δt, and 640 Δt. In Fig. 6.12, the undisturbed wave propagates shoreward approaching the platform. In Fig. 6.13, the wavefront propagates beneath the platform and the vertical front face of the platform causes the wave to run upward. As the wave advances further, the height of the wave run up created by the platform grows higher (Fig. 6.14). As it appears in this figure, the presence of the platform causes a sudden jump in the solution which is probably due to rapid variations of the equation coefficients. Figure 6.15 shows a reflected wave is to be formed at the front edge of the platform, while the symptoms of the sudden jump in the solution are amplified. In Fig. 6.16, the surface profile exhibits a severe oscillation in the front face of the platform which causes the algorithm to stop after a few

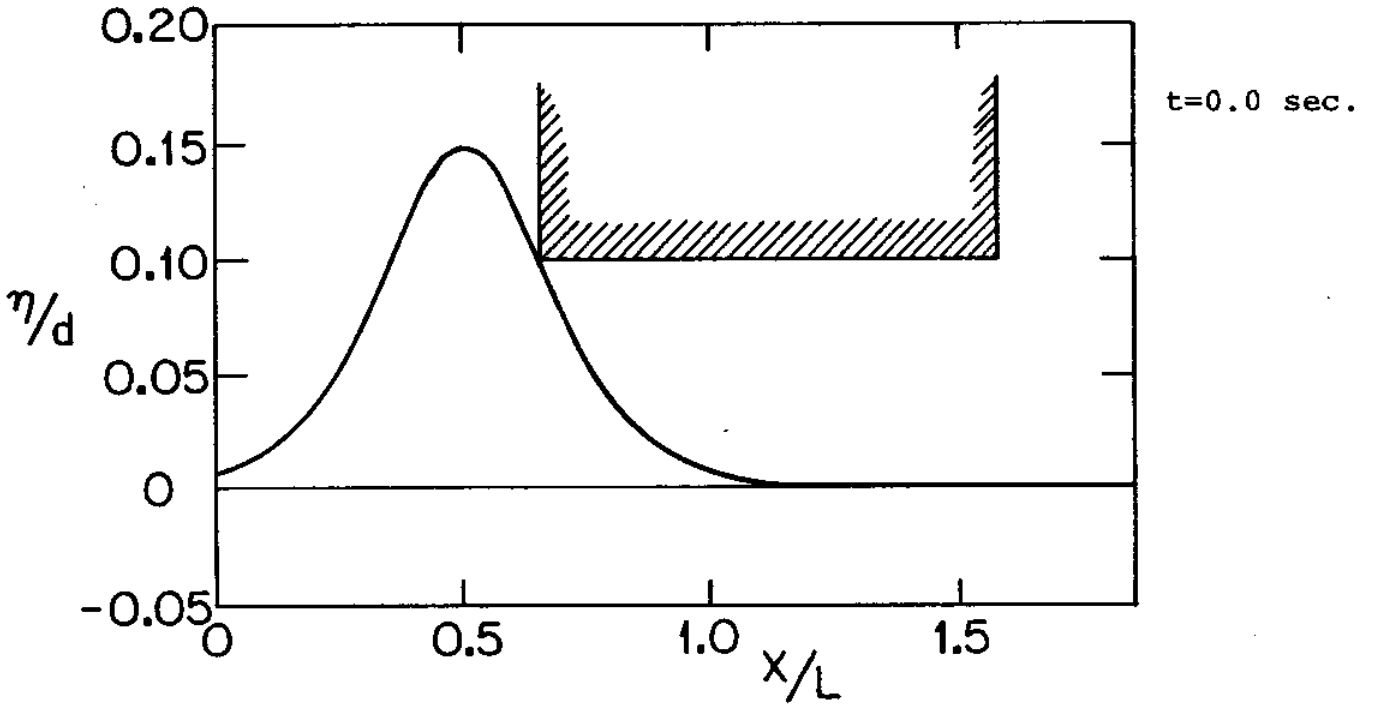

Fig. 6.12 Wave striking the platform, d = 30.48 cm., H/d = 0.15, S/d = 0.1.

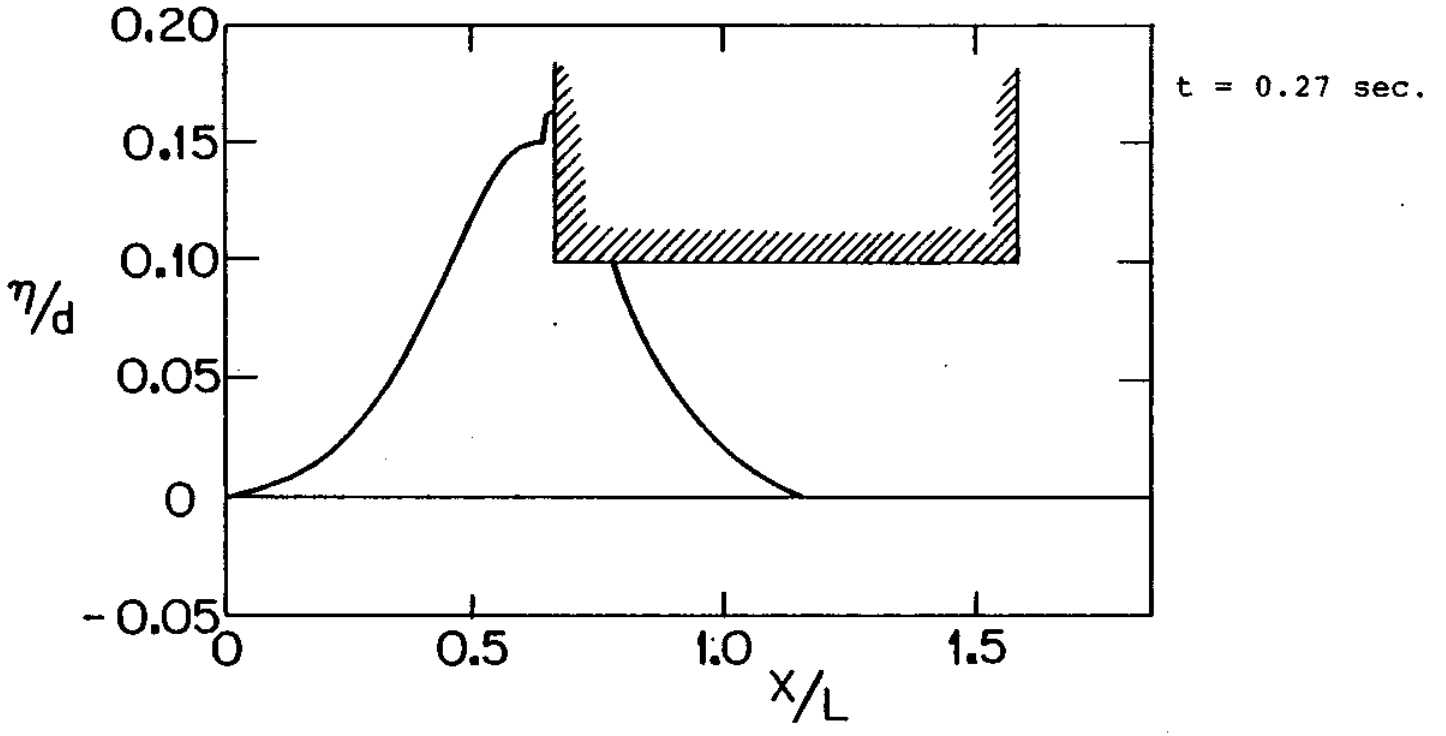

Fig. 6.13 Wave striking the platform, d = 30.48 cm., H/d = 0.15, S/d = 0.1, ν = 0.

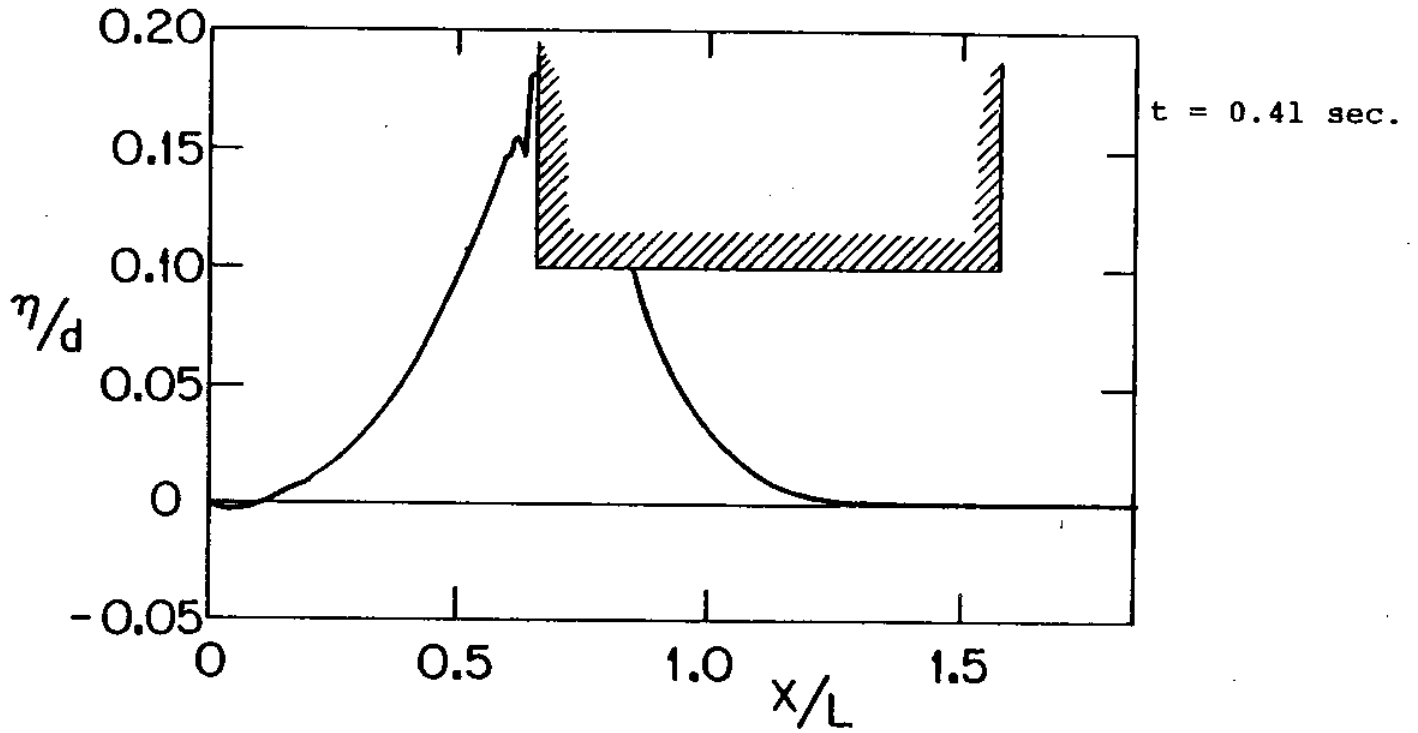

Fig. 6.14 Wave striking the platform, d = 30.48 cm., S/d = 0.1, H/d = 0.15, ν = 0.0.

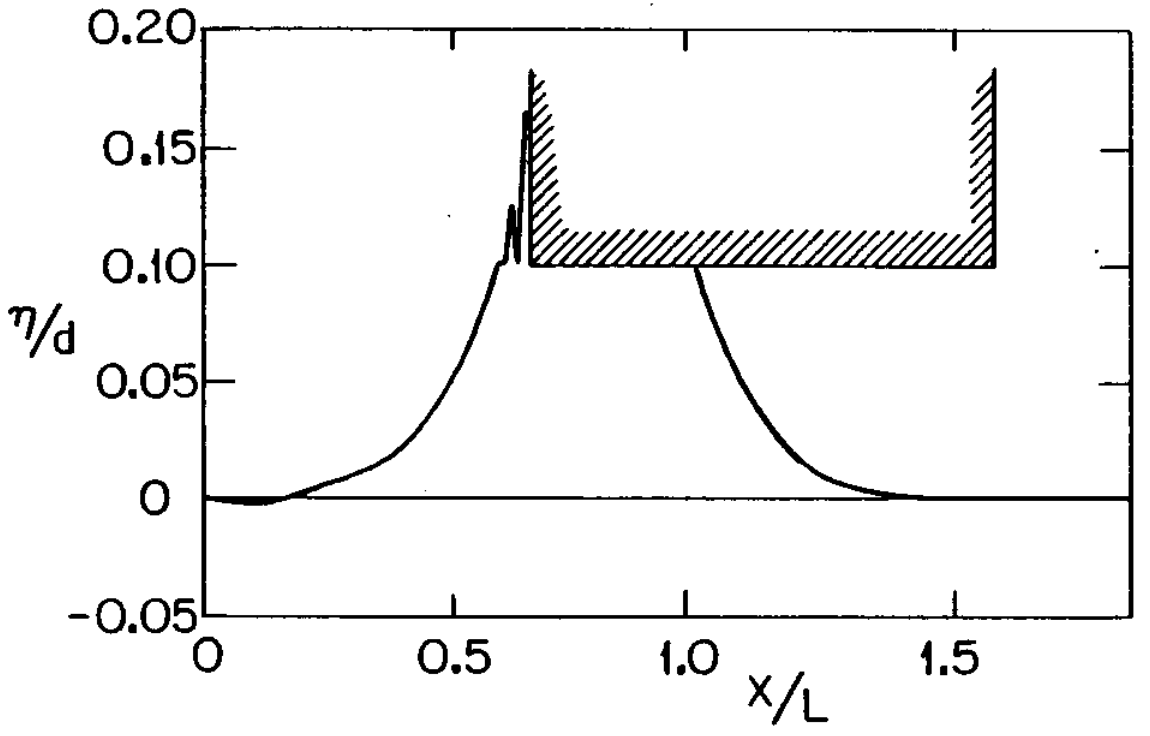

Fig. 6.15 Wave striking the platform, d = 30.48 cm., S/d = 0.1, H/d = 0.15, ν = 0.0.

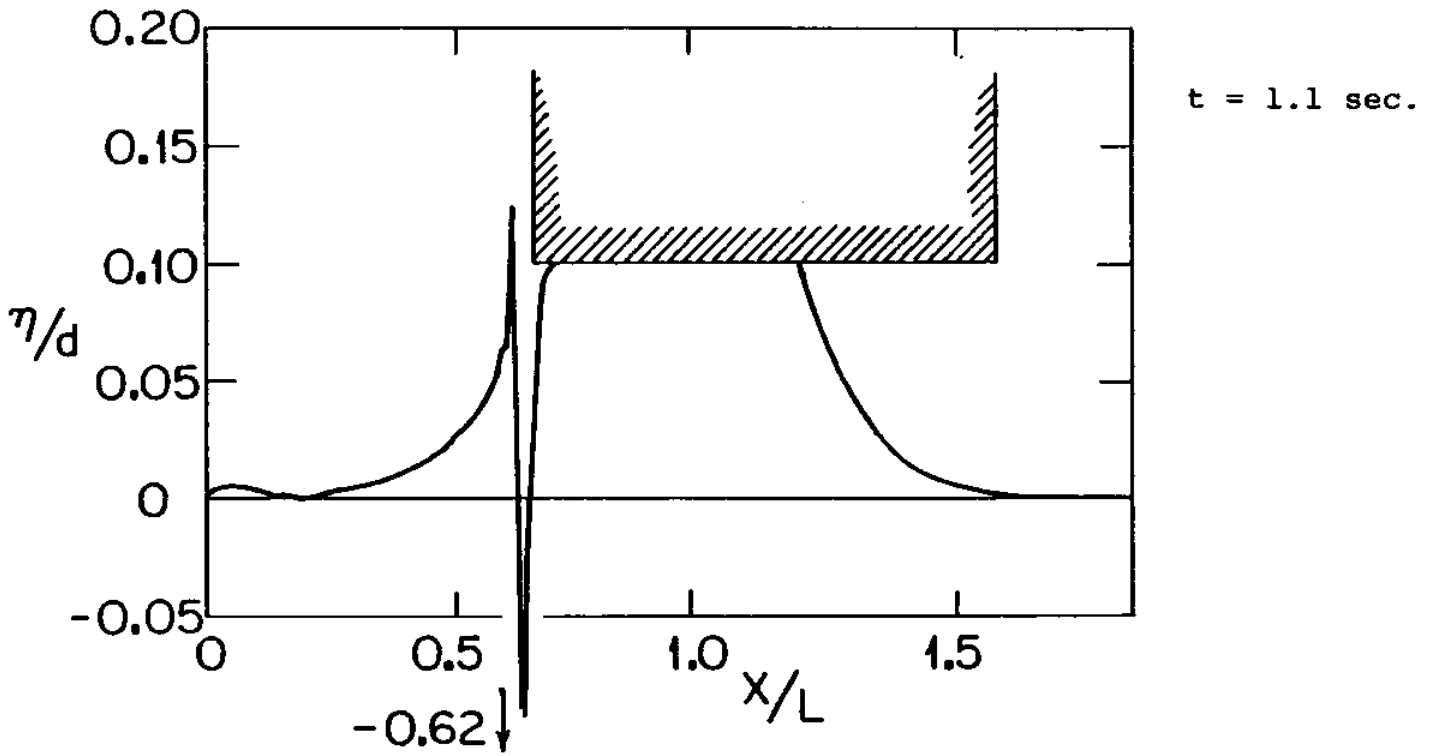

Fig. 6.16 Wave striking the platform, d = 30.48 cm., S/d = 0.1, H/d = 0.15, ν = 0.0.

more time steps. As can be seen from these results, the symptoms of instability such as the severe oscillations is only presented in the front region of the platform. As indicated in Chapter 4, similar problems have been investigated for treatment of shock waves in gas dynamics and interfaces separating two different fluids by several authors using the artificial viscosity effect. In our problem, an artificial viscosity term as $h_{,xx}$ is included in the kinematic free surface equation. this viscosity term is effective for the region where $|h_{,xx}|$ is large. To demonstrate the usefulness of this method, the same test model is used with inclusion of the artificial viscosity term. The viscosity parameter is found by numerical experiments. This is performed by increasing the numerical value of the artificial viscosity until the change in the solution profile in front of the platforms becomes insignificant. For the test model, the viscosity parameter of $\nu = 0.0065$ [m^2/sec] was found to have a significant effect in damping the abnormal free surface oscillations without altering the solutions in the region other than the front face of the platform. The numerical results of water surface profile for different time are presented in Figs. 6.17 through 6.21. In Fig. 6.17, the wave front propagates beneath the platform with much less

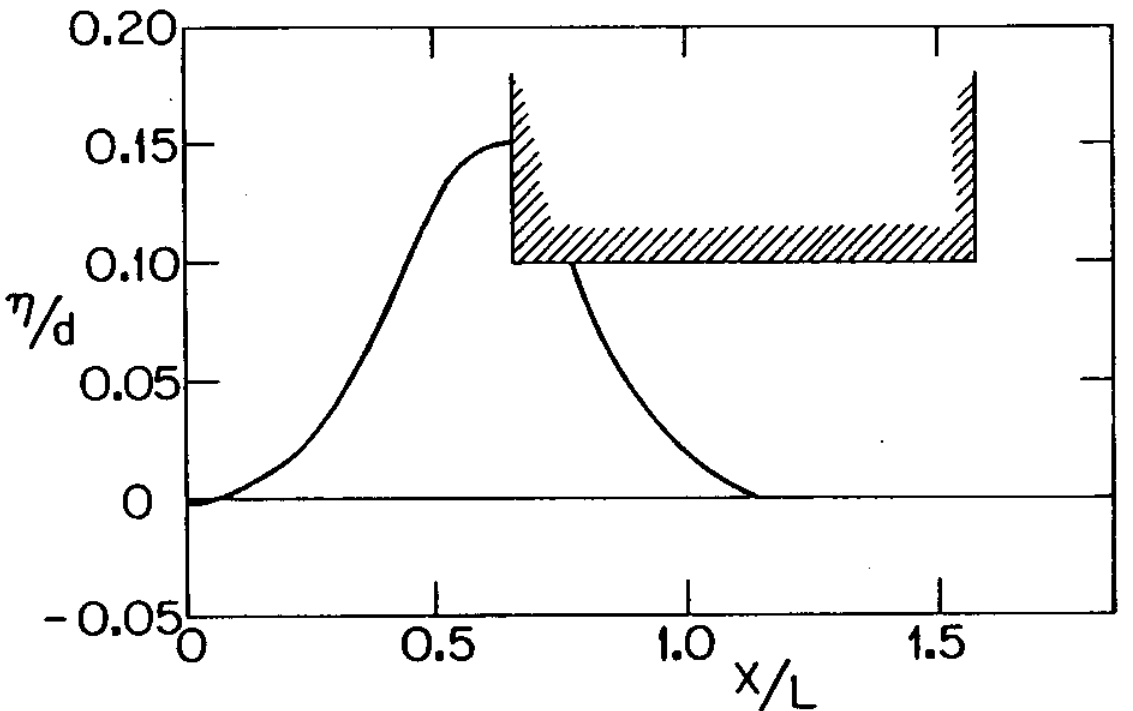

Fig. 6.17 Wave striking the platform, d = 30.48 cm., H/d = 0.15, S/d = 0.1, ν = 0.0065 [m^2/sec].

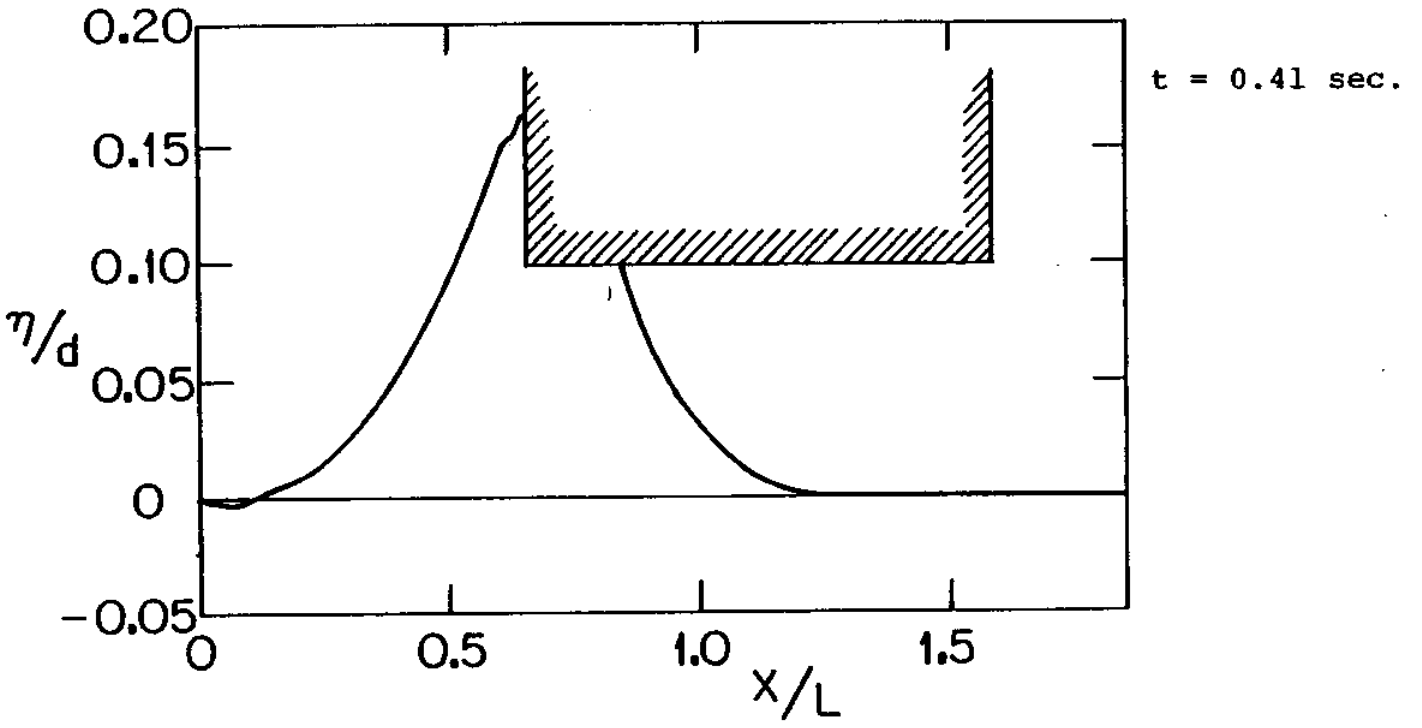

Fig. 6.18 Wave striking the platform, d = 30.48 cm., H/d = 0.15, S/d = 0.1, ν = 0.0065 [m^2/sec].

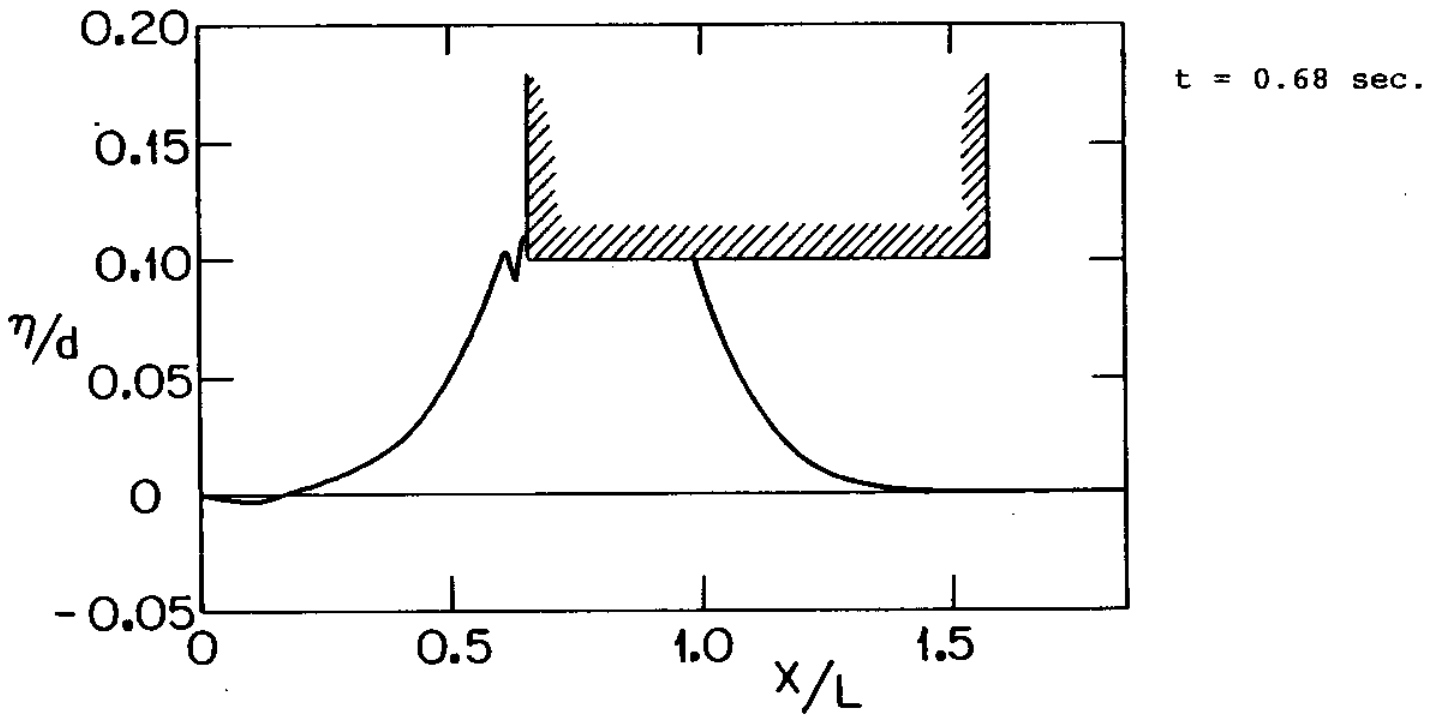

Fig. 6.19 Wave striking the platform, d = 30.48 cm., H/d - 0.15, S/d = 0.1, ν = 0.0065 $[m^2/sec]$.

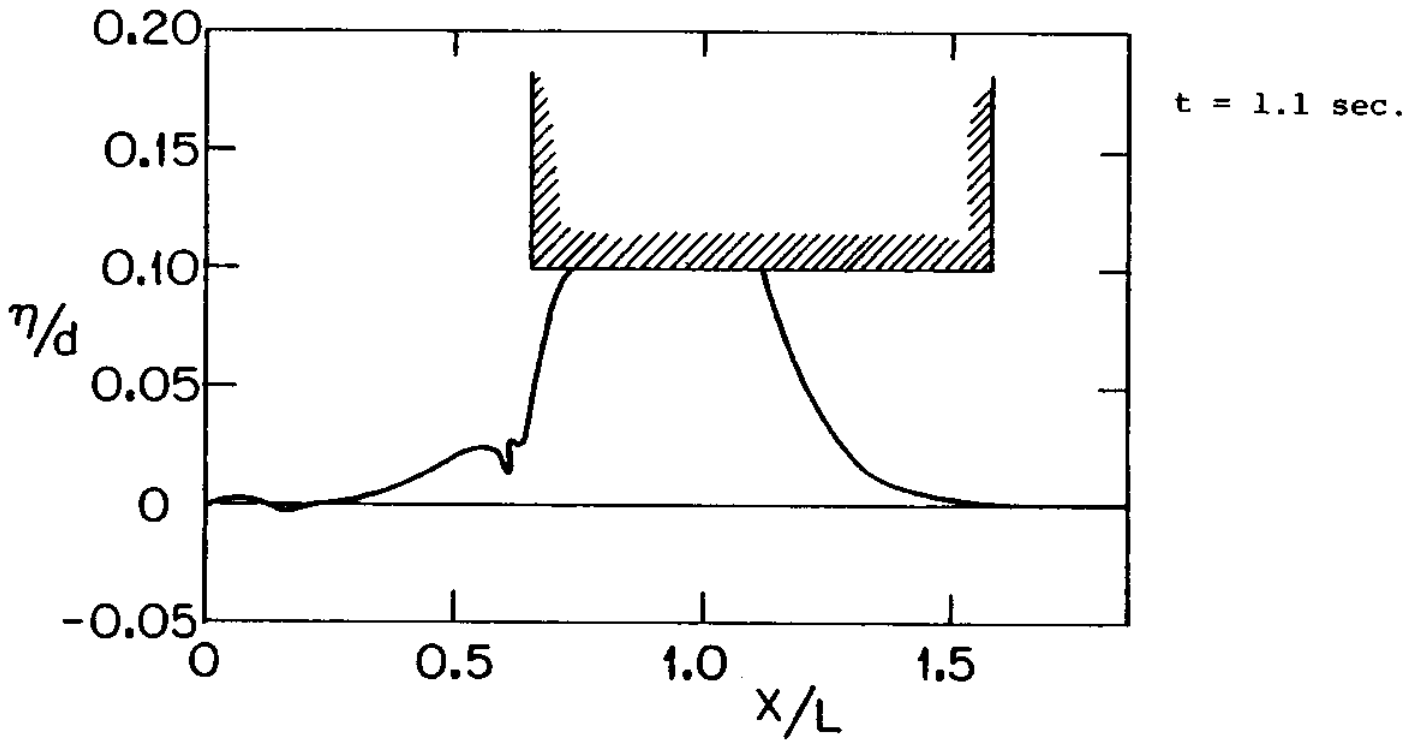

Fig. 6.20 Wave striking the platform, d = 30.48 cm., H/d = 0.15, S/d = 0.1, ν = 0.0065 [m^2/sec].

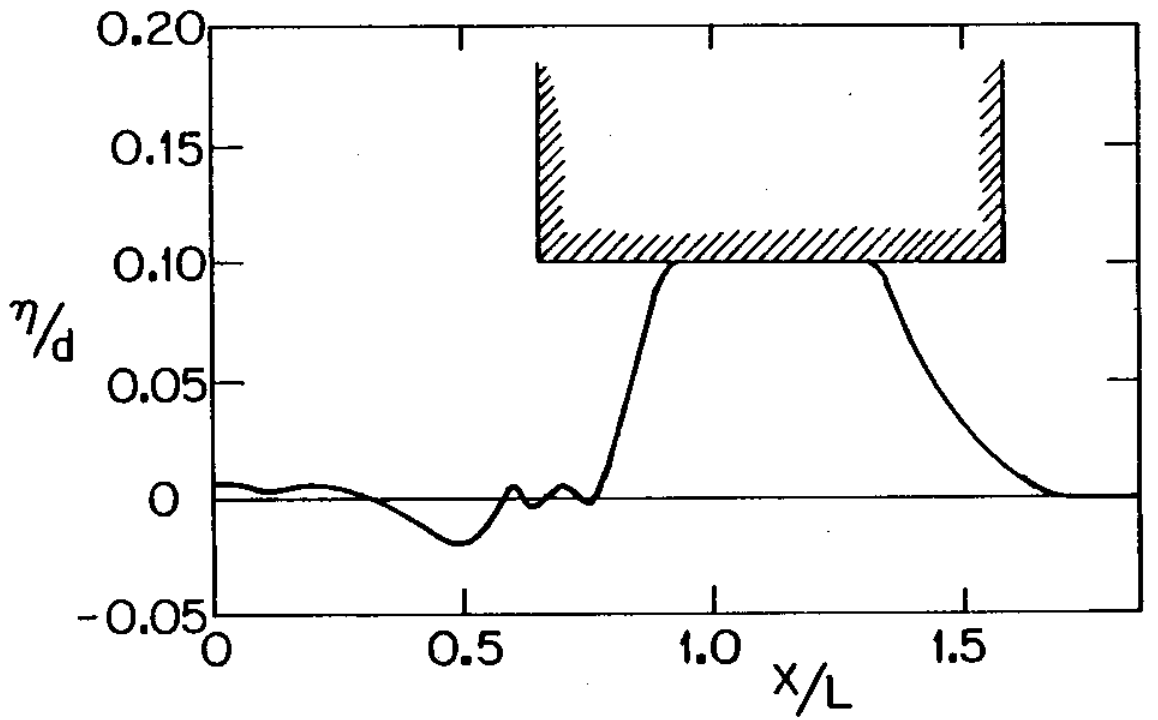

Fig. 6.21 Wave striking the platform, d = 30.48 cm., H/d = 0.15, S/d = 0.1, ν = 0.0065 [m^2/sec].

run up than in Fig. 6.13. As the wave propagates further, a moderate size of wave run up is being developed (Fig. 6.18). As the wave front continued to propagate beneath and in contact with the platform, the height of the wave run up grows no taller but descends to form part of a reflected wave train (Fig. 6.19). In Fig. 6.20, the surface profile descends from the seaward edge of the platform and the reflected wave continues to propagate away from the platform. In Fig. 6.21, the wave propagates beneath and in contact with the platform while the reflected wave train is fully developed and propagates seaward.

6.5 Velocity Field Beneath the Platform

As discussed in Chapter 5, the Laser-Doppler velocimetry technique was adapted to measure the velocity components beneath the platform as the wave strikes. The LDV was used to make two-dimensional, instantaneous measurements of water particle velocity at different depths and locations along the platform. The advantages of the Laser-Doppler velocimetry technique have been mentioned previously. The major difficulty encountered in this study was the air entrainment in the fluid region especially near the surface and near the leading edge of

the platform which interfered in LDV measurement. The air entrainment is caused by the incident wave when it strikes the platform. At this instant, the vertical front face of the platform causes the fluid to shoot upwards and air being entrained in the fluid as the wave continues to propagate and grow more turbulent. The air entrained in the fluid causes multiple scattering of the particles passing simultaneously through or sufficiently near the laser beams focal volume. The velocimetry events generated in these instances consist of a great deal of noises than those generated at other times. An even more severe problem encountered when interpreting the vertical velocities. The vertical velocity profile seemed to be varying rapidly and therefore resulting in irregular Doppler burst signals. These noises make the true picture of the vertical velocity time-history very difficult to interpret as well as many spots of missing data.

Several experimental runs were conducted to obtain the depthwise water particle velocities as a means of comparison. As mentioned earlier, the LDV is an instrument which can be used to measure velocities only at one point at a time. Therefore, it is necessary to repeat the experiments relocating the LDV for each measurement while checking the reproducibility of the wave generation

system. To minimize the effects of spume and air entrainment, wave of modest amplitudes were used. The measurement of velocities near the surface and the leading edge of the platform was usually with loss of data or noisy records for some of the cases in spite of repetition of experiments for various cases. However, for data which were clear, comparisons with numerical results can be very fruitfully done.

In Figs. 6.22 through 6.25, time-history of the horizontal water particle velocities are presented for a platform with relative soffit clearance of S/d = 0.1. In each figure, the measured water particle velocity is presented along with the particle velocity time-history obtained from the numerical model. Figures 6.22 and 6.23 present the normalized horizontal velocity $U/\sqrt{gd}$ as a function of nondimensional time $t\sqrt{g/d}$, at a location x = 5.1 cm. and vertical positions of z/d = 1.0 and z/d = 0.5, respectively. In these figures z is measured upwards from the bed and x is measured from the leading edge (upstream edge) of the platform. Figures 6.24 and 6.25 show the variation of horizontal velocities at a location x = 48 cm. and vertical positions of z/d = 0.5, and z/d = 0.2. In all these figures, the velocity profile is followed by a trailing oscillation of relatively small

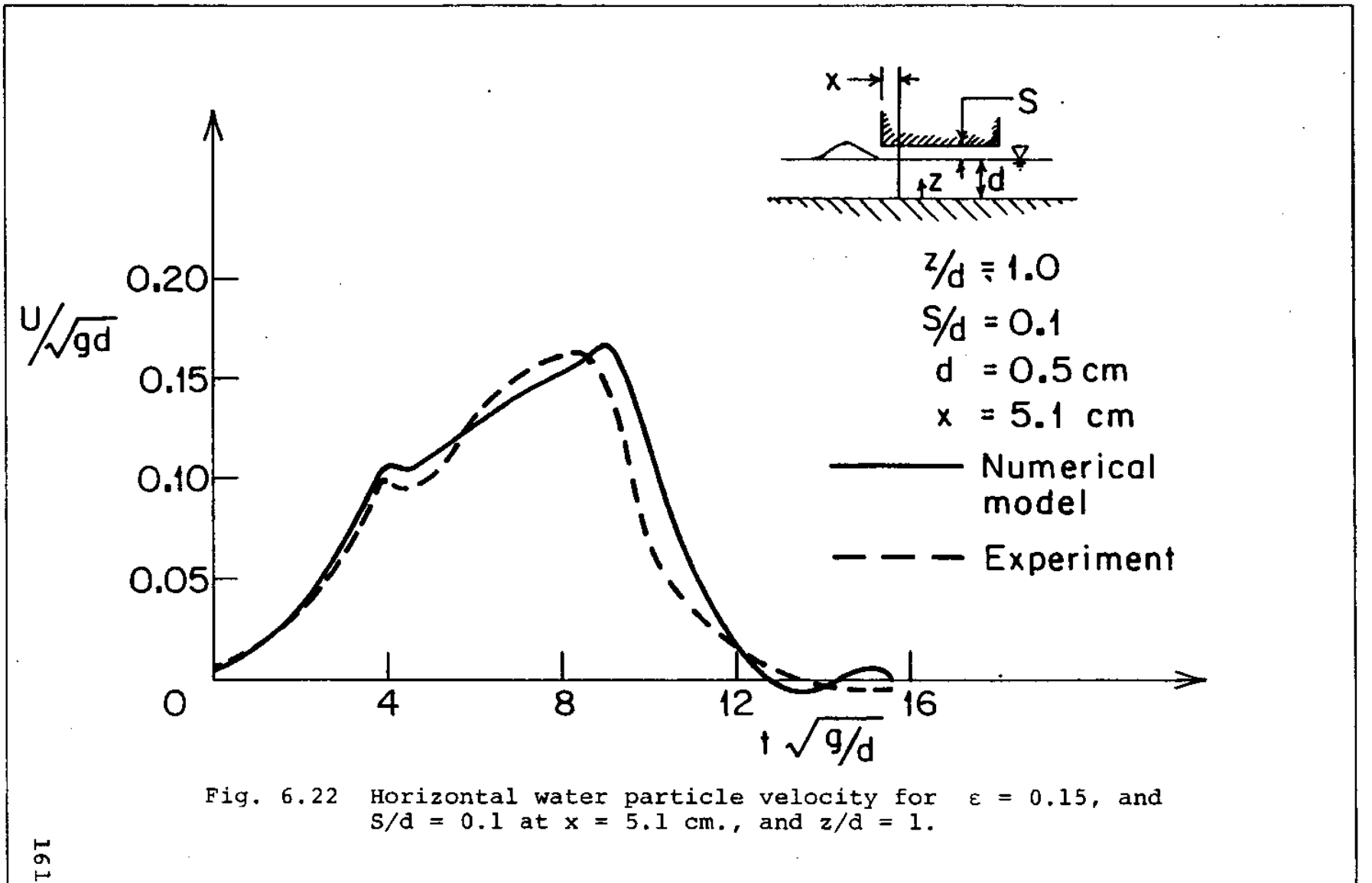

Fig. 6.22 Horizontal water particle velocity for $\varepsilon = 0.15$, and S/d = 0.1 at x = 5.1 cm., and z/d = 1.

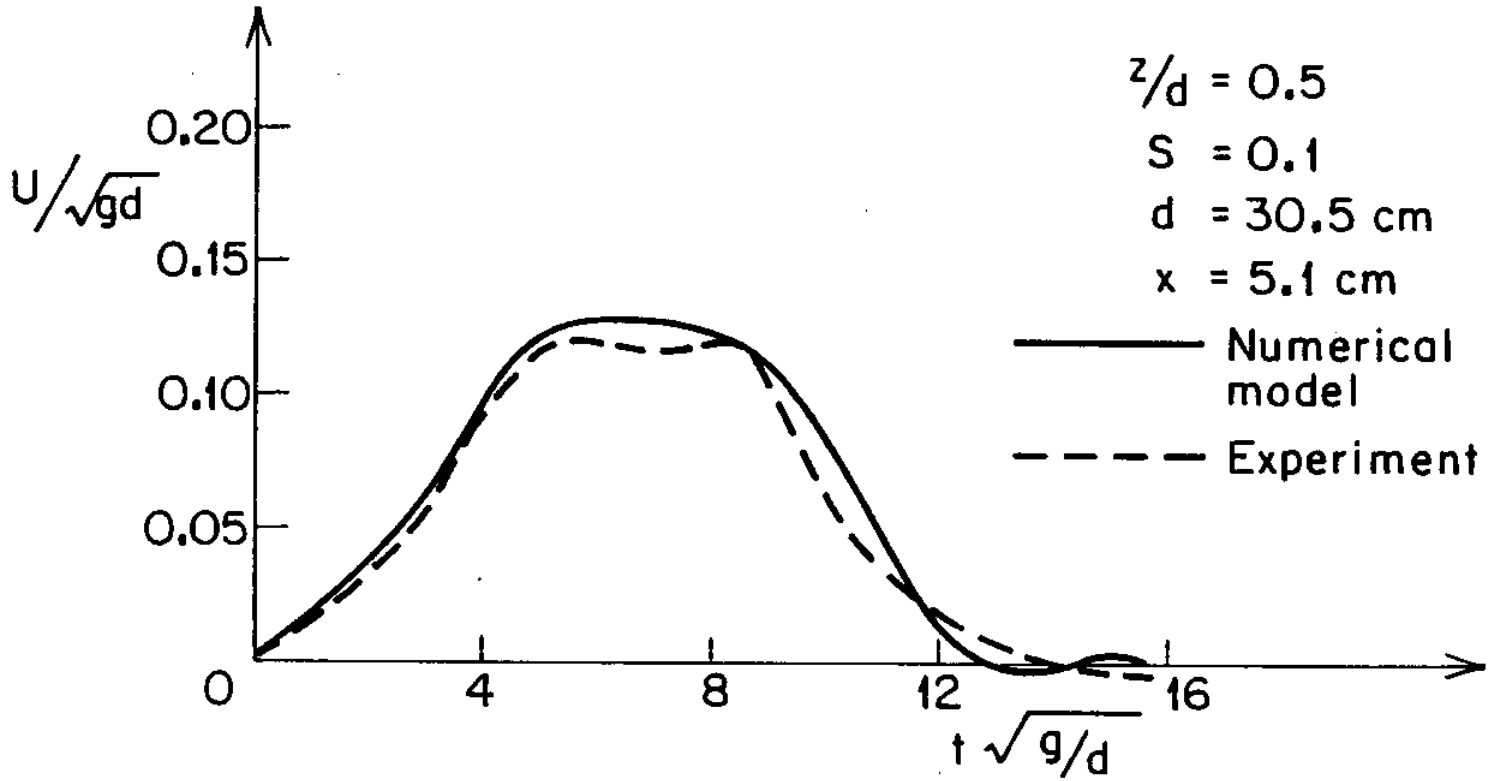

Fig. 6.23 Horizontal water particle velocity for $\varepsilon = 0.15$ and $S/d = 0.1$ at $x = 5.1$ cm., and $z/d = 0.5$.

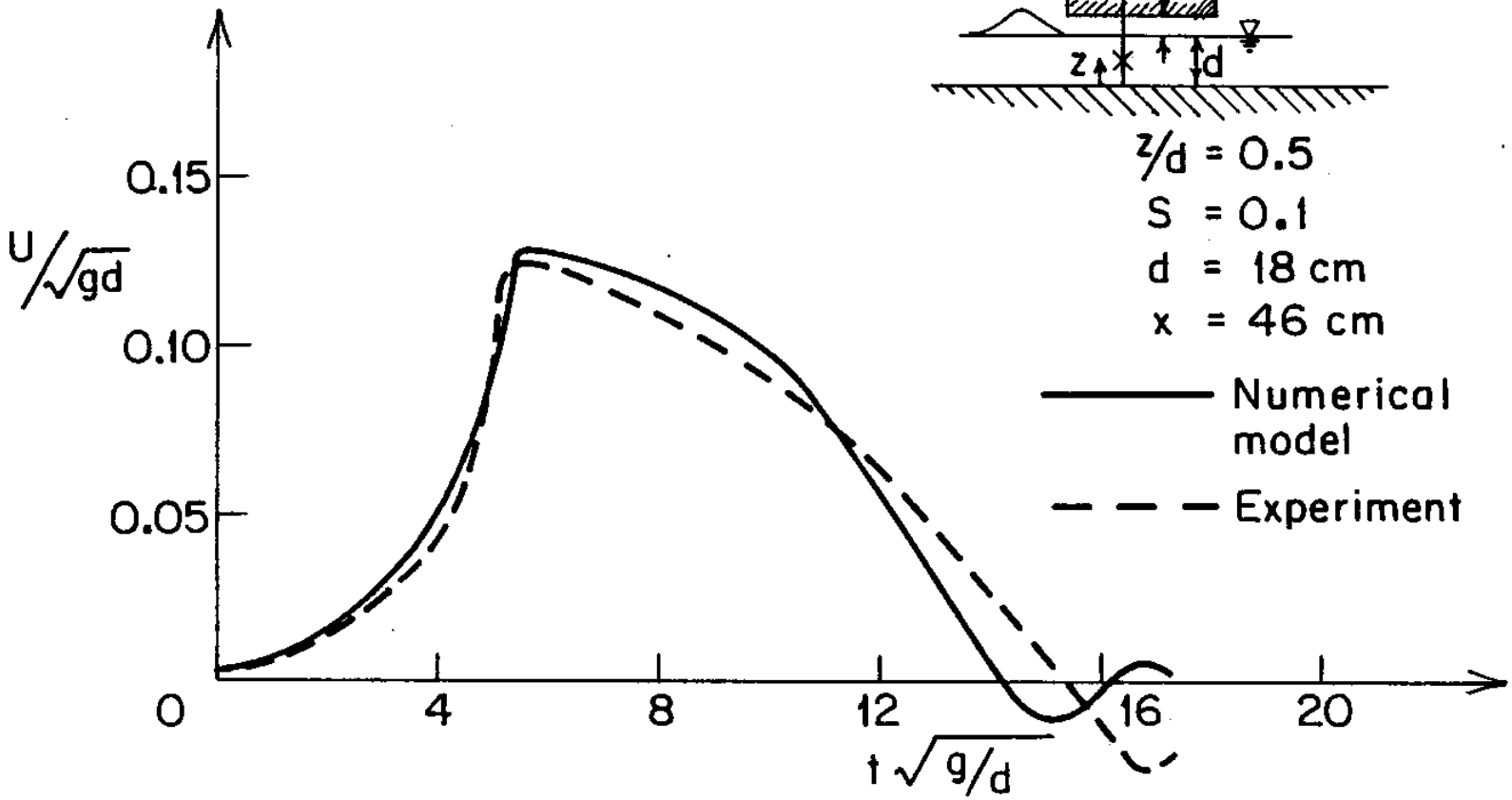

Fig. 6.24 Horizontal water particle velocity for ε = 0.15, S/d = 0.1 at x = 46 cm., and z/d = 0.5.

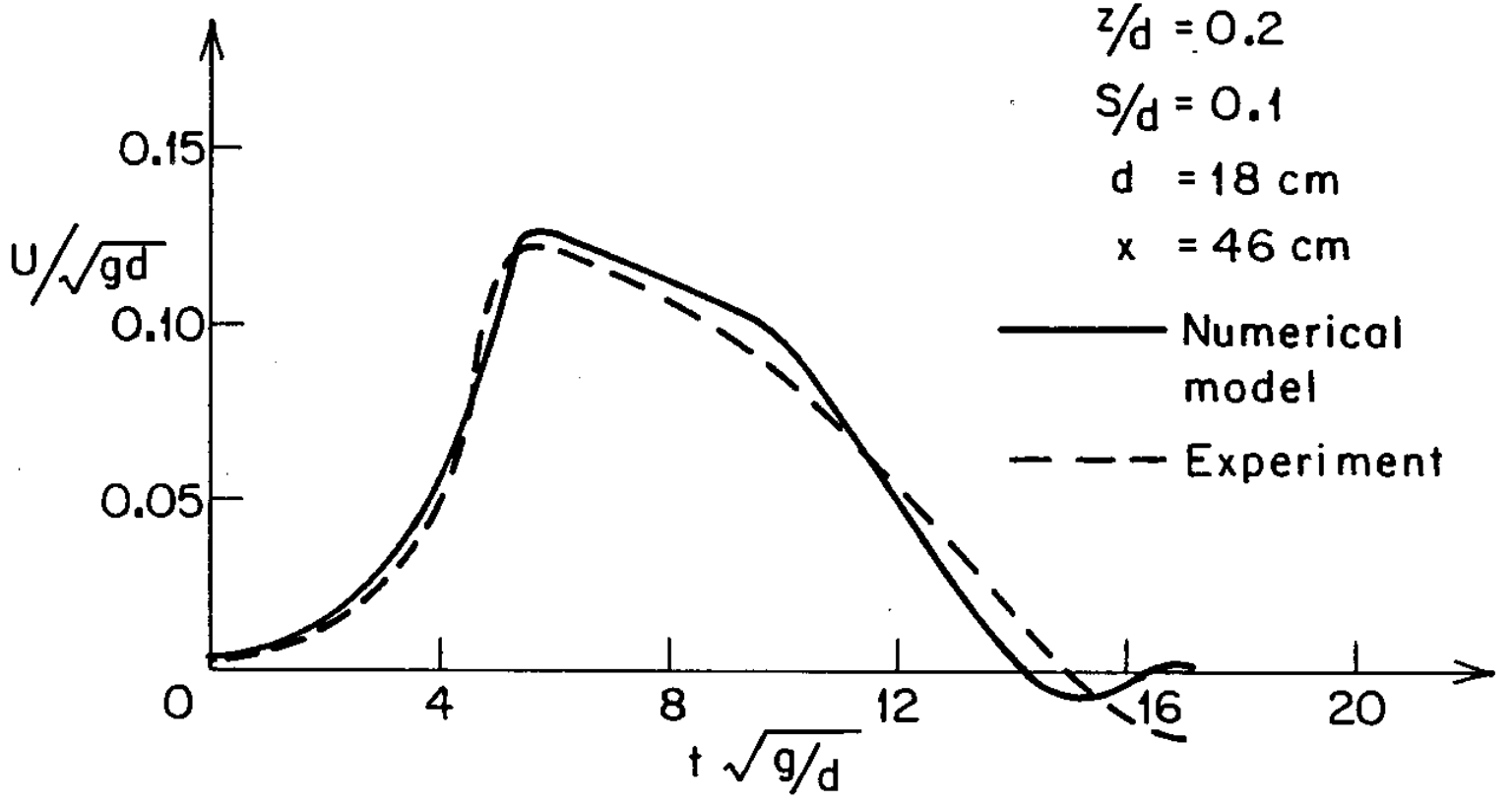

Fig. 6.25 Horizontal water particle velocity for ε = 0.15, S/d = 0.1 at x = 46 cm., and z/d = 0.2.

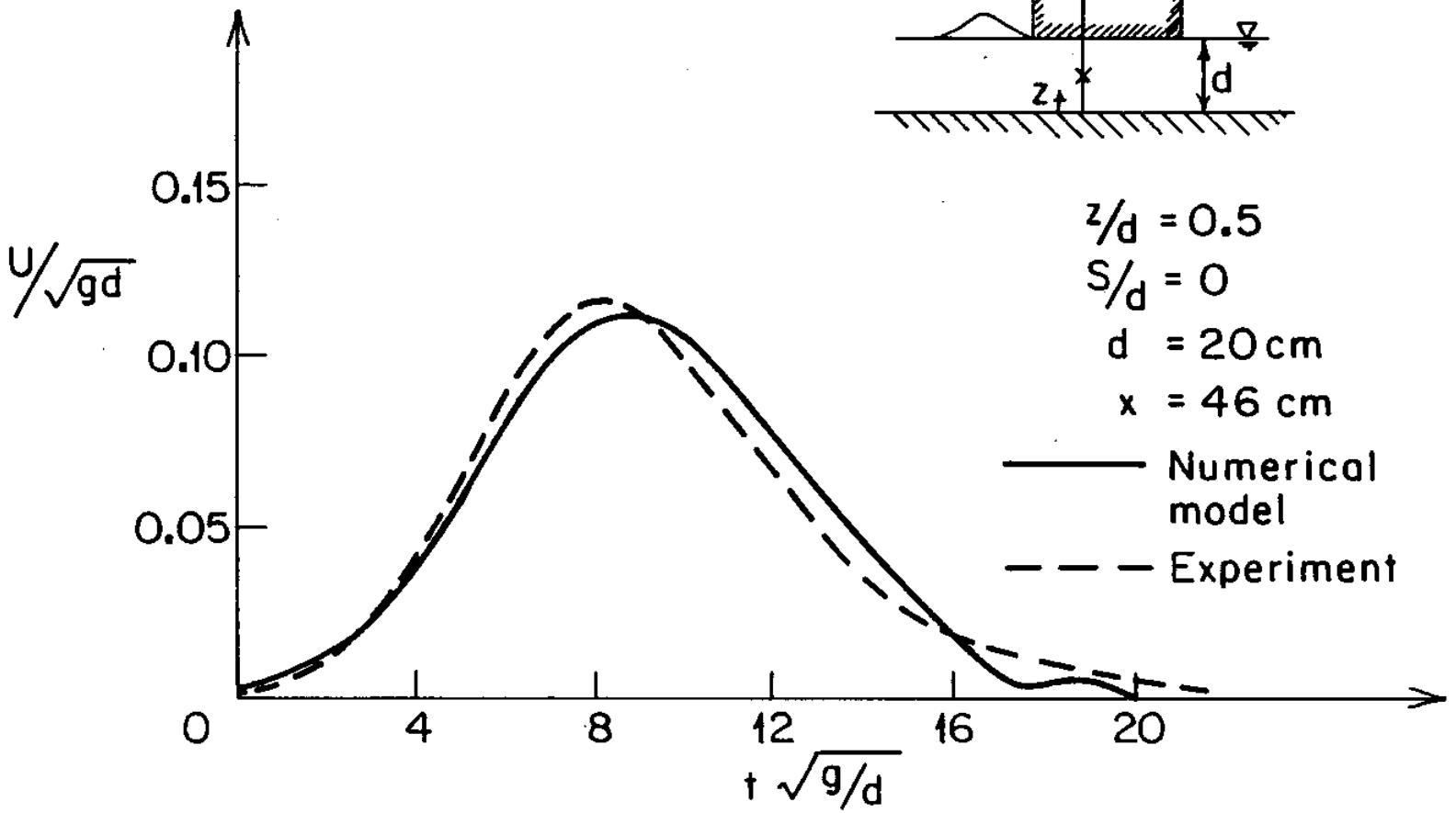

Fig. 6.26 Horizontal water particle velocity for ε = 0.15 and S/d =0 at x = 46 cm., and z/d = 0.5.

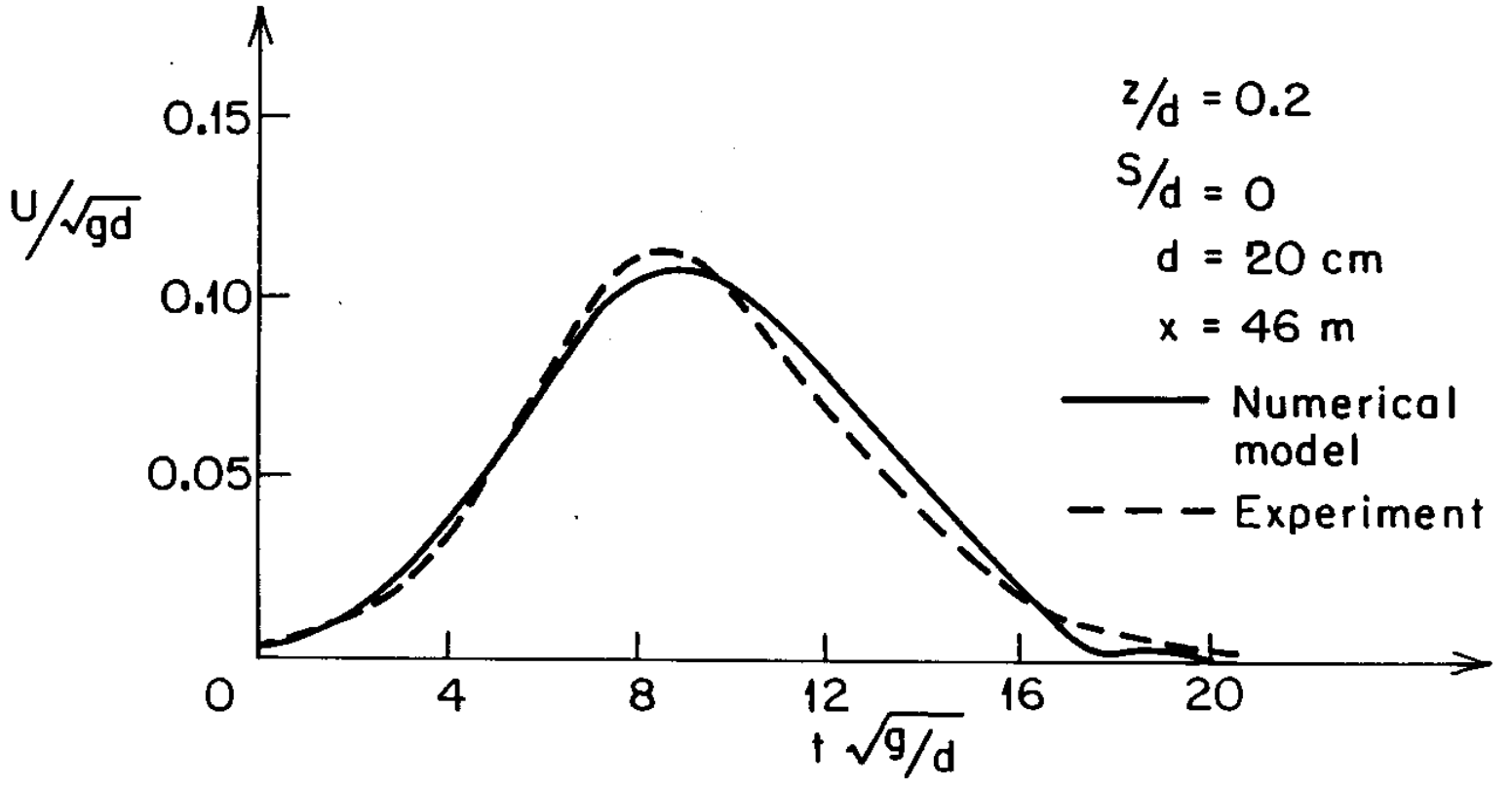

Fig. 6.27 Horizontal water particle velocity for $\varepsilon = 0.15$ and $S/d = 0$ at $x = 46$ cm., and $z/d = 0.2$.

magnitude. There are differences which are apparent in these comparisons. However, in general the differences are not large between the results obtained from the numerical model and those obtained by LDV measurements. Experimental runs where also conducted for a platform of zero soffit clearance S/d = 0.0, to evaluate how the velocity field is affected. Figures 6.26 and 6.27 represent the time-history of the horizontal velocity at a location x = 46 cm. and relative depths of z/d = 0.5, and z/d = 0.2, respectively. As can be seen from these figures, the horizontal velocity profile for the case of a platform with zero soffit clearance has similar trend as that of the horizontal velocity induced by an undisturbed solitary wave except with reduction of the amplitude and increasing the base width.

6.6 The Transmission of Solitary Waves Behind a Platform

In the experimental study of this work, in addition to measuring the incident wave and velocity field, the transmitted waves behind the platform were also recorded to define the time-history of the variation of the water surface elevation (the wave) at the downstream edge of the platform. This problem is of special importance to that of breakwater problem. In El Ghamry's experimental study

of wave uplift forces on a dock, the transmitted waves were recorded at a short distance behind the dock under the action of periodic incident waves. The dock used was constructed of thin aluminum plate with no front face to minimize reflections due to its thickness. The form of the transmitted waves was quite different from that of incident wave. They could not be approximated by sine waves and they were not completely irregular. The transmitted wave form was rather complicated, consisting of different harmonic components with different amplitudes and varying phase shifts. The change in phase shift seemed to be a function of time and was not a random variable.

In our work, the transmission of solitary waves behind a platform was considered for the case of a platform with a positive underside clearance and zero clearance. Since the propagation of the solitary wave to the downstream edge of th platform involves substantial computational steps in the two-dimensional numerical model, the transmitted waves were recorded at a short distance downstream of the platform for the purpose of comparison. In the experiment described in Chapter 5, a wave gage was placed about 10 cm. from the downstream edge of the platform to record the transmitted wave right

after the platform.

The first example of this comparison is shown in Fig. 6.28 where the relative wave amplitude is = 0.13 and the relative soffit clearance is S/d = 0.1. In this figure, the transmitted wave profile is normalized by the water depth and is expressed as a function of the nondimensional time, $t\sqrt{g/d}$. As can be seen from this figure, the amplitude of the transmitted wave is less than incident wave and the wave appears to be separating into individual waves of smaller amplitude. The oscillatory waves of small amplitudes and short periods are observed to be trailing the transmitted wave. The agreement between the experimental and numerical results is quite good considering the long computational steps involved in the computational procedure.

It was of interest to investigate the effect of the platform of zero soffit clearance on an incident solitary wave. In Fig. 6.29, the transmitted wave profile is expressed as a function of nondimensional time for the relative wave amplitude of ε = 0.15, and S/d = 0.0. It is seen from this figure that for the case of zero soffit clearance the transmitted wave profile consists of a single wave which appears to be similar to a solitary wave

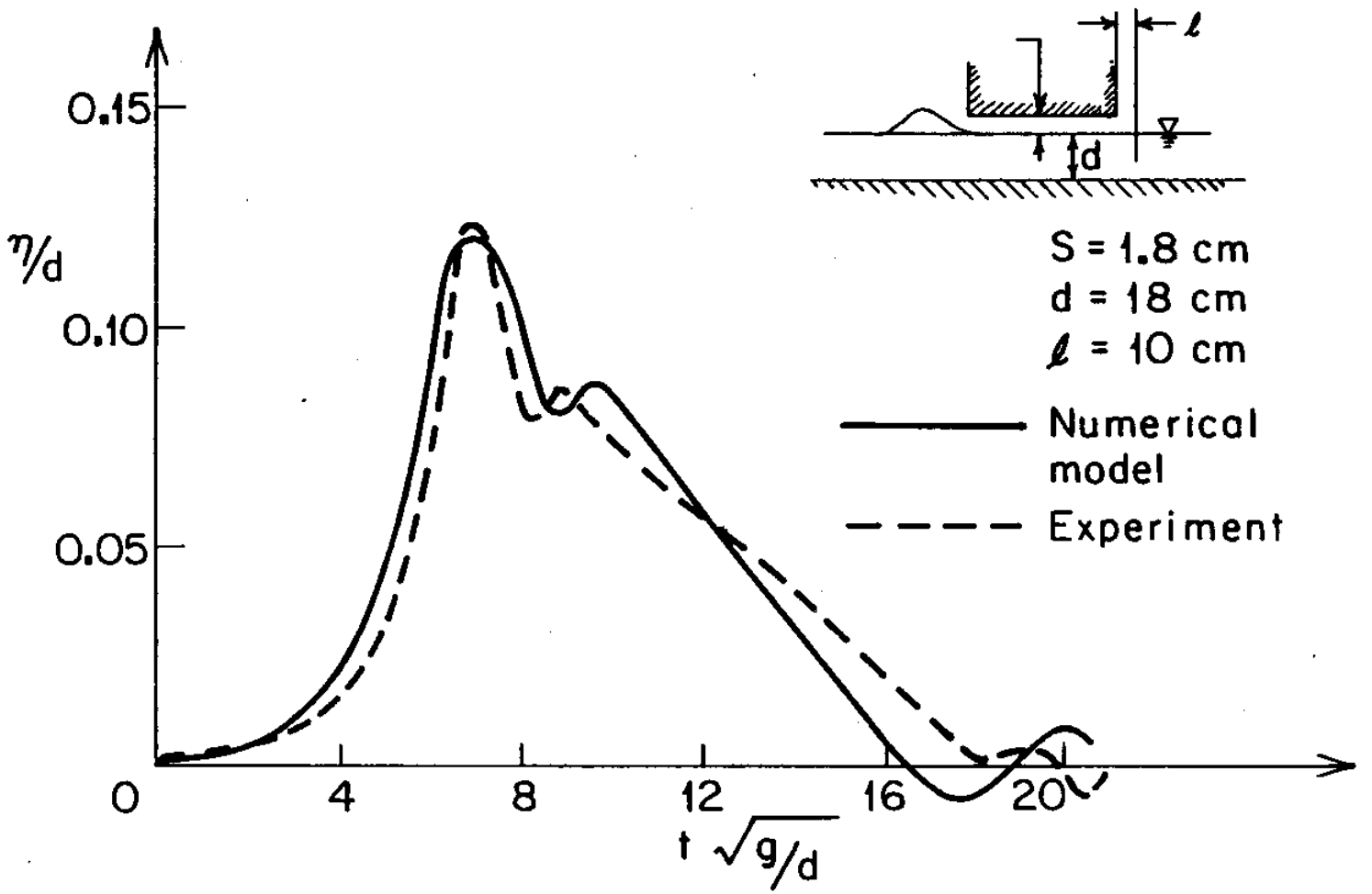

Fig. 6.28 Transmitted wave for $\varepsilon = 0.13$ and $S/d = 0.1$.

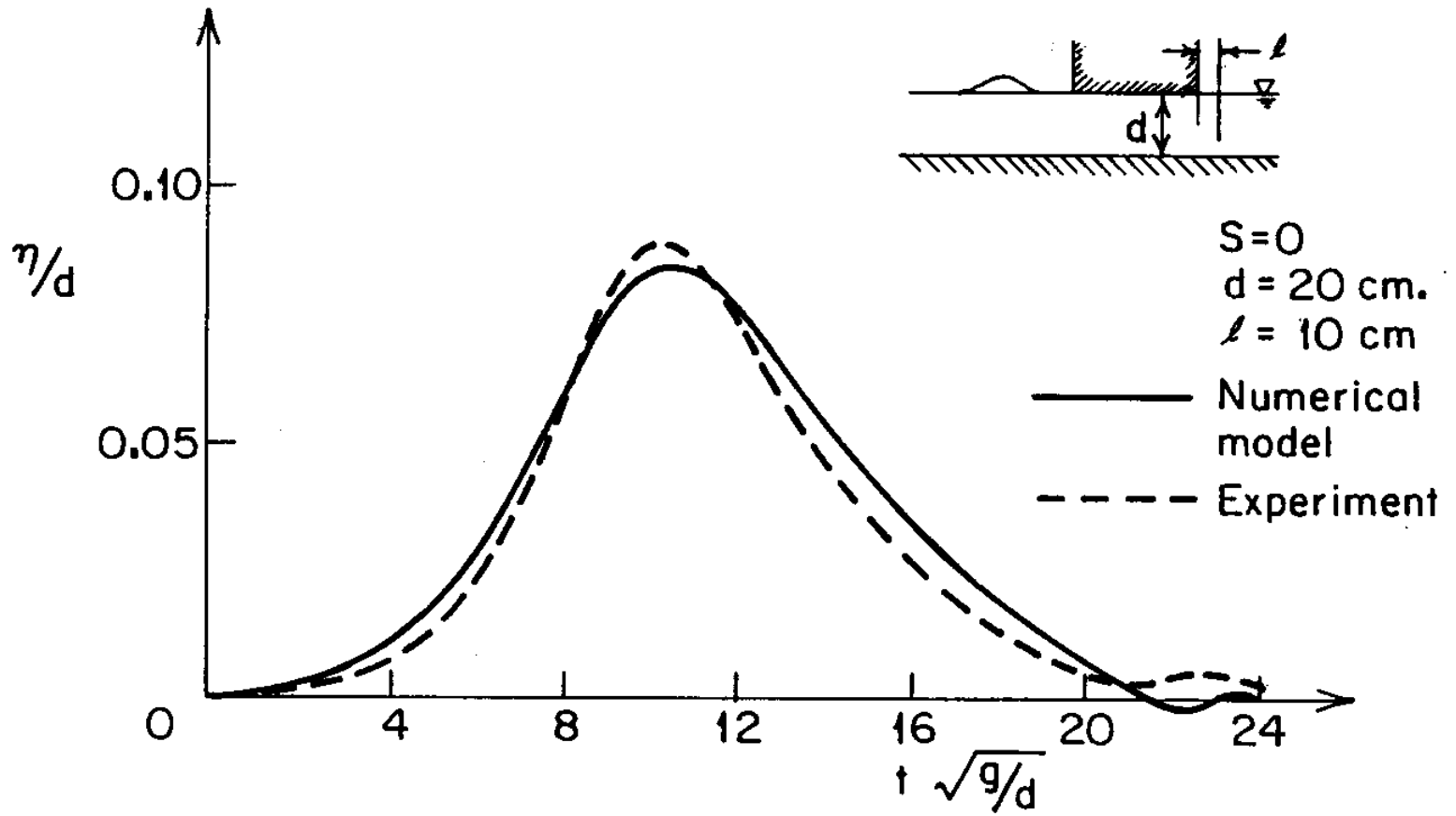

Fig. 6.29 Transmitted wave for $\varepsilon = 0.15$ and $S/d = 0$.

followed by a relatively small amplitude oscillatory waves. This is interesting to note that even with the presence of the platform in the flow field, the transmitted wave is not severely distorted but it is apparently similar to a symmetrical solitary wave profile. The transmitted wave profile indicates significant reduction of the maximum wave amplitude of the incident wave (the amplitude is decreased by about 30%). This is certainly related to the fact that some of the wave energy is reflected at the upstream of the platform.

6.7 Wave Uplift Pressures on the Platform

In this section the details of the uplift wave pressures due to the boundary condition imposed on the velocity and acceleration field by the presence of the platform is studied. As was previously mentioned experimental studies by several investigators including French (1969) have confirmed the existence of the wave uplift pressures as the incident waves strikes and advances beneath and in contact with a horizontal platform. The typical pressure profile is usually characterized by a sharp impact caused by initial contact of the wave with the platform followed by a slowly varying pressure which is first positive and then negative when

the wave leaves the platform.

In the present analysis the wave uplift pressure can be determined once the velocity potential field is computed from the numerical model. Using the Bernoulli equation, the pressure head can be expressed as a

$$\frac{P}{\gamma} = -\frac{1}{g}\phi_{,t} - \frac{1}{2g}(\phi_{,x}^2 + \phi_{,y}^2) - S$$

where the soffit clearance, S, is the distance measured from the still water depth to the underside of the platform. Thus, at any point along the platform the time-history of pressure can be computed having computed velocity potential as a function of time. To investigate the functional behavior of the uplift pressure, several cases were considered for different soffit clearances and different locations along the platform. For the purpose of comparison, the experimental results of wave uplift pressure performed by French (1969) are presented and discussed.

As was mentioned in Chapter 2, French (1969) conducted a two-dimensional laboratory study to investigate the wave uplift pressures on a horizontal and fixed platform when individually generated solitary waves strike and propagate beneath the platform. Pressure

transducers were mounted on the underside of the platform for the measurement of the induced pressure by the wave. There were some problems involved in the pressure measurements. The problem of spatial resolution due to the transducer size which was recognized during the preliminary test was later improved by using transducers of a smaller size but had not been completely solved. In spite of mounting the transducers in adaptors, they suffered a troublesome drift in zero-pressure output due to changes in temperature as the water contacted the platform. Another problem which arose in pressure measurement was a series of oscillation in output signal at approximately the point where the slowly-varying pressure profile passes from positive to negative region. A curve fitting method was employed in the region, before and after the regions of oscillation to indicate the time of zero pressure, separating region of positive and negative pressure. In our work, wave uplift pressures for the cases of moderate amplitude are computed and compared to that of French's experimental results. For consistency of comparison, the same geometrical and incident wave parameters are used. Due to inherent characteristic of the discrete numerical model, as the wave front advances beneath the platform, its contact at every new point

sustains an impulsive peak pressure which in turn affects the pressure at other points along the platform. To represent the mean value about which the computed pressure varied, an approximate envelope curve was fitted to each set of data.

In Figs. 6.30 through 6.33, the relative pressure head $P/\gamma d$ is expressed as a function of normalized time, $t\sqrt{g/d}$ for different wave amplitudes, soffit clearances, and locations along the platform. As can be seen, the pressure-time curves are characterized by a sudden rise to a peak followed by a rapid drop, and slowly-varying pressure which is first positive and then negative. The positive pressure is predicted at the advancing wave front where the rising water makes initial contact with the platform soffit. As the trough advances towards the point, the water falls below the equilibrium position. This drop on the water surface under the platform would create a vacuum in the space between the platform and the water surface. This process creates a suction force as a negative uplift. In these figures, at $t\sqrt{g/d} = 0$, the wave first makes the initial contact with the seaward edge of the platform. The differences between the computed pressures and measured pressures arise from the approximations employed in determination of the pressures.

As was mentioned before, due to severe oscillations in the pressure records from the experiment which occurred at the time of zero pressure, a curve was fitted to determine the approximate point of zero pressure. French (1969) predicted these oscillations as the wave of recession began to form at the seaward end of the platform. In reducing the slowly-varying pressure data from records, the sampling frequency was less than the oscillation frequency and therefore the oscillations do not appear clearly in experimental records. The problem of temperature shift is also a cause of discrepancy in these comparisons. As this figures show the time of zero-pressure, indicating the point that the wave is no longer in contact with the measurement point, indicates a drift comparing to that computed by the numerical model. Because of smoothing used in the determination of pressure profile from the numerical model, the process of changing pressure of negative to zero is not slowly-varying as it is in the experiment. But the duration of pressure indicated, reflects the time of contact of the wave with a given point on the platform.

Figures 6.30 and 6.31 show clearly that for a fixed platform condition such as soffit clearance, the duration of positive uplift pressure to duration of negative uplift

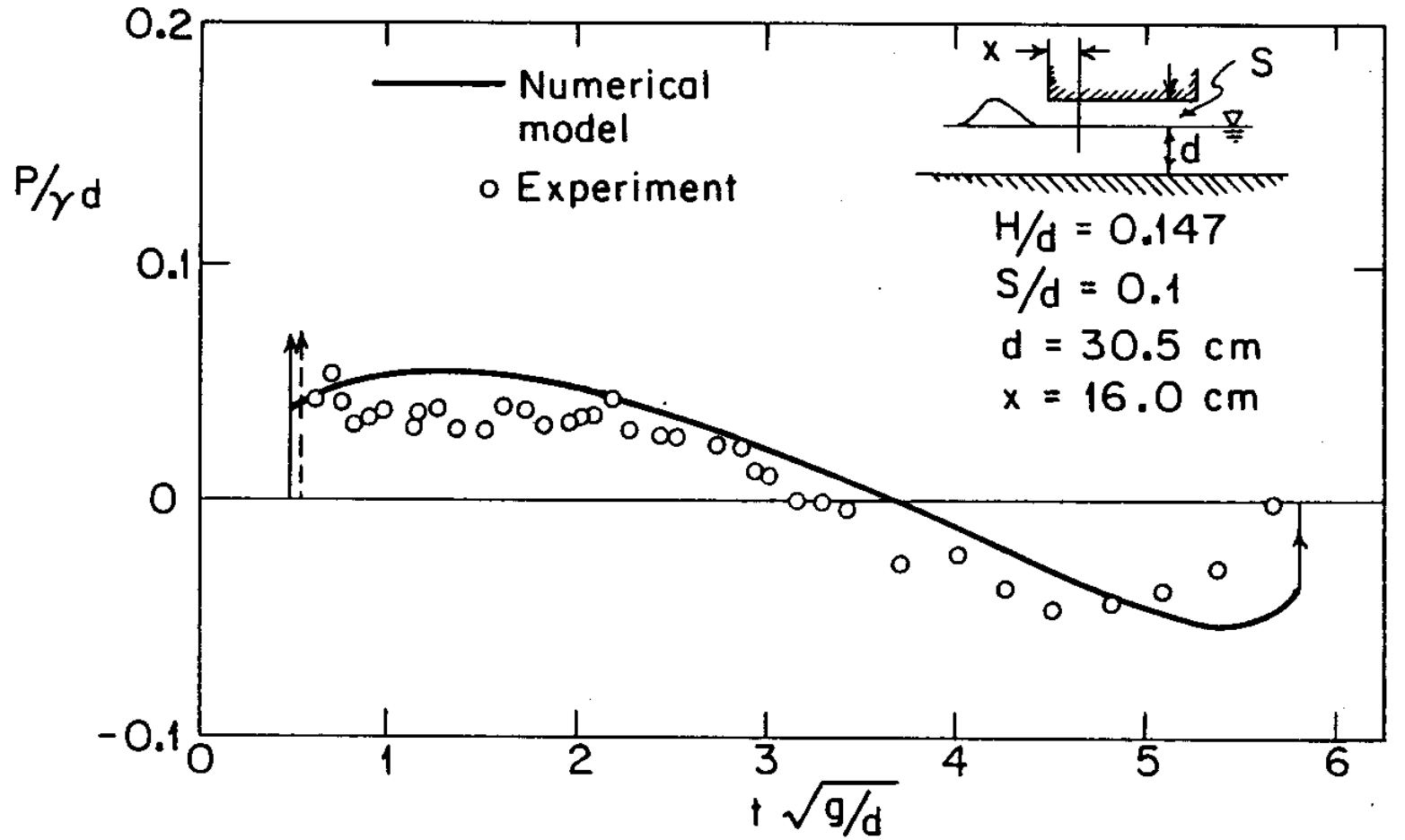

Fig. 6.30 Pressure as a function of time for ε = 0.147, and S/d = 0.1, at x/d = 0.522.

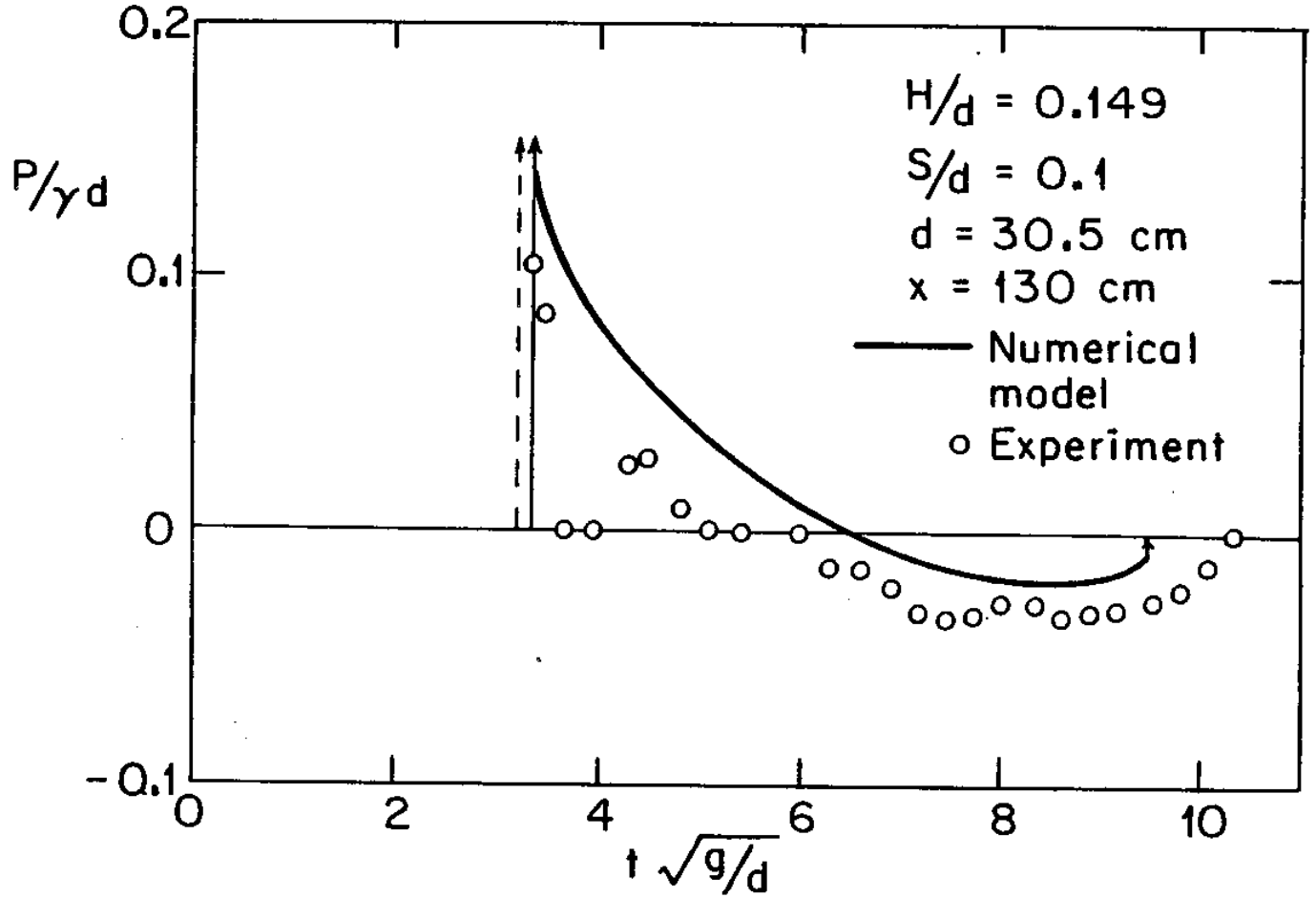

Fig. 6.31 Pressure as a function of time for ε = 0.149, and S/d= 0.1, at x/d = 4.525.

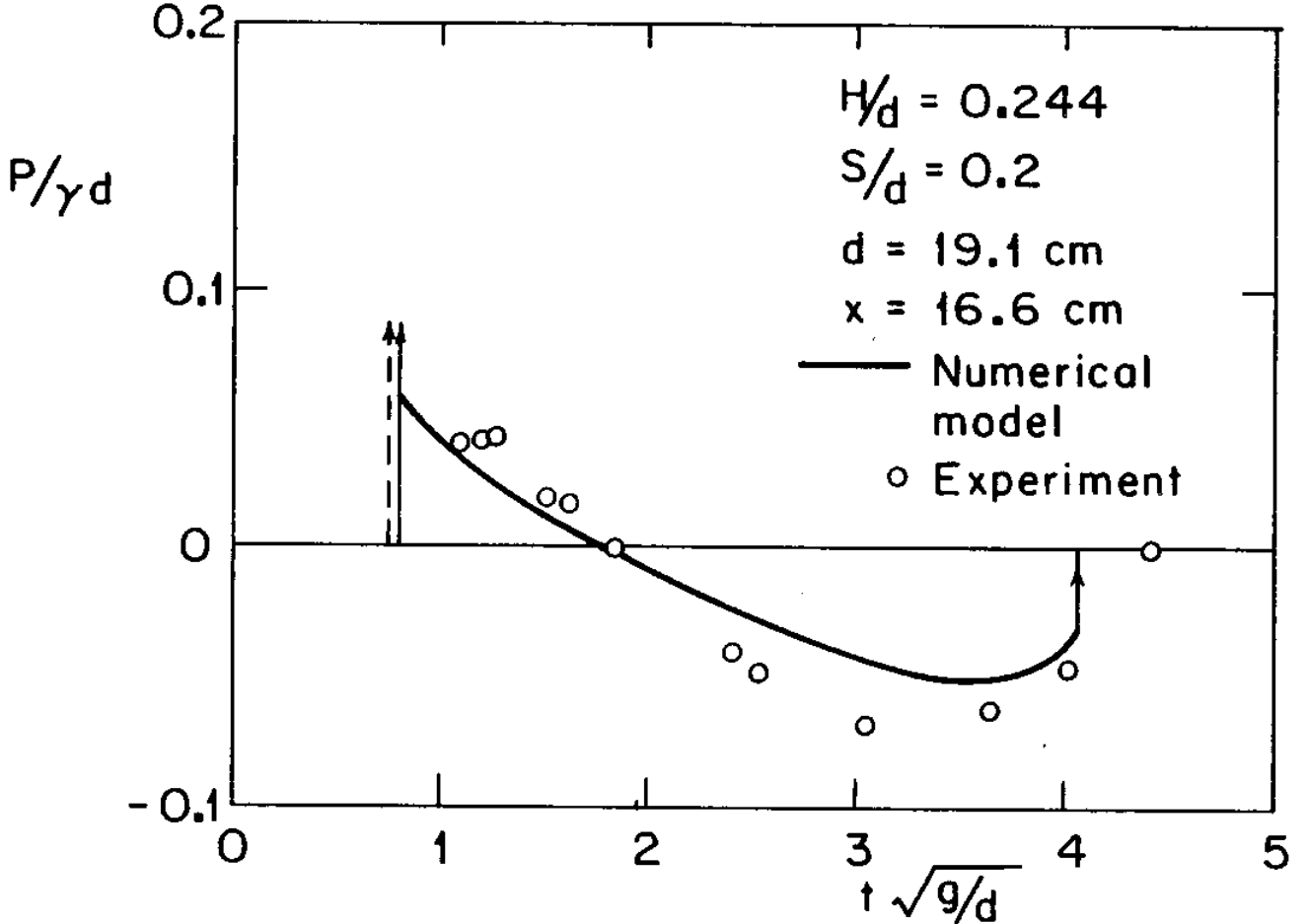

Fig. 6.32 Pressure as a function of time for ε = 0.244, S/d = 0.2, at x/d = 0.816.

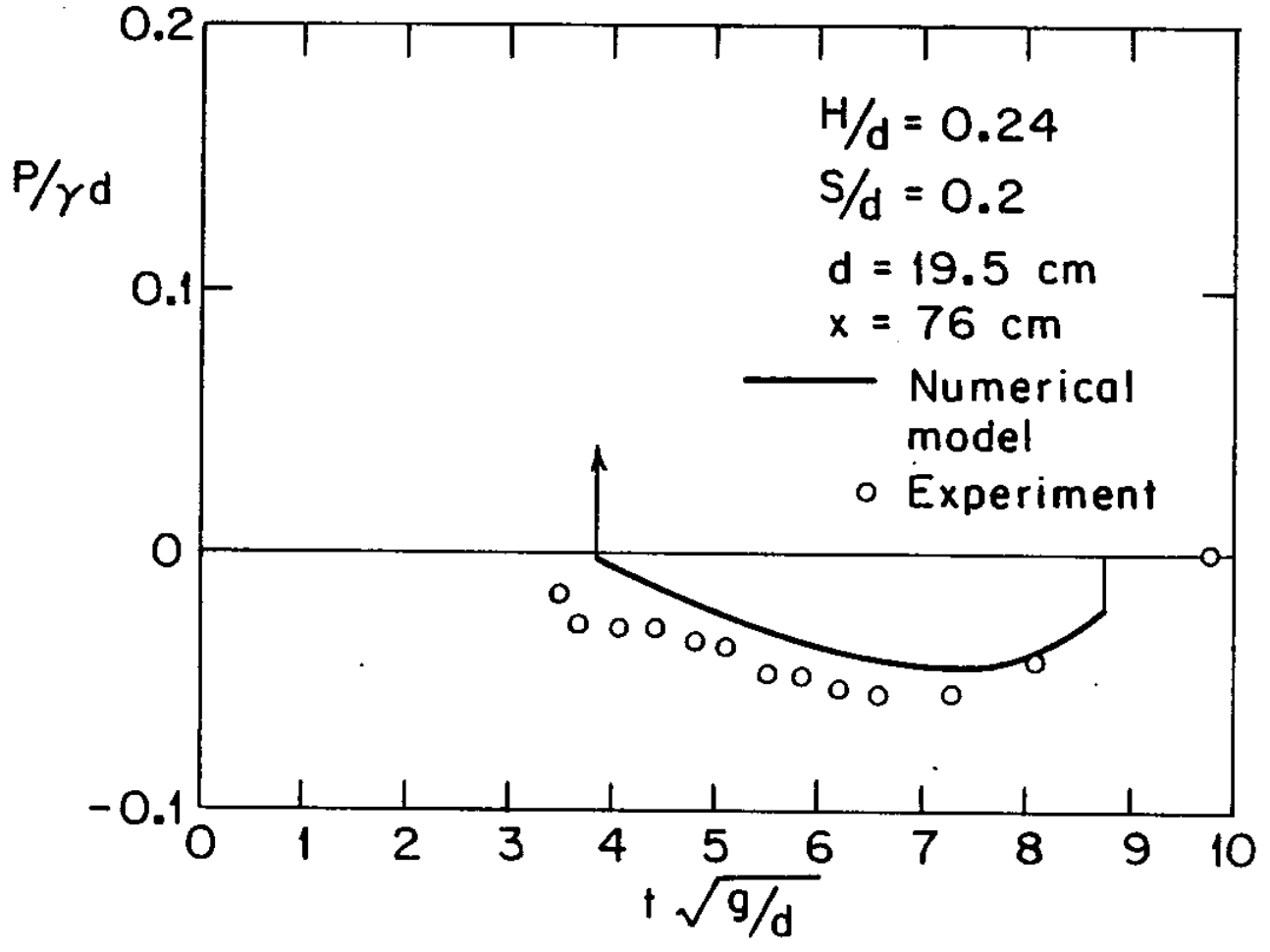

Fig. 6.33 Pressure as a function of time for ε = 0.24, and S/d = 0.2, at x/d = 3.9.

pressure at any given point on the platform decreases with increasing x/d. Comparison of Figs. 6.30 through 6.31 for S/d = 0.1 with Figs. 6.32 through 6.33 for S/d = 0.2 indicates that for any relative position x/d along the platform, the ratio of the duration of the positive to negative uplift pressures increases with the decrease of the relative soffit clearance S/d. Figure 6.32 indicates that waves slightly higher than the soffit clearance will cause a modest uplift pressure but a negative pressure of considerable duration. Figure 6.33 shows the pressure function for a location x/d = 3.9 where the duration of positive uplift pressure is very short, and the duration of negative pressure is longer than for x/d = 8.6 shown in Fig. 6.32.

The time-history of the total uplift force per unit width of the platform is shown in Figs. 6.34 and 6.35. In these figures, uplift force computed based on the present numerical model is normalized with respect to F_s, the hydrostatic force due to an undisturbed wave of height H less than the soffit clearance s (equivalent to the weight of water in the region above the platform). In Fig. 6.34, the experimental results of French (1969) is presented. The comparison is quite encouraging. As can be seen from these figures, the normalized force is

initially positive which increases with time to a maximum; then decreases with time, reaching negative values and then returns to zero. Figure 6.34 indicates that even a wave slightly greater than the platform soffit could exert a negative force of considerable duration. In Fig. 6.35, the normalized uplift force for a platform with smaller soffit clearance is shown. This figure illustrates that as the soffit decreases, the duration of positive uplift force to duration of negative uplift force increases.

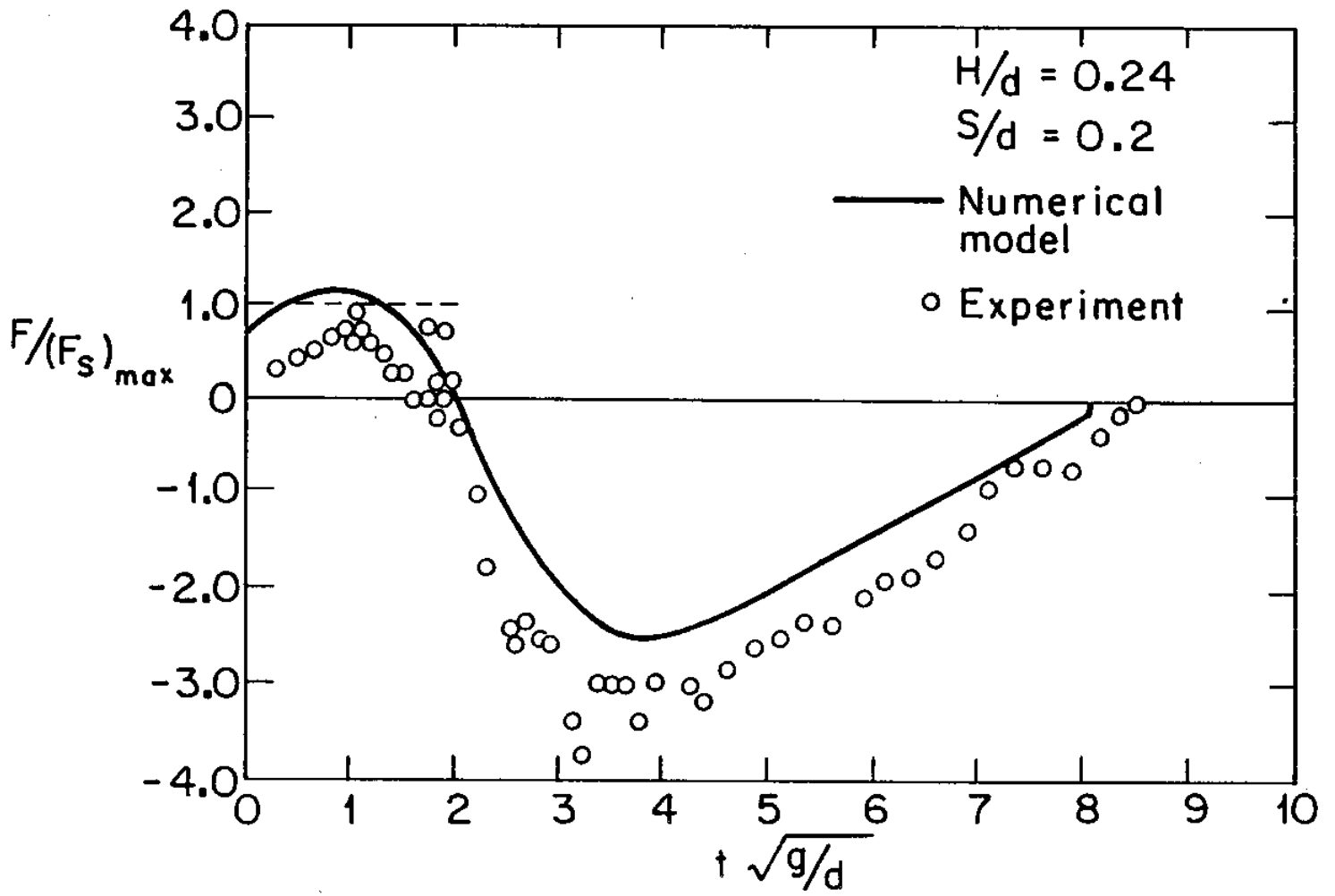

Fig. 6.34 Normalized uplift pressure per unit width, for d = 38.1 cm., L/d = 4.0.

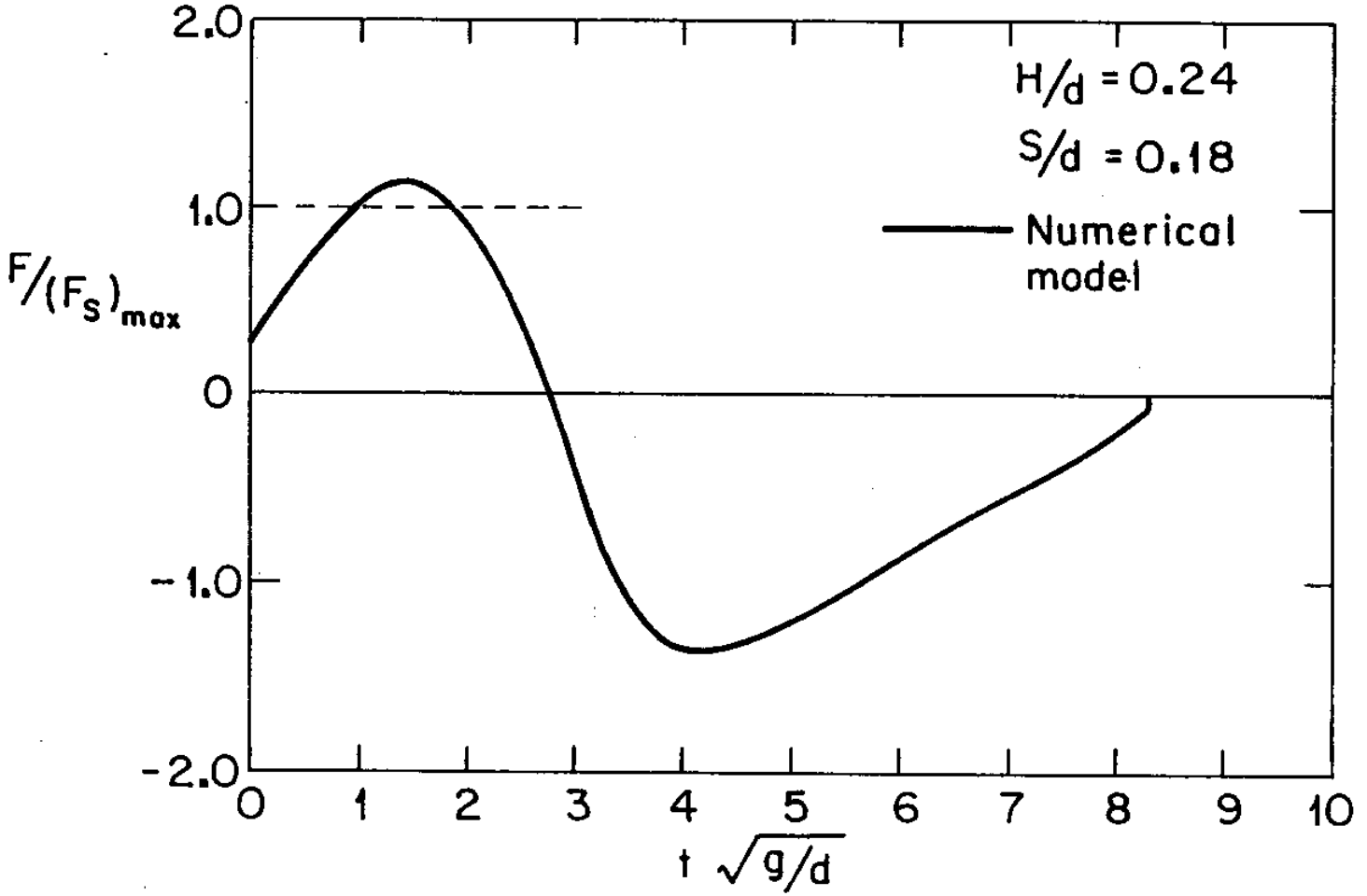

Fig. 6.35 Normalized uplift force per unit width, for d = 3.81 cm., L/d = 4.0.

CHAPTER 7

SUMMARY AND CONCLUSION

The major objective of the present investigation has been concerned with the study of wave hydrodynamic effects on a horizontal platform that result from the incidence of a solitary wave.

In the analysis, a two-dimensional finite element model was considered for the case of inviscid, incompressible, and irrotational fluid region. The geometrical configuration of the fluid domain was described by a horizontal channel bottom and a flat horizontal platform. The conditions chosen for the study are relevant to prototype conditions of interest. Solitary wave was used as a model incident wave, since it represents a relevant model of ocean waves in the region where marine structures are located. In order to construct the finite element model, the fluid region was discretized into small elements of convenient shape. To handle the moving free surface boundary, isoparametric mapping technique was adapted to transform the fluid region into a regular geometry. To generalized the finite

element mesh, each rectangular cell in the parent computational domain was separately mapped to a new isoparametric plane. Finite element discretization of the governing equations was performed by employing the Galerkin weighted residual method. To construct the free surface motion, the free surface equations were integrated with respect to time. This was done by invoking a mass-lumping technique to eliminate any coupling between the time derivative of unknown at adjacent nodes. The time derivatives at computational node were then simulated using explicit forward difference scheme. The stability of the numerical model was tested for propagation of a solitary wave in a fluid region of constant depth. Using the CFL convergence condition, it was found that the algorithm was conditionally stable restricting the time increment to be less than a bounded value. A platform was inserted in the model to simulate the flow transient beneath the platform due to an incident wave. The sequence of the wave impact was studied by the numerical model. An artificial viscosity term was included in the kinematic free surface equation to smooth the rapid oscillation of the free surface, caused by the front edge of the platform. Numerical experiments were performed to determine the numerical value of the viscosity parameter

which maintained a smooth surface profile in front of the platform. A multi-grid solution algorithm was developed and used to speed the repeated solution of linear algebraic equations resulted from finite element discretization of the transformed Laplace equation. It was found that the multi-grid algorithm could effectively be used to reduce the convergence time by several orders of magnitude. An experimental study was conducted in the Keck Hydraulic Laboratory of the California Institute of Technology. A two-dimensional Laser-Doppler velocimeter developed by Raichlen & Lee (1982, 1983) was used to measure the water particle velocities in the fluid region. Wave gages were used to measure the incident and transmitted waves upstream and downstream of the platform. The major difficulty encountered in LDV measurements was due to air entrainment in the fluid region, near the surface and near the leading edge of the platform especially for incident waves of relatively large amplitude. The measurement of vertical velocity was troublesome because of the noise and irregularities present in output data. Several experimental runs were conducted to measure the depthwise variation of the water particle velocities. To ensure that the developed finite element model could be applied with confidence to the

problem of wave impact on a platform, the water particle velocity components induced by an undisturbed solitary wave were computed for several depths and compared with that of Boussinesq's theory and available LDV experimental data. The computed horizontal velocities were found to agree reasonably well with the LDV measurement with maximum deviation of 2%. The computed vertical velocities agreed well with that of Boussinesq's theory but LDV experimental data showed more critical comparison. But the deviation was not very large considering the magnitude of the vertical velocity and the rapid phase changes from positive to negative. Comparisons of numerical model results and the velocity data obtained by an LDV measurement were made for the case of positive as well as zero soffit clearances and at different locations along the platform. Different depthwise positions were considered to define the vertical variation of water particle velocity. The numerical results were found to be in good agreement with experimental data obtained by LDV measurement. For the case of the platform with zero soffit clearance the horizontal velocity profiles demonstrated similar trend as in the case of undisturbed solitary wave except with the reduction of amplitude and increase in base-width. In addition to velocity

components the transmitted waves downstream the platform were computed and compared to that of experimental measurement. This problem may be of interest to breakwater problems. The transmitted wave from a platform with positive soffit clearance appeared to be separating into individual waves of smaller amplitude. However, the maximum amplitude was less than the incident wave. For the case of a platform with zero soffit clearance the transmitted wave profile consisted of a single wave which appeared to have similar trend as a solitary wave but with significant reduction and in wave amplitude.

The uplift pressure time-history were computed and compared to that of French's (1969) experiment using pressure transducers. The pressure profile was characterized by a sudden rise to a peak followed by slowly-varying pressure which was first positive and then negative. The variation of the pressure was obtained for different soffit clearances and different locations along the platform. The positive pressure was predicted at the advancing wave front. It was found that the ratio of the duration of positive uplift pressure to negative uplift pressure decreases with the increase of the relative distance from the front edge of the platform, and pressure induced by a wave of slightly higher than the platform

soffit clearance causes an insignificant positive uplift but a negative uplift of considerable duration.

REFERENCES

Atkinson, K.E. (1978), An Introduction to Numerical Analysis, John Wiley and Sons, New York.

Bathe, K.J. (1982), Finite Element Procedure in Engineering Analysis, Prentice-Hall, Inc., Englewood Cliffs, New Jersey.

Beale, J.T. (1981), "The Initial Value Problem for the Navier-Stokes Equations with a Free Surface," Communication on Pure and Applied Mathematics, Vol. 34, pp. 359-392.

Brandt, A. (1977), "Multi-level Adaptive Solutins to Boundary-Value Problems," Mathematics of Computaton, Vol. 31, No. 138, pp. 333-370.

Boussinesq, J. (1871), "Theorie des ondes et des remous qui se propagent le long d'un canal rectangulaire horizontal, en communiquant au liquide contenu danc ce canal des vitesses sensibilement pareilles de la surface au fond," Journal des Mathematiques, 2nd series, Vol. 17, Paris.

Carrier, G.F. and Pearson, C.E. (1976), Partial

Differential Equations, (Theory and Techniques), Academic Press, New York.

Chen, H.S. and Mei, C.C., (1974), "Oscillations and Wave Forces in an Offshore Harbor, (Applications of Hybrid Finite Element Method to Water-Wave Scattering)," Report No. 190, Ralph M. Parsons Laboratory for Water Resources and Hydrodynamics, Massachusetts Institute of Technology, Cambridge, Massachusetts.

Chung, T.,J. (1978), Finite Element Analysis in Fluid Dynamics, McGraw-Hill Publications, New York.

El Ghamry, O. (1963), "Wave Forces on a Dock," Report No. HEL-9-1, University of California, Berkeley, California.

Currie, I.G.. (1974), Fundamental Mechanics of Fluids, McGraw-Hill Publications, New York.

Dietrich, D., McDonald, B.E., and Warn-Varnas, A. (1975), "Optimized Block-Implicit Relaxation," Journal of Computational Physics, Vol. 18, pp. 421-439.

Easton, C.R. and Catton, I. (1972), "Initial Value Techniques in Free Surface Hydrodynamics," Journal of Computational Physics, Vol. 9, pp. 424-439.

Courant, R., Friedrichs, K., and Lewy, H. (1928), "Uber die partiellen diffelenzgleichungen der mathematischen Physik," Math. Ann. 100, p. 32.

Emery, A.F. (1968), "An Evaluation of Several Differencing Methods for Inviscid Flow Problems," Journal of Computational Physics, Vol. 2, pp. 306-331.

Fairweather, G. and Navon, I.M. (1980), "A Linear ADI Method for the Shallow-Water Equations," Journal of Computational Physics, Vol. 37, pp. 1-18.

Fix, G.J and Larsen, K. (1971), "On the Convergence of SOR Iteration for Finite Element Approximation to Elliptic Boundary Value Problem," SIAM J. Numerical Analysis, Vol. 8, pp. 536-547.

French, J.A. (1969), "Wave Uplift Pressure on Horizontal Platforms," Report No. KH-R-19, W.M. Keck Laboratory of Hydraulics and Water Resources, California Institute of Technology, Pasadena, California.

Friedrich, K.O., Hyers, D.H. (1954), "The Existence of Solitary Wave," Communications on Pure and Applied

Mathematics, Vol. 7, pp. 517-550.

Friedrichs, K. and Lewy, H. (1948), "The Dock Problem," Communications on Applied Mathematics, Vol. 1, No. 2, pp. 135-148.

Goring, D.G. (1979), Tsunamis-The Propagation of Long Waves onto a Shelf, Ph.D. Thesis, California Institute of Technology, Pasadena, California.

Gresho, P.M., Lee, R.L., and Sani, R.L. (1978), "Advection-Dominatd Flows, With Emphasis on the Consequences of Mass Lumping," in Finite Elements and Fluids, R.H. Gallagher, J.T. Odens, C. Taylor, and O.C. Zienkiewicz (Eds.), Vol. III, Wiley-Interscience Publications, New York, pp. 335-350.

Hafez, M.M., Wellford, L.C. and Murman, E.M. (1978), "Finite Elements in Finite Differences for Transonic Flow Calculations," in Finite Elements in Fluid, R.H. Gallagher, J.T. Oden, C. Taylor, and O.C. Zienkiewicz (Eds.), Vol. III, Wiley-Interscience Publications, New York, pp. 219-254.

Harlow, F.H. and Welch, J.E. (1965), "Numerical Calculation of Time-Dependent Viscous Incompressible Flow of Fluid With Surface," The Physics of Fluids,

Vol. 8, No. 12, pp. 2182-2189.

Hirt, C.W. (1968), "Heuristic Stability Theory for Finite-Difference Equations," Journal of Computational Physics, Vol. 2, pp. 339-355.

Hogden, N., Miller, B.L., Searle, J.W., and Ward, G. (1977), "Estimation of Fluid Loading in Offshore Structures," Proceedings of the Institution of Civil Engineers, Part 2, pp. 515-562.

Hornbeck, R.W. (1975), Numerical Methods, Quantum Publishers, Inc., New York.

Hughes, T.J.R., Liu, W.K., and Zimmermann, T.K. (1978), "Lagrangian-Eulerian Finite Element Formulation for Incompressible Viscous Flows," presented at U.S.-Japan Conference on Interdisciplinary Finite Element Analysis, Cornell University, Ithaca, New York.

Ippen, A.T.(1966), Estuary and Coastal Hydrodynamics, McGraw-Hill Publications, New York.

Isaacson, E. (1948), "Waves Against an Overhanging Cliff," Communications on Pure and Applied Mathematics, Vol. 1, No. 2, pp. 201-210.

Jameson, A and Caughey, D.A. (1977), "Finite Volume Method for Transonic Potential Flow Calculation," A.I.A.A. 3rd Computational Fluid Dynamics Conf., New Mexico.

Lax, P.D. (1954), "Weak Solution of Nonlinear Hyperbolic Equations and Their Numerical Computation," Communication on Pure and Applied Mathematics, Vol. 7, pp. 159-193.

Lax, P. and Wendroff, B. (1960), "Systems of Conversation Laws," Communicationns on Pure and Applied Mathematics, Vol. 13, pp. 217-237.

Lee, J.J., Skjelbreia, J., and Raichlen, J. (1982), "Measurement of Velocities in Solitary Waves," Proceedings of the American Society of Civil Engineering, Vol. 108, No. WW2, pp. 200-218.

Lomax,H. and Steger, J. (1975), "Relaxation Methods in Fluid Mechanics,", Annual Review of Fluid Mechanics, Vol. 7, pp. 63-88.

Longuet-Higgins, M.S. (1981), "Trajectories of Particles at the Surface of Steep Solitary Waves," Journal of Fluid Mechanics, Vol. 110, pp. 239-247.

Luck, J.C. (1967), "A Variational Principle for a Fluid with a Free Surface," Journal of Fluid Mechanics, Vol. 27, Part 2, pp. 395-397.

Miles, J.W. (1980), "Solitary Waves," Annual Review of Fluid Mechanics, Vol. 12, pp. 11-43.

Morison, J.R., Johnson, J.W., and O'Brien, M.P. (1953), "Experimental Studies of Forces on Piles," Proceedings of Fourth Conference on Coastal Council on Wave Research, Berkeley, California, pp. 340-370.

Munk, W.H. (1949), "The Solitary Wave Theory and Its Application to Surf Problems," Annals of the New York Academy of Science, Vol. 51, pp. 376-426.

Naheer, E. (1977), "Stability of Bottom Armoring Under the Attack of Solitary Waves,"Report No. KH-R-34, W.M. Keck Laboratory of Hydraulics and Water Resources, California Institute of Technology, Pasadena, California.

Nichols, B.D. and Hirt, C.W. (1971), "Improved Free Surface Boundary Conditions for Numerical Incompressible-Flow Calculations," Journal of Computational Physics, Vol. 8, pp. 434-448.

Nicolaides, R.A. (1975), "On Multiple Grid and Related Techniques for Solving Discrete Elliptic Systems," Journal of Computational Physics, Vol. 19, No. 4, pp. 418-431.

Nicolaides, R.A.(1977), "On the Convergence of an Algorithm for Solving Finite Element Equations," Mathematics of Computation, Vol. 31, No. 140, pp. 892-906.

Parelett, B. (1977), "Roundoff Error in the Solution of Finite Element Systems," in Formulation and Computational Algorithm in Finite Element Analysis, K.J. Bathe, J.T. Oden, and W. Wunderlich (Eds.), pp. 877-913.

Perko, L.M. (1968), "Large-Amplitude Motion of a Liquid-Vapor Interface in an Accelerating Container," Journal of Fluid Mechanics, Vol. 35, Part 1, pp. 77-96.

Raichlen, F. and Lee, J.J. (1982), "Some Experiments Dealing with the Interaction of Currents and Waves," Report to Naval Construction Battalion Center.

Raichlen, F. and Lee, J.J. (1983), "The Interaction of

Solitary Wave with Currents," Report to Naval Construction Battalion Center.

Richtmyer, R.D. and Morton, K.W. (1967), Difference Methods for Initial-Value Problems, Second Edition, Interscence Publishers, A Division of John Wiley and Sons, New York.

Sarpkaya, T. and Isaacson, M. (1981), Mechanics of Wave Forces on Offshore Structures, Van Nostrand Reinhold Company, New York.

Settari, A. and Aziz, K. (1973), "A Generalization of the Additive Collection Methods for the Iterative Solution of Matrix Equations," SIAM Journal of Numerical Analysis, Vol. 10, No. 3, pp. 506-521.

Stoker, J.J. (1957), Water Waves, Wiley Interscience, New York.

Suenderman, J. (1977), "The Application of Finite Element and Finite Difference Techniques in Hydrodynamical Numerical Models," in Formulation and Computational Algorithm in Finite Element Analysis, K.J. Bathe, J.T. Oden, and W. Wunderlich (Eds.), pp. 986-1038.

Turkel, E. and Zwas, G. (1979), "Explicit Large

Time-Step Schemes for the Shallow Water Equations," Advances in Computer Methods for partial Differential Equations, R. Vichnevetsky and R.S. Stepleman (Eds.), Vol. 3, pp. 65-68.

Vanoni, V.A., Brooks, N.H., and Raichlen, F. (1967), "A 40-Meter Precision Tilting Flume," Technical Memorandum 67-3, W.M. Keck Laboratory of Hydraulics and Water Resource, California Institute of Technology, Pasadena, California.

Von Neumann, J. and Richtmyer, R. (1950), "A Method for Numerical Calculation of Hydrodynamic Shocks," Journal of Applied Physics, Vol. 21, pp. 232-237.

Wachspress, E.L. (1977), "Two-Level Finite Element Computation," in Formulation and Computational Algorithms in Finite Element Analysis, K.J. Bathe, J.T. Oden, and W. Wunderlich (Eds.), pp. 877-913.

Wang, H. (1967), "Estimating Wave Pressure on a Horizontal Pier," Technical Report R546, Naval Civil Engineering Laboratory, Port Hueneme, California.

Wellford, L.C. and Ganaba, T. (1981), "A Finite Element Method with a Hybrid Lagrange Line for Fluid Mechanics Problems Involving Larg Free Surface

Motion," International Journal for Numerical Methods in Engineering, Vol. 17, pp. 1201, 1231.

Wellford, L.C. and Vahdani, B. (1981), "A Block Iteration Scheme for the Solution of Systems of Equations Resulting from Linear and Nonlinear Finite Element Models," Computer Methods in Applied Mechanics and Engineering, No. 26, pp. 33-52.

Weigel, R.L. (1964), Oceanographic Engineering, Prentice-Hall, Inc., Englewood Cliffs, New Jersey.

Wylie, C.R. (1960), Advance Engineering Mathematics, Third Edition, McGraw-Hill Publications, New York.

Zienkiewicz, O.C. (1977), The Finite Element Methods, Third Edition, McGraw-Hill Publication, New York.

APPENDIX A

A.1 EVALUATION OF THE ELEMENT STIFFNESS MATRIX

The element stiffness matrix resulting from the finite element discretization of the transferred Laplace equation takes the form

$$K_{ij}=A_{KM}\int_{-1}^{1}\int_{-1}^{1}\Psi_{i,\xi}\Psi_{j,\xi}d\xi d\eta+ B_{KM}\int_{-1}^{1}\int_{-1}^{1}\Psi_{i,\eta}\Psi_{j,\eta}d\xi d\eta+$$

$$\frac{1}{2}C_{kM}\int_{-1}^{1}\int_{-1}^{1}\Psi_{i,\eta}\Psi_{j,\xi}d\xi d\eta+\frac{1}{2}C_{KM}\int_{-1}^{1}\int_{-1}^{1}\Psi_{i,\xi}\Psi_{j,\eta}\,d\xi d\eta-$$

$$D_{KM}\int_{-1}^{1}\int_{-1}^{1}\Psi_{i,\eta}\Psi_{j}\,d\xi d\eta$$

where i = 1,...,4 and j = 1,...,4. These integrals are evaluated as

$$\int_{-1}^{1}\int_{-1}^{1}\Psi_{1,\xi}^{2}\,d\xi d\eta=\frac{1}{3}$$

$$\int_{-1}^{1}\int_{-1}^{1}\Psi_{1,\eta}^{2}\,d\xi d\eta=\frac{1}{3}$$

$$\int_{-1}^{1}\int_{-1}^{1}\Psi_{1,\eta}\Psi_{1,\xi}\,d\xi d\eta=\frac{1}{4}$$

$$\int_{-1}^{1}\int_{-1}^{1}\Psi_{1,\eta}\Psi_{1}\,d\xi d\eta=\frac{1}{3}$$

and so on. Then the entries in the element stiffness matrices are found to be

$$K_{11} = \frac{1}{3} A + \frac{1}{3} B + \frac{1}{4} C + \frac{1}{3} D$$

$$K_{12} = -\frac{1}{3} A + \frac{1}{6} B + \frac{1}{6} D$$

$$K_{13} = -\frac{1}{6} A - \frac{1}{6} B - \frac{1}{4} C - \frac{1}{6} D$$

$$K_{14} = \frac{1}{6} A - \frac{1}{3} B - \frac{1}{3} D$$

$$K_{21} = K_{12}$$

$$K_{22} = \frac{1}{3} A + \frac{1}{3} B - \frac{1}{4} C + \frac{1}{3} D$$

$$K_{23} = \frac{1}{6} A - \frac{1}{3} B - \frac{1}{3} D$$

$$K_{24} = -\frac{1}{6} A - \frac{1}{6} B + \frac{1}{4} C - \frac{1}{6} C$$

$$K_{31} = K_{13}$$

$$K_{32} = K_{23}$$

$$K_{33} = \frac{1}{3} A + \frac{1}{3} B + \frac{1}{4} C - \frac{1}{3} D$$

$$K_{34} = -\frac{1}{3} A + \frac{1}{6} B - \frac{1}{6} D$$

$$K_{41} = K_{14}$$

$$K_{42} = K_{24}$$

$$K_{43} = K_{34}$$

$$K_{44} = \frac{1}{3} A + \frac{1}{3} B - \frac{1}{4} C - \frac{1}{3} D$$

All the coefficients are evaluated at the center of the element (k,m), where k and m are column and row numbers of the lower-right node.

A.2 DERIVATION OF GLOBAL FINITE ELEMENT EQUATIONS

To obtain the global finite element equations, we isolate the typical group of assembled elements of Fig. 4.5 which are pictured in Figs. A.1a through A.1f,

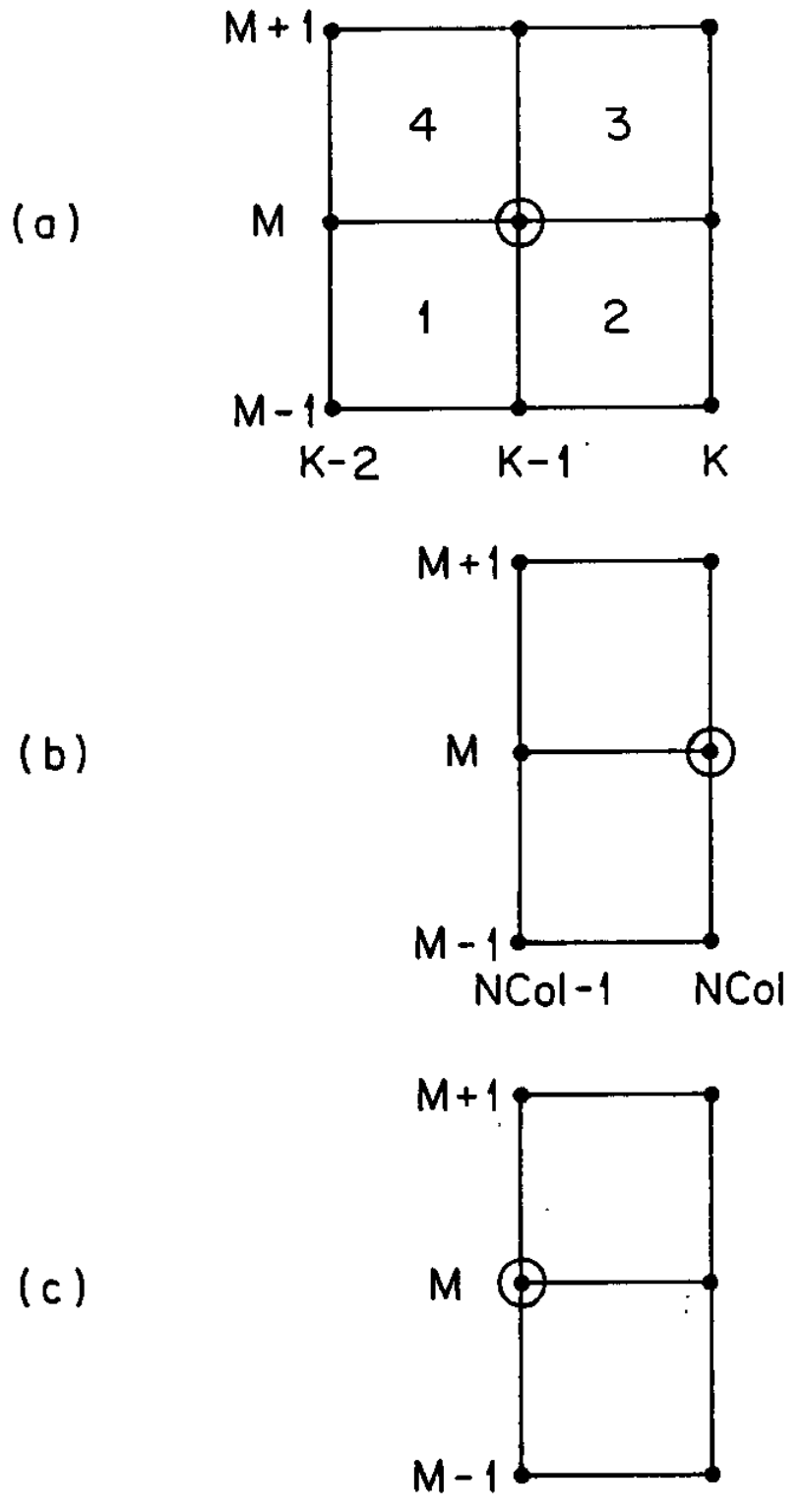

Fig. A-1 Typical groups of assembled elements for the flow region. (a) Interior elements, (b) right-side element, (c) left-side elements, (d) bottom-side elements, (e) left-corner element, (f) right-corner element.

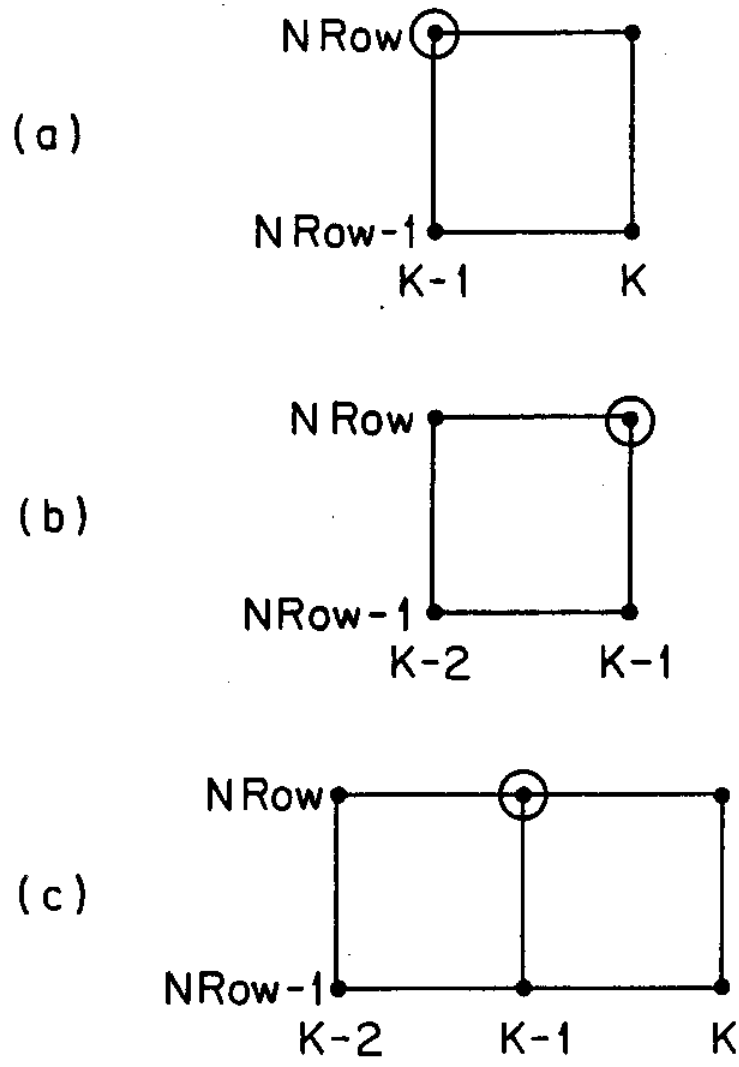

Fig. A-1 Continued.

where NROW and NCOL represent the number of nodes in horizontal and vertical directions, respectively. The global equation for each typical group of assembled elements, shown in Figs. A.1, is obtained by finding the appropriate entries from the local matrices which define the coefficients in the finite element equations. The global equations are found as,

$$\phi(K-1,M) = -\frac{1}{\overset{*}{A}(K-1,M)}\left[\overset{*}{A}(K-2,M-1)\phi(K-2,M-1)+\overset{*}{A}(K-1,M-1)\right.$$
$$\phi(K-1,M-1)+\overset{*}{A}(K,M-1)\phi(K,M-1)+\overset{*}{A}(K-2,M)\phi(K-2,M)+$$
$$\overset{*}{A}(K,M)\phi(K,M)+\overset{*}{A}(K-2,M+1)\phi(K-2,M+1)+\overset{*}{A}(K-1,M+1)\phi(K-1,M+1)$$
$$\left.+\overset{*}{A}(K,M+1)\phi(K,M+1)\right] \qquad (A.1a)$$

$K = 3,\ldots,NCOL$
$M = 2,\ldots,NROW-1$

where

$$\overset{*}{A}(K-2,M-1) = \overset{①}{K}_{31}$$
$$\overset{*}{A}(K-1,M-1) = \overset{①}{K}_{32} + \overset{②}{K}_{41}$$
$$\overset{*}{A}(K,M-1) = \overset{②}{K}_{42}$$
$$\overset{*}{A}(K-2,M) = \overset{①}{K}_{34} + \overset{④}{K}_{21}$$
$$\overset{*}{A}(K-1,M) = \overset{①}{K}_{33} + \overset{②}{K}_{44} + \overset{③}{K}_{11} + \overset{④}{K}_{22}$$
$$\overset{*}{A}(K,M) = \overset{②}{K}_{43} + \overset{③}{K}_{12}$$
$$\overset{*}{A}(K-2,M+1) = \overset{④}{K}_{24}$$
$$\overset{*}{A}(K-1,M+1) = \overset{④}{K}_{23} + \overset{③}{K}_{14}$$
$$\overset{*}{A}(K,M+1) = \overset{③}{K}_{13}$$

superscripts in the above expression represent the element numbers shown in Fig. A.1a. For instance, the superscript ① represents the element (K,M-1) according to our convention. Referring to Fig. A.1b, we have,

$$\phi(K,M) = -\frac{1}{\overset{*}{B}(K,M)}\left[\overset{*}{B}(K-1,M-1)\phi(K-1,M-1)+\overset{*}{B}(K,M-1)\phi(K,M-1)\right.$$
$$+\overset{*}{B}(K-1,M)\phi(K-1,M)+\overset{*}{B}(K-1,M+1)\phi(K-1,M+1)$$
$$\left.+\overset{*}{B}(K,M+1)\phi(K,M+1)\right]$$

$$K = NCOL \qquad M = 2,\ldots,NROW-1 \qquad \text{(A.1b)}$$

where

$$\overset{*}{B}(K-1,M-1) = \overset{②}{K}_{31}$$
$$\overset{*}{B}(K,M-1) = \overset{②}{K}_{32}$$
$$\overset{*}{B}(K-1,M) = \overset{②}{K}_{34} + \overset{③}{K}_{21}$$
$$\overset{*}{B}(K,M) = \overset{②}{K}_{33} + \overset{③}{K}_{22}$$
$$\overset{*}{B}(K-1,M+1) = \overset{③}{K}_{24}$$
$$\overset{*}{B}(K,M+1) = \overset{④}{K}_{23}$$

Referring to Fig. A.1c, we obtain,

$$\phi(K-1,M) = \frac{1}{\overset{*}{C}(K-1,M)}\left[\overset{*}{C}(K-1,M-1)\phi(K-1,M-1)\right.$$
$$+\overset{*}{C}(K,M-1)\phi(K,M-1) + \overset{*}{C}(K,M)\phi(K,M)$$
$$\left.+\overset{*}{C}(K-1,M+1)\phi(K-1,M+1) + \overset{*}{C}(K,M+1)\phi(K,M+1)\right] \qquad \text{(A.1c)}$$

$$K = 2 \qquad M = 2,\ldots,NROW-1$$

where

$$\overset{*}{C}(K-1,M-1) = \overset{①}{K}_{41}$$

$$\overset{*}{C}(K,M-1) = \overset{①}{K}_{42}$$

$$\overset{*}{C}(K-1,M) = \overset{①}{K}_{44} + \overset{②}{K}_{11}$$

$$\overset{*}{C}(K,M) = \overset{①}{K}_{43} + \overset{②}{K}_{12}$$

$$\overset{*}{C}(K-1,M+1) = \overset{②}{K}_{14}$$

$$\overset{*}{C}(K,M+1) = \overset{②}{K}_{13}$$

and

$$\boxed{\begin{aligned}\phi(K-1,M) = -\frac{1}{\overset{*}{D}(K-2,M)}\Big[&\overset{*}{D}(K-2,M)\phi(K-2,M)\\ &+\overset{*}{D}(K,M)\phi(K,M)+\overset{*}{D}(K-2,M+1)\phi(K-2,M+1)\\ &+\overset{*}{D}(K-1,M)\phi(K-1,M)+\overset{*}{D}(K,M+1)\phi(K,M+1)\Big]\end{aligned}} \qquad \text{(A.1d)}$$

$$K = 3,\ldots,\ \text{NCOL}$$
$$M = 1$$

where

$$\overset{*}{D}(K-2,M) = \overset{④}{K}_{21}$$

$$\overset{*}{D}(K-1,M) = \overset{④}{K}_{22} + \overset{③}{K}_{11}$$

$$\overset{*}{D}(K,M) = \overset{③}{K}_{12}$$

$$\overset{*}{D}(K-2,M+1) = \overset{④}{K}_{24}$$

$$\overset{*}{D}(K-1,M+1) = \overset{④}{K}_{23} + \overset{③}{K}_{14}$$

$$\overset{*}{D}(K,M+1) = \overset{③}{K}_{23}$$

and

$$\phi(K,M) = -\frac{1}{\overset{*}{E}(K,M)}\left[\overset{*}{E}(K+1,M)\phi(K+1,M) + \overset{*}{E}(K,M+1)\phi(K,M+1) + \overset{*}{E}(K+1,M+1)\phi(K+1,M+1)\right] \qquad \text{(A.1e)}$$

$K = 1$
$M = 1$

where

$$\overset{*}{E}(K,M) = \overset{③}{K}_{11}$$

$$\overset{*}{E}(K+1,M) = \overset{③}{K}_{12}$$

$$\overset{*}{E}(K+1,M+1) = \overset{③}{K}_{13}$$

$$\overset{*}{E}(K,M+1) = \overset{③}{K}_{14}$$

and

$$\phi(K,M) = -\frac{1}{\overset{*}{F}(K,M)}\left[F(K-1,M)\phi(K-1,M) + F(K,M+1)\phi(K,M+1) + F(K-1,M+1)\phi(K-1,M+1)\right] \qquad \text{(A.1f)}$$

$K = NCOL$
$M = 1$

where $\overset{*}{F}(K-1,M) = \overset{④}{K}_{21}$

$\overset{*}{F}(K,M) = \overset{④}{K}_{22}$

$\overset{*}{F}(K-1,M+1) = \overset{④}{K}_{23}$

$\overset{*}{F}(K,M+1) = \overset{④}{K}_{24}$

A.3 GLOBAL REPRESENTATION OF THE EQUATIONS OF THE FREE SURFACE

Referring to Figs. A.2a through A.2c, the global free surface equations are obtained in the following:

(a) Equations for the element left node:

$$\frac{2}{3}\phi_{,t}(K,M)+\frac{4}{3}\phi_{,t}(K-1,M)=P_1\phi^2(K-1,M-1)+P_2\phi(K-1,M-1)\phi(K,M-1)$$
$$+P_3\phi(K-1,M-1)\phi(k,M)+P_4\phi(K-1,M-1)\phi(K-1,M)+P_5\phi^2(K,M-1)$$
$$+P_6\phi(K,M-1)\phi(K,M)+P_7\phi(K,M-1)\phi(K-1,M)+P_8\phi^2(K,M) \qquad (A.2a)$$
$$+P_9\phi(K,M)\phi(K-1,M)+P_{10}\phi^2(K-1,M)-\frac{4}{3}\,gh(K-1,M)-\frac{2}{3}\,gh(K,M)$$
$$+\ 2gd$$

and

$$\frac{2}{3}\,h_{,t}(K-1,M)+\frac{1}{3}\,h_{,t}(K,M)=q_1\phi(K-1,M-1)+q_2\phi(K,M-1)+q_3\phi(K,M)$$
$$+q_4\phi(K-1,M)+q_5\phi(K-1,M-1)h(K-1,M)+q_6\phi(K-1,M-1)h(K,M) \qquad (A.2b)$$
$$+q_7\phi(K,M-1)h(K-1,M)+q_8\phi(K,M-1)h(K,M)+q_9\phi(K,M)h(K-1,M)$$
$$+q_{10}\phi(K,M)h(K,M)+q_{11}\phi(K-1,M)h(K-1,M)+q_{12}\phi(K-1,M)h(K,M)=0$$

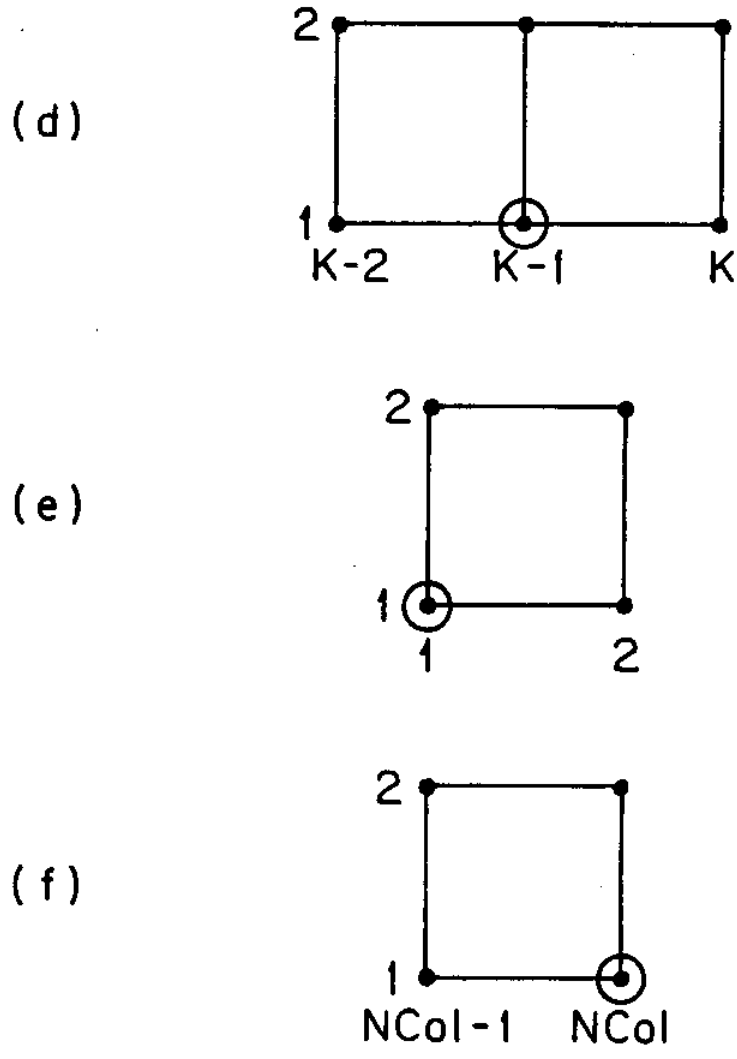

Fig. A-2 Typical groups of assembled elements for the free surface boundary. (a) surface elements, (b) left-coner element, (c) right-corner element.

where

$$P_1 = -\frac{1}{8} B$$

$$P_2 = -\frac{1}{12} B$$

$$P_3 = \frac{1}{12} B + \frac{1}{6} C$$

$$P_4 = \frac{1}{4} B - \frac{1}{6} C$$

$$P_5 = -\frac{1}{24} B$$

$$P_6 = \frac{1}{12} B + \frac{1}{12} C$$

$$P_7 = \frac{1}{12} B - \frac{1}{12} C$$

$$P_8 = -(\frac{1}{4} A + \frac{1}{24} B + \frac{1}{12} C)$$

$$P_9 = -(-\frac{1}{2} A + \frac{1}{12} B + \frac{1}{12} C)$$

$$P_{10} = -(\frac{1}{4} A + \frac{1}{8} B - \frac{1}{6} C)$$

$$q_1 = -\frac{1}{3} G$$

$$q_2 = -\frac{1}{6} G$$

$$q_3 = \frac{1}{6} G$$

$$q_4 = \frac{1}{3} G$$

$$q_5 = -\frac{1}{6} H$$

$$q_6 = \frac{1}{6} H$$

$$q_7 = -\frac{1}{12} H$$

$$q_8 = \frac{1}{12} H$$

$$q_9 = \frac{1}{4} A + \frac{1}{12} H$$

$$q_{10} = -\frac{1}{4} A + \frac{1}{12} H$$

$$q_{11} = -\frac{1}{4} A + \frac{1}{6} H$$

$$q_{12} = \frac{1}{4} A - \frac{1}{6} H$$

All the coefficients are evaluated at the center of the element whose right-lower corner node has the subscripts (K,M-1).

(b) Equations for the element right node:

$$\frac{2}{3}\phi_{,t}(K-2,M)+\frac{4}{3}\phi_{,t}(K-1,M)=r_1\phi^2(K-2,M-1)$$
$$+r_2\phi(K-2,M-1)\phi(K-1,M-1)+r_3\phi(K-2,M-1)\phi(K-1,M)$$
$$+r_4\phi(K-2,M-1)\phi(K-2,M)+r_5\phi^2(K-1,M-1)+ \qquad \text{(A.2c)}$$
$$+r_6\phi(K-1,M-1)\phi(K-1,M)+r_7\phi(K-1,M-1)\phi(K-2,M)+r_8\phi^2(K-1,M)$$
$$+r_9\phi(K-1,M)\phi(K-2,M)+r_{10}\phi^2(K-2,M)$$
$$-\frac{2}{3}\,gh(K-2,M)-\frac{4}{3}\,gh(K-1,M)+2gd$$

and

$$\frac{1}{3}\,h_{,t}(K-2,M)+\frac{2}{3}\,h_{,t}(K-1,M)=t_1\phi(K-2,M-1)+t_2\phi(K-1,M-1)$$
$$+t_3\phi(K-1,M)+t_4\phi(K-2,M)+t_5\phi(K-2,M-1)h(K-2,M)$$
$$+t_6\phi(K-2,M-1)h(K-1,M)+t_7\phi(K-1,M-1)h(K-2,M) \qquad \text{(A.2d)}$$
$$+t_8\phi(K-1,M-1)h(K-1,M)+t_9\phi(K-1,M)h(K-2,M)$$
$$+t_{10}\phi(K-1,M)h(K-1,M)+t_{11}\phi(K-2,M)h(K-2,M)$$
$$+t_{12}\phi(K-2,M)h(K-1,M)$$

where

$$r_1 = -\frac{1}{24}\,B$$
$$r_2 = -\frac{1}{12}\,B$$
$$r_3 = \frac{1}{12}\,B+\frac{1}{12}\,C$$
$$r_4 = \frac{1}{12}\,B-\frac{1}{12}\,C$$
$$r_5 = -\frac{1}{8}\,B$$
$$r_6 = \frac{1}{4}\,B+\frac{1}{6}\,C$$

$$r_7 = \frac{1}{12} B - \frac{1}{6} C$$

$$r_8 = -(\frac{1}{4} A + \frac{1}{8} B + \frac{1}{6} C)$$

$$r_9 = -(-\frac{1}{2} B + \frac{1}{12} B - \frac{1}{12} C)$$

$$r_{10} = -(\frac{1}{4} A + \frac{1}{24} B - \frac{1}{12} C)$$

$$t_1 = -\frac{1}{6} G$$

$$t_2 = -\frac{1}{3} G$$

$$t_3 = \frac{1}{3} G$$

$$t_4 = \frac{1}{6} G$$

$$t_5 = -\frac{1}{12} H$$

$$t_6 = \frac{1}{12} H$$

$$t_7 = -\frac{1}{6} H$$

$$t_8 = \frac{1}{6} H$$

$$t_9 = \frac{1}{4} A + \frac{1}{6} H$$

$$t_{10} = -(\frac{1}{4} A + \frac{1}{6} H)$$

$$t_{11} = -\frac{1}{4} A + \frac{1}{12} H$$

$$t_{12} = \frac{1}{4} A - \frac{1}{12} H$$

(c) Equations for assembled elements:

$$\begin{aligned}
&\tfrac{2}{3}\phi_{,t}(K-2,M)+\tfrac{8}{3}\phi_{,t}(K-1,M)+\tfrac{2}{3}\phi_{,t}(K,M)=(P_1+r_5)\phi^2(K-1,M-1)\\
&+(P_{10}+r_8)\phi^2(K-1,M)+(P_4+r_6)\phi(K-1,M-1)\phi(K-1,M)\\
&+P_2\phi(K-1,M-1)\phi(K,M-1)+P_3\phi(K-1,M-1)\phi(K,M)+P_5\phi^2(K,M-1)\\
&+P_6\phi(K,M-1)\phi(K,M)+P_7\phi(K,M-1)\phi(K-1,M)+P_8\phi^2(K,M)\\
&+P_9\phi(K-1,M)\phi(K,M)+r_1\phi^2(K-2,M-1)+r_2\phi(K-2,M-1)\phi(K-1,M-1)\\
&+r_3\phi(K-2,M-1)\phi(K-1,M)+r_4\phi(K-2,M-1)\phi(K-2,M)\\
&+r_7\phi(K-1,M-1)\phi(K-2,M)+r_9\phi(K-1,M)\phi(K-2,M)+r_{10}\phi^2(K-2,M)\\
&-\tfrac{2}{3}gh(K-2,M)-\tfrac{8}{3}gh(K-1,M)-\tfrac{2}{3}gh(K,M)+4gd
\end{aligned} \qquad (A.2e)$$

and

$$\frac{1}{3}\,h_{,t}(K-2,M)+\frac{4}{3}\,h_{,t}(K-1,M)+\frac{1}{3}\,h_{,t}(K,M)=(q_1+t_2)\phi(K-1,M-1)$$
$$+(q_4+t_3)\phi(K-1,M)+q_2\phi(K,M-1)+q_3\phi(K,M)+t_1\phi(K-2,M-1)$$
$$+t_4\phi(K-2,M)+(q_5+t_8)\phi(K-1,M-1)h(K-1,M)+$$
$$+(q_{11}+t_{10})\phi(K-1,M)h(K-1,M)+q_6\phi(K-1,M-1)h(K,M) \qquad \text{(A.2f)}$$
$$+q_7\phi(K,M-1)h(K-1,M)+q_8\phi(K,M-1)h(K,M)+q_9\phi(K,M)h(K-1,M)$$
$$+q_{10}\phi(K,M)h(k,M)+q_{12}\phi(K-1,M)h(k,M)+t_5\phi(K-2,M-1)h(K-2,M)$$
$$+t_6\phi(K-2,M-1)h(k-1,M)+t_7\phi(K-1,M-1)h(K-2,M)+$$
$$+t_9\phi(K-1,M)h(K-2,M)+t_{11}\phi(K-2,M)h(K-2,M)$$
$$+t_{12}\phi(K-2,M)h(K-1,M)$$

APPENDIX B

B-1. MULTI-GRID L_2-NORM AT DIFFERENT GRID LEVEL

GRID LEVEL	L2-NORM OF ERROR
1	12.82637
1	11.35155
2	12.64928
2	11.36476
3	8.204524
3	6.862130
4	4.171836
4	3.294989
3	3.392702
2	3.141024
1	2.124808
1	1.701539
2	1.827396
2	1.623309
3	1.181929
3	0.9875039
4	0.6193031
4	0.4911679
3	0.4874255
2	0.4602108
1	0.3753730
1	0.2942406
2	0.3170389
2	0.2824114
3	0.2054260
3	0.1716066
4	0.1067053
4	8.454743E-02
3	8.462567E-02
2	8.039350E-02
1	6.513935E-02
1	5.031110E-02
2	5.304775E-02
2	4.721094E-02
3	3.409302E-02
3	2.848766E-02
4	1.742949E-02

Level 1=finest grid

4	1.377310E-02
3	1.410825E-02
2	1.359786E-02
1	1.240820E-02
1	9.397863E-03
2	9.667135E-03
2	8.317992E-03
3	5.978842E-03
3	4.923012E-03
4	2.978747E-03
4	2.352337E-03
3	2.391618E-03
2	2.412377E-03
1	2.586683E-03
1	1.853257E-03
1	1.605844E-03
2	1.723453E-03
2	1.438014E-03
3	1.046082E-03
3	8.445124E-04
4	5.185505E-04
4	4.118384E-04
3	3.958755E-04
2	4.139456E-04
1	4.278330E-04
1	2.923796E-04
1	2.504835E-04
2	2.703937E-04
2	2.207767E-04
3	1.652494E-04
3	1.316729E-04
4	8.450641E-05
4	6.765540E-05
5	4.404834E-05
5	3.702663E-05
5	2.890576E-05
4	2.644456E-05
3	3.313594E-05
2	4.846873E-05
1	6.130373E-05
1	3.212316E-05
1	2.555994E-05
2	2.737813E-05
2	2.157750E-05
3	1.661729E-05
3	1.303702E-05
4	8.846415E-06

4	7.158660E-06
5	5.073812E-06
5	4.296860E-06
5	3.384851E-06
4	2.506311E-06
3	2.827892E-06
2	4.991089E-06
1	6.690094E-06
1	3.125241E-06
1	2.374194E-06